Temperature Dependence of Carbon Kinetic Isotope Effect for the Oxidation Reaction of Ethane by Hydroxyl Radicals Under Atmospherically Relevant Conditions: Experimental and Theoretical Studies

Tammarat Piansawan

JÜLICH
FORSCHUNGSZENTRUM

Temperature Dependence of Carbon Kinetic Isotope Effect for The Oxidation Reaction of Ethane by Hydroxyl Radicals Under Atmospherically Relevant Conditions: Experimental and Theoretical Studies

by

Tammarat Piansawan

Presented to the School of Mathematics and Natural Sciences in fulfillment of the dissertation requirement for the degree of

Doctor Rerum Naturalium

Doctoral Program in Physics

University of Wuppertal

Wuppertal, Germany

December 2015

Die Dissertation kann wie folgt zitiert werden:

Temperature Dependence of Carbon Kinetic Isotope Effect for the Oxidation Reaction of Ethane by Hydroxyl Radicals Under Atmospherically Relevant Conditions: Experimental and Theoretical Studies

Tammarat Piansawan

Abstract

Ethane is the second most abundant hydrocarbon in the atmosphere, after methane, impacting on air quality, human health and climate. A quantification of its effects requires accurate knowledge of sources, processes along transport, and sinks. Carbon stable isotopic ratio investigations, complementarily to concentration measurements, were demonstrated to give more insight in source apportionment and atmospheric processing of organic compounds.

Yet, apportionment of atmospheric ethane sources, processing and sinks by using the ^{13}C isotopic composition (δ^{13}C) requires accurate knowledge of the stable carbon kinetic isotope effect (KIE) of its atmospheric degradation through oxidation by hydroxyl (OH) radicals. Moreover, the interpretation of tropospheric ambient data should account for the temperature dependence of KIE, since the tropospheric temperatures can vary extremely, over the range of 180-320 K.

In this work, the KIE temperature dependence for the oxidation of ethane by OH radicals in the tropospherically relevant temperature range was comprehensively investigated by experimental measurements and theoretical calculations. A framework to apply the observed KIE for interpreting ambient observations is presented. Experiments to determine the KIE temperature dependence of ethane oxidation by OH radicals were carried out with natural isotope abundances in the reactant, at ambient pressure, and in a temperature range of 243 to 303 K. Propane was used as a reference compound to verify the ethane chemistry. Chemical reactions were carried out in a ~12 L FEP reaction chamber, suspended in a newer developed temperature controlled oven. Using Thermal Desorption – Gas Chromatography – Combustion – Isotopic Ratio Mass Spectrometry (TD-GC-C-IRMS), the KIE of ethane with OH radical was derived from the temporal evolution of the ethane δ^{13}C and concentration. At 303 ± 0.1 and 288.0 ± 0.3 K, the KIE values for the ethane oxidation by OH were found to be 7.45 ± 0.48 and 7.16 ± 0.54 ‰, respectively,

showing a remarkable improvement of the measurement precision compared to the only available KIE value of 8.57 ± 1.95 ‰ at 296 ± 4 K reported by Anderson et al. (2004). Over the investigated temperature range, a slight increasing tendency of KIE toward lower temperatures was found, being approximately 0.4 ± 0.1 ‰ per 10 K.

Quantum mechanical calculations together with semi-Classical Transition State Theory (SCTST) were employed to theoretically determine the temperature dependence of KIE for reaction of ethane with OH in the temperature range of 150 – 400 K. The goal of this study was to better understand the reaction kinetics, as well as to investigate KIE at temperatures where experimental work has strong limitations. The quantum mechanical calculations were performed employing the M06-2X density functional theory method with an aug-cc-pVTZ basis set. Energy refinements were carried out at high-level theory CCSD(T) using aug-cc-pVxZ (x = D,T,Q) basis set, with extrapolation to the complete basis set limit (CBS). To this end, the 3-parameter expression aug-Schwartz6(DTQ) was employed in CBS. Tunneling effects and internal rotation treatments were also included in the KIE computation. For the first time, the anharmonicity of molecular vibration, and internal rotation was considered for the ethane + OH system. The theoretically computed KIE values are overestimated by approximately a factor of six, compared to the experimental results. However, a slightly negative temperature dependence of the theoretical KIE supports the experimental findings.

Implications of using the refined KIE values in investigating the isotopic fractioning of ethane during its chemical degradation in the atmosphere are discussed.

Kurzzusammenfassung

Ethan ist der zweithäufigste Kohlenwasserstoff in der Atmosphäre nach Methan. Es beeinflusst die Luftqualität, die menschliche Gesundheit und das Klima. Eine Quantifizierung möglicher Auswirkungen erfordert genaue Kenntnisse über seine Quellen und Senken, sowie über die Prozesse, die während des atmosphärischen Transportes stattfinden. Mithilfe von Untersuchungen zu stabilen Kohlenstoffisotopenverhältnissen kann man, komplementär zu Konzentrationsmessungen, einen fundierten Einblick in die Quellenzuordnung und in die atmosphärischen Abbauprozesse von organischen Verbindungen gewinnen.

Die genaue Beschreibung von troposphärischen Ethanquellen, Prozessen und Senken anhand der ^{13}C-Isotopenzusammensetzung (δ^{13}C) erfordert präzise Kenntnis des kinetischen Isotopeneffekts (KIE) des atmosphärischen Abbaus von Ethan durch Oxidation mit Hydroxylradikalen (OH). Darüber hinaus sollte die Temperaturabhängigkeit des KIEs aufgeklärt werden, um Feldmessungen zu interpretieren, da die Temperaturen in der Troposphäre von 180 bis zu 320 K variieren können.

In dieser Arbeit wurde die KIE-Temperaturabhängigkeit für die Oxidation von Ethan durch OH-Radikale durch umfassende experimentelle Messungen und theoretischen Berechnungen untersucht. Die Implikationen einer Anwendung des beobachteten KIEs für die Interpretation von Feldmessungen werden diskutiert.

Experimente zur Bestimmung der Temperaturabhängigkeit des KIEs für die Ethanoxidation durch OH-Radikale wurden mit einem Reaktanten, der eine natürliche Isotopenhäufigkeit aufwies, bei Umgebungsdruck und im Temperaturbereich von 243 bis 303 K durchgeführt. Propan wurde als Referenzverbindung verwendet, um die Ethanchemie zu verifizieren. Chemische Reaktionen wurden in einer ~12 L FEP-Reaktionskammer durchgeführt. Diese befand sich in einem neu entwickelten, temperaturgesteuerten Ofen. Eine Thermodesorption – Gaschromatographie –

Verbrennung – Isotopenverhältnis–Massenspektrometrie (TD-GC-C-IRMS) Methode wurde entwickelt und getestet. KIE für die Reaktion des Ethans mit OH wurde aus dem zeitlichen Verlauf der δ^{13}C und der Konzentration von Ethan abgeleitet. Die gemessenen werte von 7,45 ± 0,48 ‰ bei 303 ± 0,1 K und 7,16 ± 0,54 ‰ bei 288,0 ± 0,3 K, zeigen eine bemerkenswerte Verbesserung der Messgenauigkeit im Vergleich zu dem KIE-Wert von 8,57 ± 1,95 ‰, bestimmt von Anderson et al. (2004) bei 296 ± 4 K. Über den untersuchten Temperaturbereich wurde eine leichte steigende Tendenz des KIEs (0,4 ± 0,1 ‰ pro 10 K) zu niedrigeren Temperaturen hin gefunden.

Quantenmechanischen Rechnungen wurden zusammen mit der semi-klassischen Eyring-Theorie (SCTST) angewendet, um die Temperaturabhängigkeit des KIEs für die Reaktion von Ethan mit OH in einem Temperaturbereich von 150 bis 400 K theoretisch zu bestimmen. Das Ziel dieses Teils der Arbeit war es, die Reaktionskinetik besser zu verstehen, sowie Aussagen über den KIE bei Temperaturen zu treffen, bei denen die experimentelle Bestimmung nicht möglich ist. Die quantenmechanischen Rechnungen wurden unter Benutzung der Dichtefunktionalmethode M06-2X zusammen mit einem aug-cc-pVTZ Niveau des Basissatzes durchgeführt. Bei dem verwendeten hohen Niveau der Theorie CCSD(T) wurden Verfeinerungen der Energie mithilfe eines aug-cc-pVxZ (x = D, T, Q) Basissatzes und Extrapolation auf die gesamte Basissatzlimit (CBS) eingesetzt. Dafür wurde der Drei-Parameter-Ausdruck aug-Schwartz6(DTQ) in CBS verwendet. Der Tunneleffekt und die Behandlung der Innenrotation wurden ebenfalls in den KIE Berechnungen berücksichtigt. Zum ersten Mal wurde für das System Ethan + OH die Anharmonizität der Molekülschwingung betrachtet. Im Vergleich zu den experimentellen Ergebnissen sind die theoretisch berechneten KIE Werte ungefähr um einen Faktor von sechs überschätzt. Eine leicht negative Temperaturabhängigkeit der theoretischen KIE unterstützt jedoch den experimentellen Befund.

Implikationen der Verwendung von verbesserten KIE-Werten in den Untersuchungen zur isotopischen Fraktionierung von Ethan während seiner chemischen Abbau in der Atmosphäre werden diskutiert.

Acknowledgements

Contents

1 Introduction

1.1 Motivation and objectives

Volatile organic compounds (VOC) are released continuously in large amounts into the atmosphere from both natural and anthropogenic sources, affecting both air quality and human health. Some are highly efficient greenhouse gases, impacting on climate through their warming effect. During transport, VOC undergo chemical and physical processes which strongly influences the atmospheric chemistry. In the presence of NO and NO_2, VOC chemical degradation processes lead to ozone production [1], which is harmful to both humans and biotopes. A variety of other secondary organic compounds are formed during these processes, further damaging human health, air quality and the climate. Through VOC efficient oxidation, mainly by OH radicals, NO_3 and O_3, oxygenated VOC (OVOC) are formed. They are lower volatile, more water soluble and can be easily removed from the atmosphere. Therefore, these oxidation reactions are the most significant sink process of tropospheric VOC. Due to their lower vapor pressure OVOC can nucleate, forming new particles, or condense on existing ones. These particles may act as cloud condensation nuclei (CCN), forming clouds and thus, providing a cooling contribution to the atmosphere. A quantification of both warming and cooling contribution of VOC and their overall effect rely on accurate knowledge of sources, chemical and physical processes occurring during VOC transport, as well as on the sinks of VOC.

Stable isotope ratio measurements have been introduced to atmospheric science to better constrain sources and atmospheric processes occurring from emission to measurements. The fundamental concept used in application of stable isotopes is that they provide a 'fingerprint' for sources, i.e. trace gases emitted from different sources have a specific isotopic composition, the so called 'isotopic signature'. The isotopic composition of a single VOC changes moreover specifically during its chemical degradation, due to the

kinetic isotope effect (KIE) that is specific for each reaction. The KIE value ascertained to a chemical reaction can be theoretically or experimentally investigated

In the last decades, the techniques and instrumentation for the isotopic measurement have dramatically evolved, leading to remarkable improvement of the accuracy in determining the compound specific stable isotope ratio measurements of atmospheric gases in trace amounts. On the other side, the advancement of computational resources have allowed high levels of theory implemented in quantum mechanical calculations and statistical rate theory to gain molecular insights for different isotopes. However, there are few studies aimed to interpret ambient isotope ratio measurements [2-12]. Limitations for it are a lack of the necessary fundamentals on isotope effects of atmospheric reactions, as well as on the isotopic composition at emission sources.

Ethane was chosen as a prominent VOC to be investigated in this work, based on several reasons. Since it is a long-lived species, ethane is abundant in the temperature-varied atmosphere, impacting the tropospheric chemistry on hemispheric scales. Concentration and stable carbon isotopic ambient measurements are reported in the literature [2, 9-15]. Additionally, a KIE value of 8.57 ± 1.95 ‰ at room temperature (296 ± 4 K) for the reaction $C_2H_6 + OH$ was already measured by Anderson et al. [16], showing an uncertainty of 23% of the mean value. Based on this, Stein and Rudolph [17] estimated global ethane isotopic distribution employing chemical transport models. Yet, to better understand sources and sinks of tropospheric ethane by using isotopic studies, a very accurate KIE of its main degradation process is needed. However, the measurement of KIE for $C_2H_6 + OH$ in terms of improving the measurement precision as well as investigating its temperature dependence is experimentally challenging due to ethane's long lifetime. On the other side, the $C_2H_6 + OH$ reaction is a relative small reaction system that its KIE can be theoretically investigated at the highest level using existing computational power.

The objectives of this work are

1) to improve the precision of experimental measurement and to experimentally investigate the temperature dependence of stable carbon KIE for the oxidation reaction of ethane by hydroxyl radicals,

2) to theoretically determine stable carbon KIE and its temperature dependence for C_2H_6 + OH reaction at the molecular level,

3) to apply the observed stable carbon KIE and its temperature dependence in order to interpret ambient stable carbon isotopic ratio measurements.

This work presents the investigations of stable carbon KIE for the oxidation reaction of ethane by hydroxyl radicals in tropospheric relevant temperature range, using both experimental and theoretical approaches. The experimental stable carbon KIE study is presented in Chapter 2 including the description of experimental setup (Section 2.1) and procedure (Section 2.2), as well as experimental determined temperature dependence of KIE (Section 2.3). Theoretical stable carbon KIE calculations are described in Chapter 3. This includes theories (Section 3.1) and computational details (Section 3.2) employed to obtain the theoretically calculated KIE (Section 3.3). Implications of using the observed stable carbon KIE for ambient stable carbon isotopic ratio interpretation are discussed in Chapter 4.

1.2   Tropospheric ethane and its oxidation by hydroxyl radicals

Ethane (C_2H_6) is the second most abundant hydrocarbon in the troposphere, after methane. It is an important atmospheric organic trace gas, showing concentrations of 1049 ± 99 pptv on the Northern Hemisphere and 277 ± 34 pptv on the mid-Southern Hemisphere, averaged for the time period of 1984-2010 [18]. Its zonally monthly averaged mole fractions for 2006-2013 are illustrated in Figure 1.1 [19], showing a large seasonal and latitudinal variation. Lower concentrations in summer are due to the photochemical

removal by hydroxyl (OH) radicals. Ethane emission seasonal cycles contribute to winter maxima and summer minima. Larger mixing ratios in the Northern Hemisphere show that the majority of sources, mostly related to fossil fuel extraction, transport, processing and combustion, exist in this part of the globe. In the Southern Hemisphere, emissions from biomass burning are the main ethane source, being yet smaller comparing to fossil fuel usage. Overall, the global ethane emissions budget of 13 Tg yr^{-1} is composed of 8.0-9.2 Tg yr^{-1} originating from the production, transmission and processing of oil and gas, as well as 2.4-2.8 Tg yr^{-1} and 2.6 Tg yr^{-1} from biomass burning and biofuel combustion, respectively. There are also possible minor emissions from oceanic, biogenic and geological sources [17, 18, 20-22].
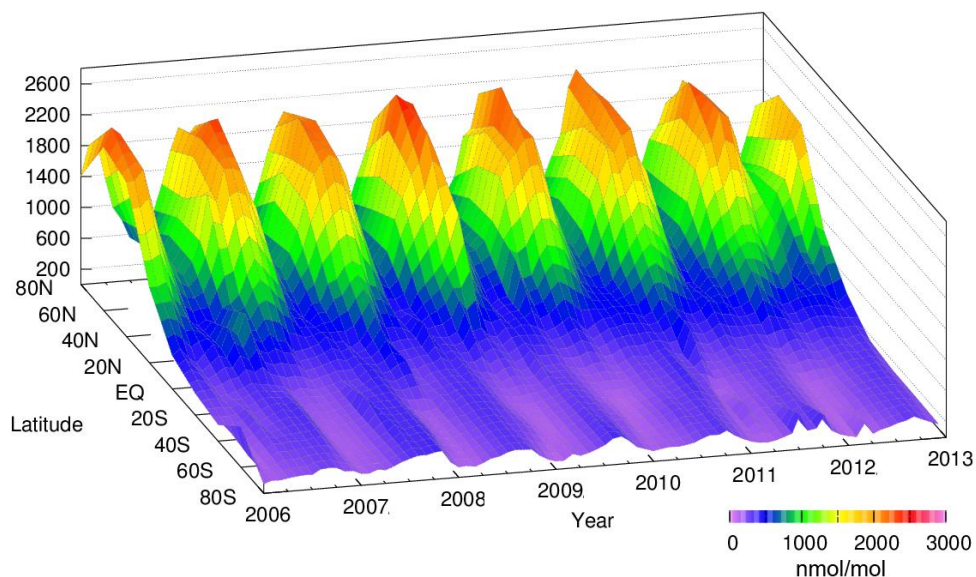
Figure 1.1   Variation of zonally averaged monthly mean ethane mole fractions. The zonally averaged mole fractions were calculated for each 20° zone. (Taken from Schultz et al. [19]).
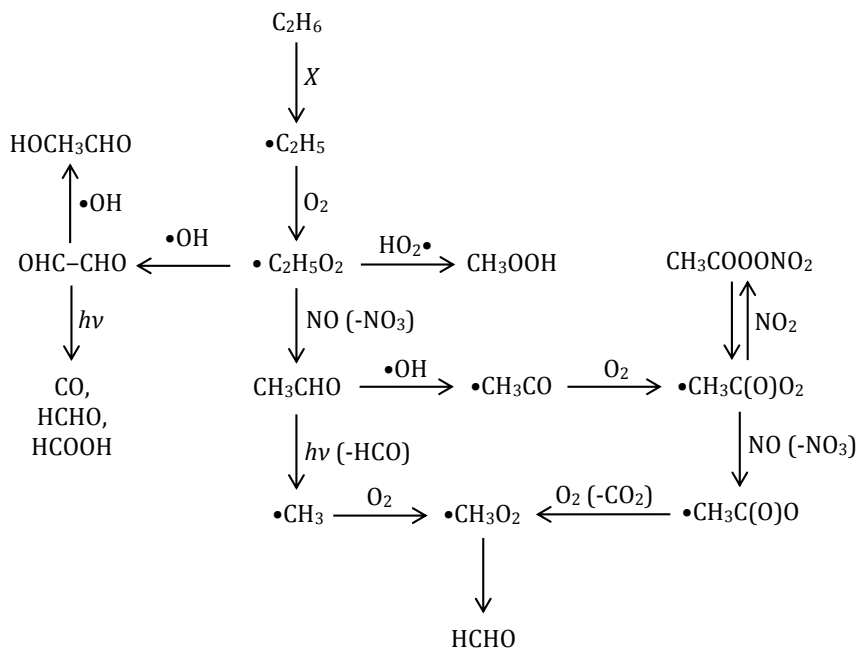
Figure 1.2 Degradation and transformation reactions of ethane (C_2H_6) which occur in the troposphere with the initial oxidants: X = hydroxyl radicals ($\bullet OH$), nitrate radicals ($\bullet NO_3$), or chlorine atoms ($\bullet Cl$), producing important intermediates: ethyl radicals ($\bullet C_2H_5$) and ethyl peroxy radicals ($\bullet C_2H_5O_2$). Typical products are acetyl peroxide (CH_3OOH), glyoxal ($OHC–CHO$), and acetaldehyde (CH_3CHO). Carbon monoxide (CO), formaldehyde (HCHO), formic acid (HCOOH), and glycolaldehyde ($HOCH_3CHO$) can be further produced from glyoxal. Multistep processing of acetaldehyde produces formaldehyde and peroxyacetyl nitrate ($CH_3COOONO_2$). (Adapted from Atkinson [23] and Möller [24])

Ethane is a precursor of tropospheric ozone, thus influencing the tropospheric chemistry. Loss processes of ethane occur neither via direct photolysis nor due to reaction with ozone (O_3) at measurable rates. Ethane reacts efficiently with the "cleansing" agents of the atmosphere, hydroxyl radicals (•OH), as well as with nitrate radicals (•NO_3) and chlorine atoms (•Cl). The hydrogen abstraction reactions produce ethyl radicals (•C_2H_5) and stable molecules (Reactions R1.1-R1.3) [23, 25].

$$C_2H_6 + \bullet OH \xrightarrow{k_{OH}} \bullet C_2H_5 + H_2O \qquad \text{(R1.1)}$$

$$C_2H_6 + \bullet NO_3 \xrightarrow{k_{NO_3}} \bullet C_2H_5 + HNO_3 \qquad \text{(R1.2)}$$

$$C_2H_6 + \bullet Cl \xrightarrow{k_{Cl}} \bullet C_2H_5 + HCl \qquad \text{(R1.3)}$$

where the reaction rate coefficients at 298 K are k_{OH} = 2.4 × 10^{-13} cm^3 molec^{-1} s^{-1}, k_{NO3} < 1.0 × 10^{-17} cm^3 molec^{-1} s^{-1} and k_{Cl} = 5.8 × 10^{-11} cm^3 molec^{-1} s^{-1}.

A sketch of tropospheric ethane degradation pathways is depicted in Figure 1.2. The highly reactive ethyl radicals produced by hydrogen abstraction of ethane (Reactions R1.1-R1.3) can further react with molecular oxygen, producing ethyl peroxy radicals ($C_2H_5O_2$•). Ethyl peroxy radicals can react with 1) hydroperoxyl radicals (HO_2•) yielding acetyl peroxide (CH_3OOH), 2) hydroxyl radicals yielding glyoxal (OHC-CHO), and 3) nitric oxide (NO) yielding acetaldehyde (CH_3CHO). Glyoxal can undergo either OH oxidation producing glycolaldehyde ($HOCH_3CHO$) or photolysis producing carbon monoxide (CO), formaldehyde (HCHO), or formic acid (HCOOH). The photolysis of acetaldehyde yields methyl radicals (•CH_3) that can further react with molecular oxygen (O_2) producing formaldehyde via an intermediate, methyldioxidanyl (•CH_3O_2). Multi-reactions of acetaldehyde with hydroxyl radicals, oxygen and nitrogen dioxide (NO_2) yields peroxyacetyl nitrate ($CH_3COOONO_2$) or PAN. Formaldehyde can be formed from reactions involving PAN, nitric oxide and oxygen. The compounds resulting from this chemistry impact on human health, air quality and climate. For instance, PAN is a toxic air pollutant and also a strong greenhouse gas, affecting additionally the tropospheric ozone [13].

Investigations of sources and processing of ethane are therefore of high interest. Since emissions of atmospheric ethane are mostly from sources on the continents, Cl atoms exist mainly in coastal and marine areas [26], and the reaction of ethane with nitrate radicals is very slow, the major ethane sink process is its reaction with the hydroxyl radicals (Reaction R1.1). Thus, the mean atmospheric lifetime of ethane is approximately 2 months, if the globally averaged OH concentration is approximately 10^6 molecules cm^{-3} [13, 20, 27].

There are various pathways for the OH radical to be generated in the troposphere [1]. Mainly, they arise from photo-dissociation of tropospheric ozone by solar UV in the presence of water vapor. The primary photolysis of ozone by UV light (wavelength, $\lambda \leq 340$ nm) produces atomic ($\bullet$O) and molecular oxygen (see Reaction R1.4) [24, 28]. Depending on the excitation energy, either the atom or both may be in electronically excited states.

$$O_3 + h\nu_{\lambda \leq 340\,nm} \rightarrow O_2(^1\Delta_g) + O(^1D) \tag{R1.4}$$

The $O(^1D)$ can further react with water vapor (H_2O), thus yielding hydroxyl radicals (see Reaction R1.5).

$$O(^1D) + H_2O \xrightarrow{k_{R1.5}} 2\bullet OH \tag{R1.5}$$

where the reaction rate coefficient is $k_{R1.5} = 4.0 \times 10^{-11}$ cm^3 molecule^{-1} s^{-1}

1.3 Chemical Kinetics of C_2H_6 + OH reaction

The rate determining step for the ethane oxidation by OH is represented by the initial process, i.e. hydrogen abstraction reaction (Reaction R1.1). Further radical reactions are much faster. For kinetic studies, the rate determining step is significant, therefore the focus of this study is on Reaction R1.1.

Chemical kinetics relates concentrations and time in form of rate laws and rate coefficients. The rate describing the change in the reactant concentration during the second order reaction C_2H_6 + OH is given by

$$Rate = -\frac{d[C_2H_6]}{dt} = -\frac{d[OH]}{dt} \qquad (1.1)$$

where $[C_2H_6]$ and $[OH]$ are the ethane and hydroxyl radicals concentrations, respectively, and t is time.

The corresponding rate law, relating it to the rate coefficient k is:

$$Rate = k[C_2H_6][OH] \qquad (1.2)$$

Combining Equations 1.1 and 1.2 results in:

$$-\frac{d[C_2H_6]}{dt} = -\frac{d[OH]}{dt} = k[C_2H_6][OH]. \qquad (1.3)$$

The requirement to simultaneously monitor the concentration of both reactants makes experimental studies on second order reactions challenging. A typical solution for this is to approximate the second order as pseudo-first order kinetics. For instance, if excess of OH is continuously introduced into the reaction system, its concentration effectively stays constant during the reaction. Thus, the observed pseudo-first order rate coefficient k_{obs} for C_2H_6 + OH can be expressed by:

$$k_{obs} = k[OH]. \qquad (1.4)$$

Thus Equation 1.3 becomes

$$-\frac{d[C_2H_6]}{dt} = k_{obs}[C_2H_6]. \qquad (1.5)$$

Equation 1.5 can thus be integrated from time = 0 to time = t giving:

$$ln \frac{[C_2H_6]_t}{[C_2H_6]_0} = -k_{obs}\, t = -k[OH]t \tag{1.6}$$

where $[C_2H_6]_0$ is ethane initial concentration, $[C_2H_6]_t$ is the concentration observed at time t and t represents the reaction time.

Consequently, the experimental rate coefficient of ethane oxidation reaction could be derived from the slope of a line fitted to concentration observations plotted as $\ln [C_2H_6]_t/[C_2H_6]_0$ vs. OH exposure ($[OH]t$).

Beyond that, a rate coefficient can be expressed by the Arrhenius Equation that shows the dependence of the rate coefficient on an absolute temperature in Kelvin $k(T)$, as well as the quantitative basis for a relationship between the activation energy and the reaction rate at which the reaction proceeds (see Equation 1.7).

$$k(T) = Ae^{-E_a/(RT)} \tag{1.7}$$

where A represents the pre-exponential Arrhenius factor, or frequency factor, E_a is the activation energy, and R is the gas constant.

1.4 Relative reaction rate approach

The relative rate method is usually employed to investigate the effect of using different experimental conditions on the reaction rate coefficient [29, 30]. Sometimes, due to experimental challenges, only rate coefficient ratios of two compounds concurrently reacting are determined instead of k absolute values. In this case, if the absolute value of one reaction rate coefficient is available in the literature, the second can be derived from the observed ratio. The relative rate method has many advantages comparing to absolute rate measurements. Only relative concentrations of the compounds of interest are necessary, increasing the accuracy of the results. Precisions of 5 % or better are common when employing this method. Additionally, relative rate experiments can be carried out

under conditions directly relevant to the atmosphere, e.g., very low reactant concentrations or low temperatures.

In this study, to test the consistency of the measured ethane and propane concentration decay during the experiments, the relative rate technique was applied. This approach bases on comparing the chemical degradation by OH oxidation of ethane and propane. An advantage here is that the OH radical, which is typically a highly reactive species, unstable and difficult to measure, doesn't need to be monitored in the experiments. Even if both OH radical reaction rate coefficients are reported [25], propane was used as reference while ethane was considered the target compound, since the four times longer life time of the latter might introduce higher uncertainties in experimental studies on oxidation reactions. k_{ethane} temperature dependence is recommended by the IUPAC Subcommittee on Gas Kinetic Data Evaluation for Atmospheric Chemistry [25] as follows:

$$k_{ethane} = 6.9 \times 10^{-12} \exp\left(\frac{1000 \pm 100}{T}\right) cm^3 \text{ molecule}^{-1} \text{ s}^{-1} \qquad (1.8)$$

where T corresponds to the temperature in Kelvin.

Propane is a suitable reference compound for this approach because following required properties are fulfilled:

i) C_2H_6 and C_3H_8 have similar physical and chemical properties, i.e. both are gases under the given experimental condition and contain the same chemical moieties. Additionally, for both molecules, the OH oxidation reactions are initiated by hydrogen abstraction, having comparable rate coefficients;

ii) they do not react with each other and cannot be regenerated by any reaction of their products;

iii) temperature dependent $k_{propane}$ values, recommended by the IUPAC Subcommittee on Gas Kinetic Data Evaluation for Atmospheric Chemistry [25], are derived from:

$$k_{propane} = 7.6 \times 10^{-12} \exp\left(\frac{-585 \pm 100}{T}\right) \text{cm}^3 \text{ molecule}^{-1} \text{ s}^{-1} \qquad (1.9)$$

where T corresponds to temperature in Kelvin. The values of $k_{propane}$ are listed in Table A.1 in the Appendix.

According to Reaction 1.1, the following concurrent reactions are investigated by using the relative rate method:

$$C_3H_8 + \bullet OH \xrightarrow{\ k_{propane}\ } \bullet C_3H_7 + H_2O \qquad\qquad (R1.6)$$

$$C_2H_6 + \bullet OH \xrightarrow{\ k_{ethane}\ } \bullet C_2H_5 + H_2O \qquad\qquad (R1.7)$$

where $k_{propane}$ and k_{ethane}, are the rate coefficients for the propane and ethane oxidation reactions, respectively. Since C_3H_8 and C_2H_6 are the reactants that react with the continuously added $\bullet$OH radicals, the second order reactions can be treated by pseudo first order approximation (see Section 1.3).

According to Equation 1.6 for propane and ethane, their concentration decay during the oxidation by OH is described as following:

$$ln \frac{[C_3H_8]_t}{[C_3H_8]_0} = - k_{propane}[OH]t \qquad\qquad (1.10)$$

and

$$ln \frac{[C_2H_6]_t}{[C_2H_6]_0} = - k_{ethane}[OH]t. \qquad\qquad (1.11)$$

Substituting $[OH]t$ by $\dfrac{1}{k_{propane}} ln \dfrac{[C_3H_8]_0}{[C_3H_8]_t}$ in Equation 1.11 yields:

$$\ln\frac{[C_2H_6]_0}{[C_2H_6]_t} = \frac{k_{ethane}}{k_{propane}} ln \frac{[C_3H_8]_0}{[C_3H_8]_t} \qquad\qquad (1.12)$$

By monitoring the concentrations of the precursors C_3H_8 and C_2H_6, the rate coefficient ratio $k_{propane}/k_{ethane}$ is experimentally obtained. Therefore, by plotting the concentrations of C_3H_8 versus C_2H_6 as functions of reaction time in form of $ln\left(\frac{[C_3H_8]_0}{[C_3H_8]_t}\right)$ vs. $ln\left(\frac{[C_2H_6]_0}{[C_2H_6]_t}\right)$, the rate coefficient ratio $\frac{k_{ethane}}{k_{propane}}$ is derived from the slope of the line fitted to the experimental data. Since the absolute value of the rate coefficient for propane OH oxidation is available from literature, the rate coefficient of C_2H_6 oxidation is derived as following:

$$(k_{ethane})_{\text{exp}} = (k_{propane})_{\text{lit}}\left(\frac{k_{ethane}}{k_{propane}}\right)_{\text{exp}} \tag{1.13}$$

As mentioned above, the relative rate technique has the advantage that only relative, not absolute concentrations of C_3H_8 and C_2H_6 need to be measured. Another advantage is the fact that there is no need to monitor the OH radical concentration during the experiments. Since OH is a highly reactive species, it is unstable and difficult to measure. Only the long lived C_3H_8 and C_2H_6 molecules, which are relatively easy to measure, need to be monitored. The accuracy of the results, however, depends critically on good knowledge of mechanistic details for the reaction system. Therefore, the kinetic analysis, which is not always straightforward in complex systems, must be valid. Furthermore, obtaining an accurate k_{ethane} from the rate coefficient ratio ($k_{propane}/k_{ethane}$) requires accurate knowledge of $k_{propane}$, the reference rate coefficient, as might be expected.

1.5 The kinetic isotope effect (KIE)

For carbon, there are two stable isotopes, ^{12}C and ^{13}C with relative abundances of approximately 98.9 % and 1.1 %, respectively. Due to the very small differences in the ratio of the number of stable carbon isotopes ($^{13}C/^{12}C$) in natural substances, the isotope ratios of investigated samples are typically expressed relative to the absolute ratio of the

internationally accepted reference standard, Vienna Peedee belemnite (VPDB), with a $(^{13}C/^{12}C)_{VPDB} = 0.0112372$ [31, 32], using the 'delta' notation. $\delta^{13}C$ is commonly expressed as its per mille value, as shown in the following :

$$\delta^{13}C_{sample} = \frac{(^{13}C/^{12}C)_{sample} - (^{13}C/^{12}C)_{VPDB}}{(^{13}C/^{12}C)_{VPDB}} \cdot 1000 \qquad /‰. \qquad (1.14)$$

Isotopologues refer to chemical substances with identical chemical structure but containing different isotopes of one or more of its atoms. Isotopologues differ by their isotope ratios, representing the number concentration of the heavier isotope relative to the lighter isotope number concentration. It's worth here pointing out that this work focuses on stable carbon isotope investigations on ethane with natural isotopic abundances. The probability that both carbon atoms are ^{13}C is extremely low. Therefore only two isotopologues of ethane are here referred, i.e. $^{12}CH_3^{12}CH_3$ and $^{13}CH_3^{12}CH_3$. They have an identical molecular electronic structure, but different molecular masses. Thus, they show different vibrational frequency properties.

Figure 1.3 shows the ground-state potential energy curve for the ^{12}C–H and ^{13}C–H bond dissociations using the harmonic and Morse (anharmonic) oscillator model. A diatomic harmonic oscillator is a simple model for the vibrational transition of chemical bonds. The vibrational frequency is inverse proportional to root of the mass. The heavier the isotope, the lower the frequency of vibration and the smaller the zero point energy. For the potential curve of this molecule, one of the nuclei will be fixed at the origin of the coordinate. The other nucleus will vibrate inside the potential well. The minimum of this well correspond to the equilibrium distance between both nuclei. The dissociation energy results by extracting the ZPE from the well depth. This means that for the heavier isotope the dissociation energy is higher. Morse potential explicitly includes the effect of bond breaking. In this case the distance between both nuclei is smaller for the heavier isotope (see Figure 1.3). Thus, the bounding in the isotopologue containing the ^{13}C is stronger. Another consequence of the higher molecular mass of ^{13}C is the lower collision frequencies for the heavier isotopologues. This will affect the pre-exponential Arrhenius factor.
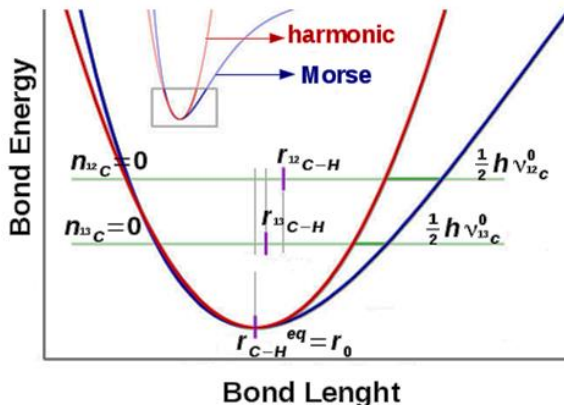
Figure 1.3 Molecular potential energy curve for a harmonic (red) and Morse (blue) oscillator model. Zero point energy levels are shown for ^{12}C and ^{13}C (for details see text).

Differences in ZPE and collision frequency due to isotopic replacement lead to slightly different rate for the reactions of pure ^{12}C reactant and those involving ^{13}C containing isotopologues. The result is measured in kinetic isotope effect (KIE). The stable carbon KIE is defined as:

$$KIE_{^{13}C} = \frac{k_{12}(T)}{k_{13}(T)}$$ (1.15)

where k_{12} is the rate coefficient of a reaction in which the reactant contains solely ^{12}C atoms and k_{13} is that of a reaction involving at least one ^{13}C atom. As shown in Equation 1.15, KIE is a ratio of temperature dependent rate coefficients. At lower temperatures, the probability that a vibrational degree of freedom is converted into a translational degree of freedom is much lower for heavier isotopologues. Moreover differences in collision frequencies are accentuated. Thus, a negative temperature dependence of KIE is expected.

Due to the KIE, the isotope ratio of the reactant changes during the reaction. For VOC oxidation reactions, molecules containing one ^{13}C atom typically show slightly slower

reaction rates than those with ^{12}C only, resulting in KIE values greater than unity. Based on KIE, during the reactions, the lighter isotopologues accumulate in the product, the heavier in the reactant. This translates in increasing $\delta^{13}C$ of reactant in the course of the reaction [33, 34]. Figure 1.4 visualizes the change in isotope abundances during β-pinene ozonolysis. The increase in $\delta^{13}C$ of reactant (β-pinene) becomes drastic at reactant conversion higher than 80 %. The major reaction product, nopinone in gas and particle phase, is initially depleted in [13]C. Due to β-pinene enrichment in ^{13}C in the course of reaction, $\delta^{13}C$ of the formed nopinone slowly increases too. At the end of reaction, the product $\delta^{13}C$ reaches the initial $\delta^{13}C$ value of reactant.
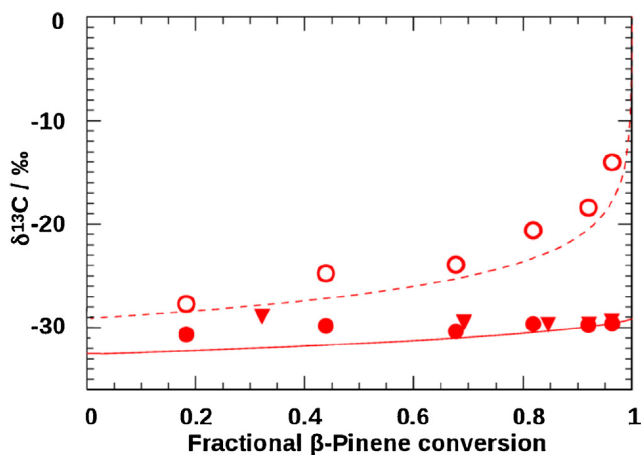
Figure 1.4   Evolution of $\delta^{13}C$ for β-pinene (open circle) and its main ozonolysis product nopinone in both gas (filled circle) and particle phase (up-side-down triangle) as function of fractional β-pinene conversion. The given lines are modeled $\delta^{13}C$ for β-pinene and nopinone when applying the the KIE for β-pinene ozonolysis. (Taken from Gensch et al. [34])

KIE experimental studies on atmospheric VOC oxidation reactions are scarce, and most of them report KIE values only at room temperature. Interpretation of ambient data using room temperature KIE may not be realistic due to the fact that the tropospheric temperatures can vary in the range of 180-320 K. Gensch et al. [33] found experimentally a negative KIE temperature dependence for β-pinene ozonolysis. They showed that the implementation of the observed parametrization KIE(T) in global modelling might lead to noticeable over- and underestimation of the predicted β-pinene atmospheric average chemical age (see Figure 1.5). Overall, KIE temperature dependence of atmospheric oxidation reactions of trace gases should be investigated in detail over the whole tropospheric relevant temperature range, since only accurate KIE values can be used to accurately interpret the age of air.

A negative KIE temperature dependence was also reported by theoretical studies for the reactions CH_4 + OH and CH_4 + Cl [35, 36] (see Figure 1.6). Both reports emphasize that the level of quantum mechanical theory implemented in the calculations, as well as the processes described in the employed statistical rate theory, such as tunneling effect, internal rotation and anharmonicity of molecular vibration, might drastically change the results.
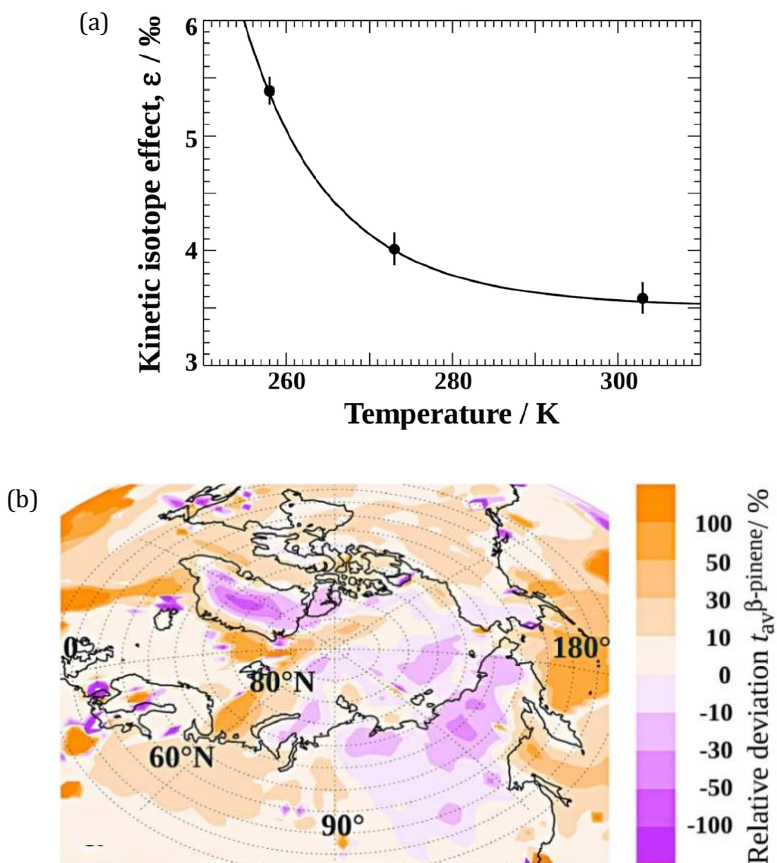
Figure 1.5   Experimentally derived KIE temperature dependence for *β*-pinene ozonolysis (a) and modeled relative difference in the isotopically determined atmospheric age of *β*-pinene near the surface between including and neglecting KIE temperature dependence for *β*-pinene ozonolysis (b). (Taken from Gensch et al. [33])

(a) KIE(^{12}C/^{13}C) vs T (K). Curves labeled MPW1K, MC3MPW, Gupta et al, Lasaga & Gibbs, MC3BB.

(b) ^{12}C / ^{x}C. k(Cl + ^{12}CH$_4$) / k(Cl + ^{x}CH$_4$) vs 1000 / T.

Legend:
- ^{13}C; Sauerssig 1995
- ^{13}C; Crowley 1999
- ^{13}C; Tyler 2000
- ^{13}C; Corchado 2000
- ^{13}C; Sellevag 2006
- ^{13}C (SCTST; TgDc)
- ^{14}C (SCTST; TgDc)
- ^{13}C (SCTST; TcTc)
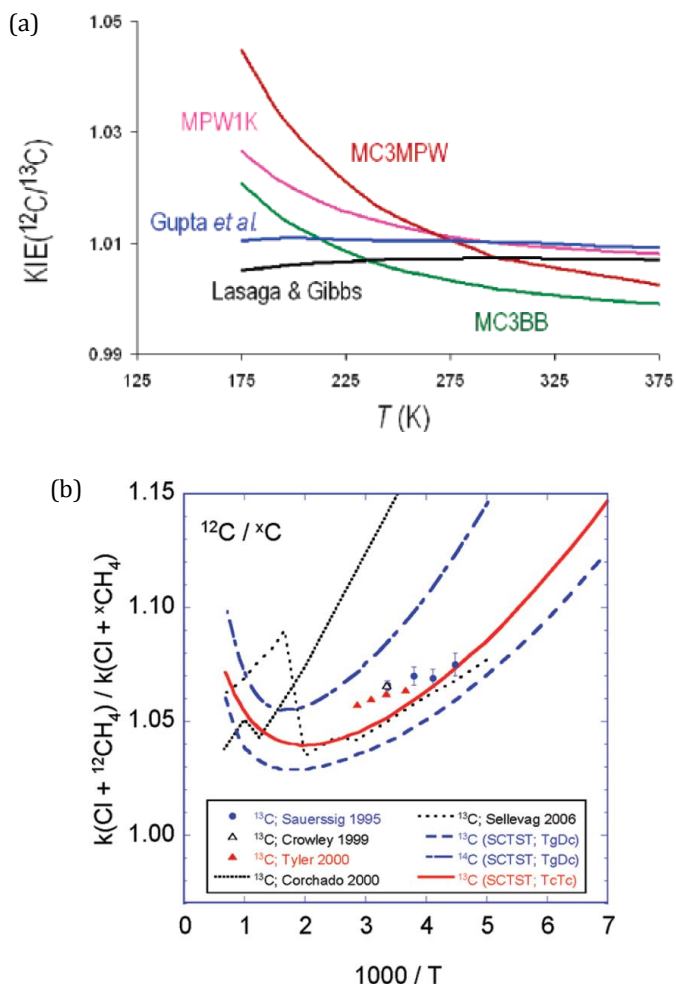
Figure 1.6 Theoretically calculated KIE temperature dependence at various levels of theory for the reactions CH$_4$ + OH (a, taken from Lin et al. [35]) and CH$_4$ + Cl (b, taken from Barker et al. [36]).

In this study, the following OH oxidation reactions of $^{12}CH_3^{12}CH_3$ and $^{13}CH_3^{12}CH_3$ were investigated:

$$^{12}CH_3{}^{12}CH_3 + \bullet OH \xrightarrow{k_{12}} \bullet^{12}CH_2{}^{12}CH_3 + H_2O \qquad \text{(R1.8)}$$

$$^{13}CH_3{}^{12}CH_3 + \bullet OH \xrightarrow{k_{13a}} \bullet^{13}CH_2{}^{12}CH_3 + H_2O \qquad \text{(R1.9a)}$$

$$^{12}CH_3{}^{13}CH_3 + \bullet OH \xrightarrow{k_{13b}} \bullet^{12}CH_2{}^{13}CH_3 + H_2O \qquad \text{(R1.9b)}$$
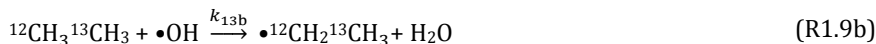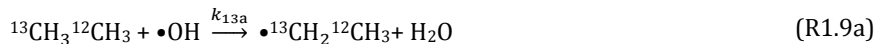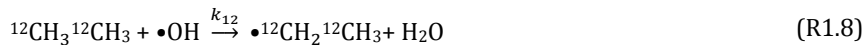
From the statistical thermodynamics point of view, the rate coefficients of these reactions depend on probabilities that reactants transform into products via a transition state. The probabilities of each statistic point along a reaction coordinate, i.e. reactants and a transition state, are expressed in term of partition functions. Thus, the temperature dependent rate coefficient $k_i(T)$ (i =12 or 13, for the reactions R1.8 to R1.9b), as from the expression $Rate = k_i(T)[^iC_2H_6][OH]$, depends on the partition functions. Details how partition functions can be linked with the experimentally measurable $k_i(T)$ are given in the Section 3.1.2.

For the $^{13}CH_3^{12}CH_3$ oxidation by OH radicals, the hydrogen abstraction can occur either at the ^{12}C or at the ^{13}C atom. This differentiation will be treated in detail in Section 3.3. At this point, the kinetics of the reaction involving one ^{13}C will be overall described by the rate coefficient k_{13}.

The rate laws of the pseudo first order for Reactions R1.8, R1.9a, and R1.9b containing different ethane isotopologues are deduced by using Equation 1.3:

$$\frac{-d[^{12}CH_3{}^{12}CH_3]}{dt} = k_{12}[OH][^{12}CH_3{}^{12}CH_3] \qquad \text{(1.16)}$$

$$\frac{-d[^{13}CH_3{}^{12}CH_3]}{dt} = k_{13}[OH][^{13}CH_3{}^{12}CH_3] \qquad \text{(1.17)}$$

For writing simplicity, $^{12}CH_3^{12}CH_3$ and $^{13}CH_3^{12}CH_3$ are denoted by ^{12}ethane and ^{13}ethane, respectively. Integrating Equations 1.16 and 1.17 results in:

$$ln\frac{[^{12}ethane]_t}{[^{12}ethane]_0} = -k_{12}[OH]t \tag{1.18}$$

$$ln\frac{[^{13}ethane]_t}{[^{13}ethane]_0} = -k_{13}[OH]t \tag{1.19}$$

Substituting $[OH]t$ by $-\dfrac{1}{k_{13}}ln\dfrac{[^{13}ethane]_t}{[^{13}ethane]_0}$ in Equation 1.18 yields:

$$\frac{1}{k_{12}}ln\frac{[^{12}ethane]_t}{[^{12}ethane]_0} = \frac{1}{k_{13}}ln\frac{[^{13}ethane]_t}{[^{13}ethane]_0} \tag{1.20}$$

Subtracting $\dfrac{1}{k_{13}}ln\dfrac{[^{12}ethane]_t}{[^{12}ethane]_0}$ on both sides of Equation 1.20 yields:

$$\left(\frac{1}{k_{12}}-\frac{1}{k_{13}}\right)ln\frac{[^{12}ethane]_t}{[^{12}ethane]_0} = \frac{1}{k_{13}}ln\frac{\frac{[^{13}ethane]_t}{[^{12}ethane]_t}}{\frac{[^{13}ethane]_0}{[^{12}ethane]_0}}. \tag{1.21}$$

By introducing the δ^{13}C and *KIE* definitions (Equations 1.14 and 1.15, respectively), Equation 1.21 becomes:

$$ln\frac{[^{12}ethane]_t}{[^{12}ethane]_0} = \frac{KIE}{1-KIE}ln\frac{\delta^{13}C_t+1000}{\delta^{13}C_0+1000}. \tag{1.22}$$

In this work, the experimentally determined concentration data are plotted against the corresponding isotopic composition measured at the same reaction extent, in form of $ln\{[^{12}ethane]_t/[^{12}ethane]_0\}$ versus $ln\{(\delta^{13}C_t+1000)/(\delta^{13}C_0+1000)\}$. The slope of the line fitted to the experimental data represents $KIE/(1-KIE)$. In the experimental study *KIE* is derived from:

$$KIE = \frac{\text{slope}}{1+\text{slope}}. \tag{1.23}$$

In the theoretical study, the KIE is determined explicitly from Equation 1.15. To do so, the absolute rate coefficients k_{12}, k_{13a}, and k_{13b} calculations are performed. The kinetics

parameters for reactions R1.8, R1.9a and R1.9b are evaluated using quantum mechanics calculations which are described in detail in Section 3.1.

Isotope fractionation effects are generally very small, similarly to stable isotope ratios. Therefore, the *KIE*, very near to 1, is presented as in per mille (‰) 'epsilon value':

$$\varepsilon = \left(\frac{k_{12}}{k_{13}} - 1\right) \cdot 1000‰. \tag{1.24}$$

1.6 Stable carbon KIE and number of carbon atoms

Rudolph et al. [4] showed a systematic dependency between the chemical structure of a homologous series of hydrocarbons and the reaction KIE. For the reaction of n-alkanes with OH radicals, KIE significantly decreases with increasing carbon number (N_C) (Figure 1.7). This is a consequence of the relation between the alkane molecular mass and their carbon atom number. For higher N_C in the homologous series, the differences in molecular masses (of heavier and lighter isotopologues) become less. For the ethane + OH reaction, authors also suggested that KIE values in the range of 4-5 ‰ are expected, instead of 6 ‰ predicted from extrapolation of inverse N_c dependency [4].

Anderson et al. [16] showed that the KIE (‰) of oxidation reactions by OH for n-alkanes with 2 to 8 carbon atoms by OH radicals can be predicted from inverse dependency on carbon number (N_C) of alkanes as following:

$$^{OH}\varepsilon = (16.6 \pm 1.0)\frac{1}{N_C}. \tag{1.25}$$

This approximation was derived from experimentally obtained KIE values. Ethane is included here, showing the highest uncertainty in the alkane series [16].
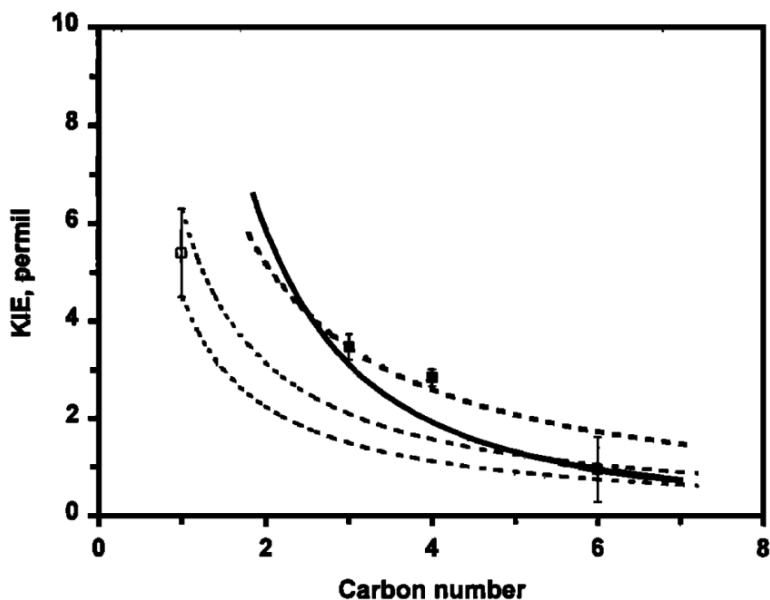
Figure 1.7 Dependence of the KIE for the reaction of n-alkanes with OH radicals on carbon number. Solid squares represent experimental data for n-alkanes from Rudolph et al. [4] and open square represents methane KIE experimentally determined by Cantrell et al. [37]. The solid line was obtained from a semi-empirical dependence based on a very simplistic structure reactivity relationship concept (for details, see text). The two thin dash lines indicate the KIE expected range, in case the hydrogen abstraction KIE deduced form the reported methane KIE. The thick dash line represents the calculated KIE from the inverse dependence of the KIE on carbon atom number, considering that the hydrogen abstraction from a carbon atom by OH results in KIE = 10 ‰. (Taken from Rudolph et al. [4])

Additionally, the KIE values for reactions of alkanes with OH radicals can be predicted by ^{13}C Structure-Reactivity Relationship (SRR) [16]. SRR is a semi-empirical approach, using a very simplistic structure reactivity relationship concept, based on the

mass dependence of the collision frequency factor. Both methods show good agreement. Though, these predictions underestimate the KIEs for alkanes with more than four carbon atoms and also cannot elucidate the differences in KIE between alkane isomers.

1.7 The "Isotopic hydrocarbon clock"

VOC with well-known chemistry can be used as tracers to investigate processes which are not directly measurable. Tracers contribute to determine the photochemical age of air masses and thus, to better apportion VOC sources. The challenge of these studies is to differentiate among mixing, chemical degradation and other loss processes occurring from emission to measurement. Within the "Hydrocarbon clock" concept, which handles solely the chemical loss of VOC, the photochemical age of air masses can be determined from the concentration ratio decay over time of two compounds with similar atmospheric lifetimes. Beside the necessity of comparable reactivity for the co-emitted species, their emission factor ratio must be known, in order to be employed as complementary tracers. Rudolph and Johnen [38] found very good agreement for the average age of an investigated air mass relative to the atmospheric n-butane derived from observed concentration ratios of three different alkane pairs (i.e. propane/ethane, *n*-butane/ethane and *i*-butane/ethane). Yet, this technique is applicable only if certain strongly simplifying assumptions are made.

In the case of stable carbon isotopes, the requirements to use ^{12}C and ^{13}C as co-emitted tracers are fulfilled. They are emitted with same emission factors. Moreover, their relative loss rate can be experimentally determined (KIE). Since KIE values are very near to unity, both tracers have similar lifetime. This and very small isotopic effects make possible to use a linear approximation of the isotope ratio changes during atmospheric processing. Consequently, Rudolph and Czuba [3] developed the so called "Isotopic hydrocarbon clock":

$$\delta^{13}C_t = \delta^{13}C_0 + t_{av}[OH]_{av}k_{OH}{}^{OH}\varepsilon \qquad (1.26)$$

where $\delta^{13}C_0$ and $\delta^{13}C_t$ represent the isotopic composition of the emission and at the observation site, respectively, $t_{av}[OH]_{av}$ is the average photochemical age, k_{OH} is the rate coefficient, and $^{OH}\varepsilon$ is the KIE of the oxidation reaction of the compound of interest by OH radicals. That means, at known source $\delta^{13}C_0$ and KIE of the chemical processing of a single compound, the fractional conversion can be determined based on its isotopic composition.

In atmospheric research, stable isotope ratio investigations are considered to be a useful tool to learn more about source apportionment and to quantify atmospheric processing. From $\delta^{13}C$ measurements of light hydrocarbons over the western North Pacific, Tsunogai et al. [14] ruled out ethane fresh emissions in maritime atmospheres. Irei et al. [39] quantified, based on information on the isotopic fractioning of low-volatile water-soluble organic aerosol (LV-WSOC) in ambient samples collected in western Japan, the extent of their atmospheric photo-oxidation. Additionally, they determined the mixing contribution of freshly emitted aerosol in the observed air masses. A similar KIE study, differentiating the effects of dilution processes and photochemical degradation of toluene in the free troposphere was carried out by Wintel et al. [8]. These studies are yet very scarce.

The "Isotopic hydrocarbon clock" is a good tool to interpret global modelling results. Stein and Rudolph [17] used global three-dimensional chemical-transport-modelling to predict the ethane isotopic ratio distribution on both hemispheres. Comparison between model estimations and observations demonstrated the existence of unidentified ethane sources. While concentration data alone provided only information on type of missing sources, isotopic analyses could differentiate between mixing and chemical losses of ethane. The use of stable isotopes for process understanding within the atmospheric research is therefore a highly innovative field.

2   Experimental KIE measurement for C_2H_6 + OH

The KIE temperature dependence of the ethane oxidation by hydroxyl radicals was studied experimentally. Thermal Desorption - Gas Chromatography - Combustion - Isotope Ratio Mass Spectrometry (TD-GC-C-IRMS) was employed to follow the changes in concentration and $\delta^{13}C$ along the reaction. A relative study of propane oxidation reaction by hydroxyl radicals was performed as a verification of chemistry for the ethane reaction. The experimental instrumentation (Section 2.1), methods and procedures (Section 2.2), as well as the experimental results (Section 2.3) are described in this chapter.

2.1   Instrumentation

Figure 2.1 displays an overview of the setup used to determine the KIE temperature dependence of the ethane oxidation by hydroxyl radicals. This consists of:

i)   a temperature controlled reaction chamber, where oxidation reactions were carried out at constant temperature;

ii)   a thermal desorption (TD) unit for pre-concentration and focusing of the samples;

iii)   a separation unit – the gas chromatograph (GC) - to separate the individual chemical components of the sample;

iv)   a combustion (C) unit – to quantitatively oxidize the organic compounds to CO_2 and H_2O;

v)   a detection unit - the isotope ratio mass spectrometer (IRMS) - to measure the stable carbon isotope ratios of the compounds of interest.

In this section, a detailed description for each instrumental part, including the parameter choices for optimal reaction, separation and detection performances is presented.
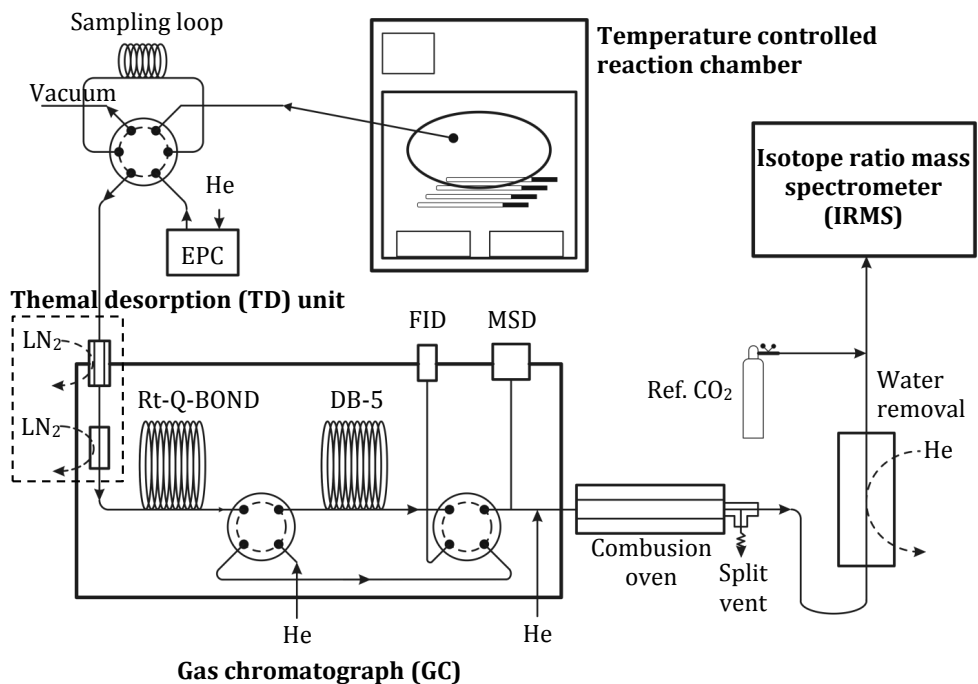
Figure 2.1   Experimental setup, adapted from Anderson et al. [40]. (for details see text)

2.1.1 Temperature controlled reaction chamber

The oxidation reaction of ethane and propane by hydroxyl radicals (OH) was carried out in the temperature controlled reaction chamber (Figure 2.1). Studying the KIE temperature dependence of this reaction requires accurate temperature control. A temperature controlled oven that houses the reaction chamber was optimized in this work to achieve temperature control in the range of 243-303 K. Its construction (Figure 2.2) was specially designed to control and stabilize the temperatures lower than room temperature. The stainless steel housing of 7 cm thickness, filled with mineral wool, thermally isolates the oven contents from its surroundings. For cooling, liquid nitrogen (LN_2) is introduced through two inlets at the top of the oven. To obtain isothermal conditions during the reaction, two heaters equipped with rotary fans, located at the base, were used. The

temperature is set and stabilized by using a digital controller that regulates the switches of liquid nitrogen valve and the heater operation. A proper coordination of the described components in the required configuration offers accurate temperature control of the reaction chamber (see below).
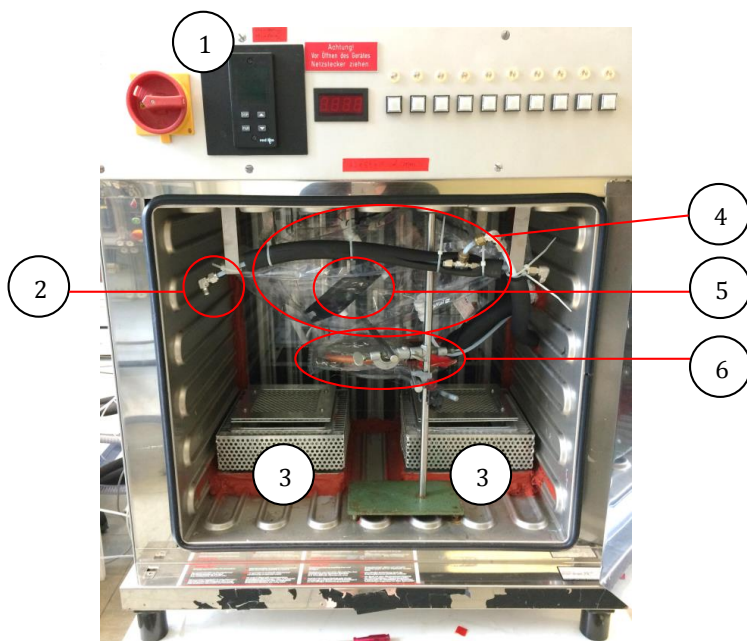
Figure 2.2   Temperature controlled reaction chamber. 1 = Temperature controller. 2 = Liquid nitrogen inlet. 3 = Heaters and rotary fans. 4 = FEP reaction chamber. 5 = rotary fan inside the chamber. 6 = UV lamps inside heating enclosure.

The reaction chambers, where oxidation reactions of ethane and propane by OH take place, were made from FEP film of 0.083 mm thickness. One chamber requires one film sheet of 140 cm × 60 cm. Each FEP film sheet was folded once in half and sealed on every side and edge using a handheld heating sealer. The obtained enclosure of circa 12 L has a rectangular form, approximately sizing 65 cm × 55 cm.

An axial rotary fan (4710KL, NMB Minebea GmbH, Germany) was installed inside the chamber to mix the gases, thus keeping the temperature as well as mixing ratios of trace gases homogeneous. Two Teflon ports, equipped with manual gas valves, were installed at the bottom of the chamber. One was used as inlet for introducing the reactant gases, the other was reserved as outlet for gas mixture sampling via a vacuum line. Two additional Teflon ports equipped with septa are needed for powering the rotary fan.

Every three experiments, a new chamber was built, to prevent contamination and leakages. The suitability of each fabricated chamber to be used for experiments was tested in three steps. Firstly, the sealing lines as well as the four Teflon ports of the chamber were examined visually for gaps or tears. Then, the chamber was filled with Helium and subsequently tested for leaks with an electronic leak detector (22655, Restek Corporation, USA) along the sealing lines and Teflon ports. Finally, the fully filled chamber was left for at least one hour to observe any reduction of chamber volume. Chambers showing leakages were either repaired or discarded.

To initiate OH radical formation by H_2O_2 photolysis, four mercury UV lamps (Analamp 81-1127-01, BHK Inc., USA, λ_{max} = 254nm, I_{max} = 508 $\mu W \cdot cm^2$) were installed below the chamber [41]. The lamps were maintained at 293 - 303 K inside a heater enclosure, to prevent any shifting in maximum wavelength and intensity of emitted UV light when initiating the H_2O_2 photolysis. Therefore, an assembly of a heating tape (HEW-THERM 90 SBL-CT ATEX, HEW-KABEL GmbH, Germany) and aluminum foil enclosed in a 15 cm × 20 cm double layers FEP bag were built around the lamps. The enclosure was purged by warm N_2 gas ($\sim$ 323 K) to condition the temperature of the lamps during the low temperature experiments.

The temperature stability of the oven was characterized at 303, 288, 273, 263, 253 and 243 K. Two thermocouples were introduced at the base and rear side of the reaction chamber, to monitor temperatures at different locations in the oven. The temperatures were recorded manually every minute for a duration of 80 minutes. The recording started 10 minutes after switching on the controller. Temperature profiles at different set points are displayed in Figure 2.3. The average, uncertainties and maximum deviation from average at the base and rear side are summarized in Table 2.1 and Figure 2.3, showing a very high stability during the testing time. Due to the rotary fan inside the chamber, a constant temperature, consistent with the temperature in the oven, was reached inside the FEP bag after 5 to 15 minutes. Furthermore, operating of the UV lamps did not have an influence to the temperature stability of the oven in the described temperature range.

Table 2.1 Average, uncertainties and maximum deviation from average (values in brackets) for temperatures measured at rear side of reaction chamber and at the oven base.

Set point, K	Average measured temperature, K	
	rear side of reaction chamber	oven base
303.0	303.0 ± 0.1 (0.2)	303.0 ± 0.1 (0.2)
288.0	288.0 ± 0.2 (0.3)	288.0 ± 0.1 (0.2)
273.0	272.7 ± 0.3 (0.7)	273.0 ± 0.1 (0.2)
263.0	262.9 ± 0.3 (0.8)	263.0 ± 0.1 (0.4)
253.0	253.2 ± 0.3 (0.6)	253.0 ± 0.2 (0.5)
243.0	242.7 ± 0.3 (0.7)	243.0 ± 0.2 (0.6)
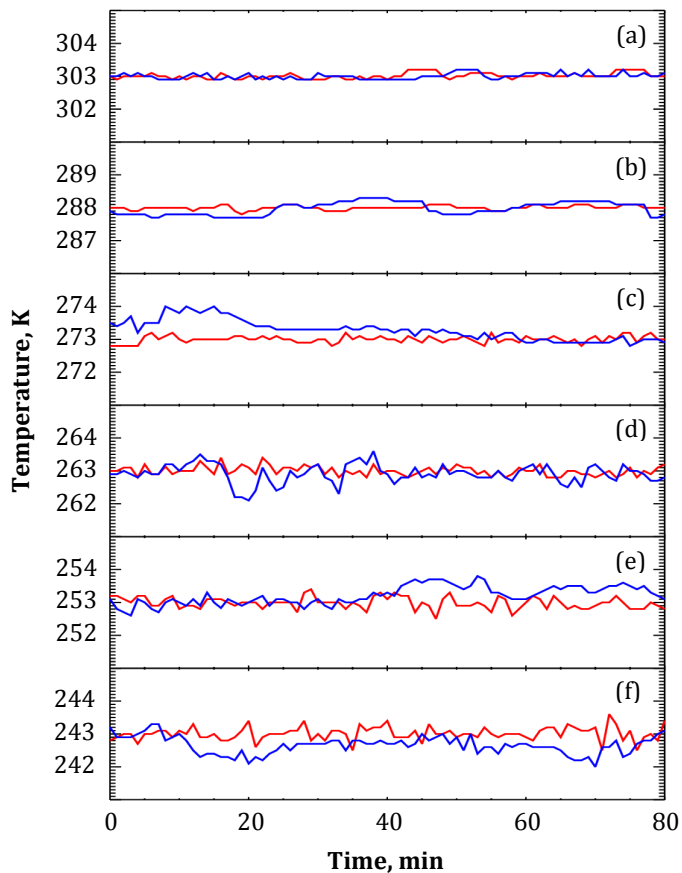
Figure 2.3 Temperature profiles of the oven for different set points; (a) 303 K, (b) 288 K, (c) 273 K, (d) 263 K, (e) 253 K, and (f) 243 K. The temperature was measured at rear side of reaction chamber (blue line) and at the oven base (red line).

2.1.2 Thermal desorption - gas chromatography – combustion - isotope ratio mass spectrometry (TD-GC-C-IRMS)

Isotope ratio measurements of the gas phase components sampled from the reaction chamber were carried out during the course of the reactions. The TD-GC-C-IRMS is depicted in Figure 2.1. Each measurement involved 1) gas mixture sampling and transfer from the temperature controlled reaction chamber to the pre-concentration unit, 2) cryogenic sample focusing and subsequent thermal desorption in the pre-concentration unit, 3) individual compound separation, including ethane and propane, by gas chromatography, 4) conversion of ethane and propane into CO_2 in the combustion furnace, and 5) analysis for concentrations and delta values by IRMS.

To transfer the gas mixture samples from the temperature controlled reaction chamber to the pre-concentration unit, a 10 mL stainless steel sample loop (SL) mounted on a six port valve was used. The 1/8" transfer lines were either of Teflon (inside the oven) or of stainless steel (outside the housing). A manual 'on-off' gas valve was fixed between the reaction chamber and the six-port sampling valve to control the transfer step, either allowing the sample to be taken from the chamber, or isolating the chamber from the sampling system. A needle valve and a mass flow controller located between sampling valve and a diaphragm pump controlled the flow rate of gas samples through the sample loop. The flow rate of the carrier gas (He, 99.9999 %, AIR LIQUIDE Deutschland GmbH, Germany) used to transfer the sample from the sampling valve to the pre-concentration unit was controlled by an Electronic Pneumatic Control (EPC) unit. All transfer lines, the sample loop as well as the sampling valve were maintained at 333 K, to prevent condensation of trace gases and their products before reaching the pre-concentration unit.

A custom-built pre-concentration unit – Thermo Desorption System Large (TDSL) (GERSTEL GmbH & Co. KG, Germany), described in detail by Iannone et al. [42], was adapted to fulfill the requirements of optimal focusing of ethane and propane prior to the GC injection. Due to high concentrations of ethane and propane in the gas samples, only the

second and third cryogenic traps were utilized, i.e. the Cooled Injection System (CIS) and the Cryogenic Trapping System (CTS). Since the compounds of interest, ethane and propane, are light hydrocarbons, the CIS was equipped with a deactivated quartz inlet liner (L = 71 mm, OD = 3mm, ID = 2mm), packed with a suitable adsorbent for C1-C4 alkanes, Carbosieve S-III (60-80 mesh, Sigma-Aldrich Corporation, USA). To improve the mixture focusing, the CTS additionally cryogenically trapped the sample at the top of the column.

The GC (6890 G1530A, Agilent Technologies, USA) was equipped with two columns. The first column was a Rt-Q-BOND column (30m length, 0.32mm i.d, 10µm film thickness, Restek Corporation, USA), which gave an optimal separation for C1-C4 hydrocarbons. Utilization of the Rt-Q-BOND column gave excellent peak resolution for ethane. The second column, a low polar DB-5 column (30m length, 0.32mm i.d., 0.25µm film thickness, Restek Corporation, USA), was employed to reach optimal propane separation, which elutes together whit propene in overlapped peaks from the first column. Therefore, the time window of the first chromatogram from 46 to 80 minutes was sent on the second column. The EPC dynamically adjusted the column inlet pressure of the carrier gas He, as a function of the GC oven temperature program. The aim was to achieve constant flow conditions throughout the whole separation process. A valve system allowed to choose different operating configurations, regarding either the transfer (on a single or on both columns), or the used detection system (FID or MS/IRMS) (Figure 2.1).

Three detectors were used during the experiments: a Flame Ionization Detector (FID) (Agilent Technologies, USA), mainly used for GC separation method development, a Mass Spectrometry Detector (MSD) (5975C, Agilent Technologies, USA) for peak identification and purity verification, and an Isotope Ratio Mass Spectrometer (IRMS) (IsoPrime, Micromass Ltd., UK) for measuring concentration and isotope ratios of the compounds of interest. In this work, selected segments of GC eluate solely containing ethane (from Rt-Q-BOND column) and propane (from DB-5 column) were directed to MS and IRMS for peak identification and isotopic ratio determination, respectively. The portions of GC eluate with no ethane and propane were sent to the FID (Figure 2.4).

For isotopic measurements, approximately 80 % of the total flow is transferred to a combustion interface, which converts the hydrocarbons to CO_2 and water. The interface, heated to at 850°C, consists of a quartz tube packed with 0.1-0.5 mm CuO particles for 12 cm. The water is then removed by passing the CO_2/H_2O stream through a tubular Nafion permeation dryer (0743390, Thermo Fisher Scientific Inc., USA).

Following the combustion process, dry CO_2 is introduced to the ion source of the IRMS instrument via an open split. CO_2 is ionized by electron ionization of 68.07 eV and separated by a magnetic field into three ion beams of m/z 44 ($^{12}C^{16}O^{16}O$), 45 ($^{13}C^{16}O^{16}O$ and $^{12}C^{17}O^{16}O$), and 46($^{12}C^{18}O^{16}O$, $^{13}C^{17}O^{16}O$, and $^{12}C^{17}O^{17}O$). The ion beams are simultaneously detected using three Faraday cup collectors, precisely positioned in the magnetic field. The ion currents are subsequently amplified, to result in comparable signals. These are continuously acquired and stored for the evaluation of the chromatograms.

For isotope ratio measurement calibration, CO_2 reference gas is online injected in 'open-split' modus, before and after eluting the peaks of interest. The working standard (WS) used in the measurements was calibrated against VPDB [32].

The quality control of isotopic measurements was achieved by regularly carrying out linearity and stability tests. Linearity test showed that the IRMS worked properly in the range of 0.3 nA and 8.8 nA (representing circa 0.45-13.31 pg ethane and 0.40-11.86 pg propane, correspondingly) with average ^{45}R and ^{46}R (see Equations 2.1 and 2.2) of $1.16384 \pm 0.00028 \times 10^{-2}$ (0.024 %) and $3.9977 \pm 0.0037 \times 10^{-3}$ (0.093 %), respectively. The sensitivity of TD-GC-C-IRMS for ethane and propane were found to be 1.51×10^{-3} and 1.35×10^{-3} ng nA^{-1}, correspondingly. The experiments were initiated only if three consecutive stability tests gave standard deviations of ratios ^{45}R and ^{46}R less than 0.1 %.

Three software packages were involved in the fully automatic regulation of the different steps of the experimental method: TDGL Large V0.5 (GERSTEL GmbH & Co. KG, Germany) to control the thermal desorption and give the start signal for the GC program; MSD ChemStation E.02.00.493 (Agilent Technologies, USA) to operate the GC and analyze

the chromatograms, as well as to give the start signal for the sampling procedure; MassLynx Inorganic Build 4.0.0.792 (GV Instruments Ltd., UK) to control IRMS, to acquire and evaluate the isotopic data.

2.2 Method and procedure

Prior to each experiment, the reaction chamber was cleaned by pumping out the air from inside. The oven was heated to 313 K. Ultrapure nitrogen (N_2, 99.9999 %, Linde AG, Germany) was filled into the bag, kept for 30 minutes and then flushed out. The procedure was repeated three times. A blank concentration measurement was carried out, to test the cleanliness of the bag. Examples of chromatograms obtained during the blank concentration measurements are shown in Section A.1.1 (see Appendix, Figures A.1 and A.2).

150 to 300 μL Ethane (C_2H_6, 99.95 %, Linde AG, Germany) and 150 μL propane (C_3H_8, 99.95 %, Linde AG, Germany) were separately introduced to the reaction chamber using a 150 μL gas loop fixed on a four-port valve. The gases were flushed in by ultrapure nitrogen.

OH radicals, necessary for the oxidation of ethane and propane, were generated by the photolysis of hydrogen peroxide, H_2O_2 [2]. Therefore, gaseous H_2O_2 was prepared by injecting 2.5 to 10.0 mL liquid hydrogen peroxide (H_2O_2, 50 %wt in H_2O, Sigma-Aldrich Corporation, USA) into a 6 L low-level reactive canister (SilcoCan 24182-650, Restek Corporation, USA) under vacuum. This was subsequently pressurized to 2.5 bars using ultrapure nitrogen. Finally, 9 L of gaseous H_2O_2 was added to the ethane/propane mixture into the chamber.

The oxidation reactions were initiated by turning the UV lamps on. Hydroxyl radicals were generated by H_2O_2 photolysis (Reaction R2.1) and initiated the oxidization of

ethane and propane by hydrogen abstraction from a carbon atom (Reactions R1.1 and R2.2).

$$H_2O_2 + h\upsilon_{\lambda=254nm} \rightarrow 2\bullet OH \qquad\qquad (R2.1)$$

$$C_2H_6 + \bullet OH \rightarrow H_2O + \bullet C_2H_5 \qquad\qquad (\text{see Reaction R1.1})$$

$$C_3H_8 + \bullet OH \rightarrow H_2O + \bullet C_3H_7 \qquad\qquad (R2.2)$$

For each experiment at a constant temperature, twelve to eighteen gas samples of 10 mL were automatically taken from the temperature controlled reaction chamber and isotopically analyzed by TD-GC-C-IRMS. The time needed for a complete TD-GC-C-IRMS analysis was limited by the chromatographic separation of ethane and propane. Therefore, after the reaction started, every 1.5 hours a gas mixture sample was taken from the reaction chamber and the concentration, as well as the stable carbon isotopic ratio of the reactants ethane and propane were measured. After opening the sampling valve, the sample loop was filled at a flow rate of 2 mL min^{-1} with the gas mixture. Stability tests for the IRMS were carried out by ten CO_2 reference gas injections, each for 30 seconds.

An optimal VOC focusing prior to the GC separation was achieved through alternatively cooling-heating of the two used cryogenic traps. Therefore, the CIS was firstly cooled to 153 K by using liquid nitrogen. After reaching the programmed temperature, the 10 mL sample was transferred from the sample loop by using a flow of 2.5 mL min^{-1} Helium (He, 99.995 %) as a carrier gas. The VOC were trapped for 10 min and then thermally desorbed at 573 K. The heating rate for the CIS was 1 K sec^{-1}. Thus, the VOC mixture was quantitatively transferred to the CTS, cooled at 123 K. Finally, the CTS was instantly heated to 453 K at a rate of 10 K sec^{-1}, allowing the GC separation process to start. For all experiments, the GC temperature program started at 243 K, ramped at a rate of 5 K min^{-1} to 423 K, being held there for 4 minutes. The duration of one measurement starting from sample transfer until completion of GC analysis was 80 minutes. The rest of 10 minutes till starting the next sampling was used to prepare the cryogenic traps and the GC oven for the following measurement. The sequence of events and corresponding temperature program are given in Table 2.2 and visualized in Figure 2.4.

The separated VOCs were transferred into the MSD partly, and into the combustion interface, being quantitatively oxidized to CO_2 and water [43]. The latter was removed by the Nafion membrane, whereas the CO_2 was transferred to the IRMS. The chromatogram, shown in Figure 2.5 illustrates the optimal base line separation of ethane (retention time, RT = 43 min) and propane (RT= 57 min). Additionally, the 15 CO_2 reference gas peaks are shown, introduced for 30 sec each time. Due to the linearity range determined during the characterization measurements, isotopic ratios of VOC showing peak heights lower than 0.3 nA were not comprised in the data analysis. Examples of chromatograms measured with FID, MSD and IRMS are shown in section A.1.2 (see Appendix). Please note that FID was operated to verify that entire VOCs were completely analyzed by IRMS and MSD.

Table 2.2 The events of the TD-GC-C-IRMS method together with the corresponding temperature program for one measurement.

Time, min	Events	T, K			T rate, K min^{-1}
		CIS	CTS	GC	
|	Sampling: chamber → SL	153	123	243	–
0	Transfer, 1st cryogenic-trapping: SL → CIS	153	|	|	–
10	Thermal desorption, 2nd cryogenic trapping: CIS → CTS	573	123	|	60
29.5	Thermal desorption: CTS→ GC	|	453	243	600
30	GC Separation on Rt-Q-BOND (RT$_{ethane}$ = 43 min)	|	|	423	5
46	GC Separation on DB-5 (RT$_{propane}$ = 57 min)	|	|	|	–
80	End of measurement	573	453	423	–
90	Start of next measurement (as time = 0)	153	123	243	–
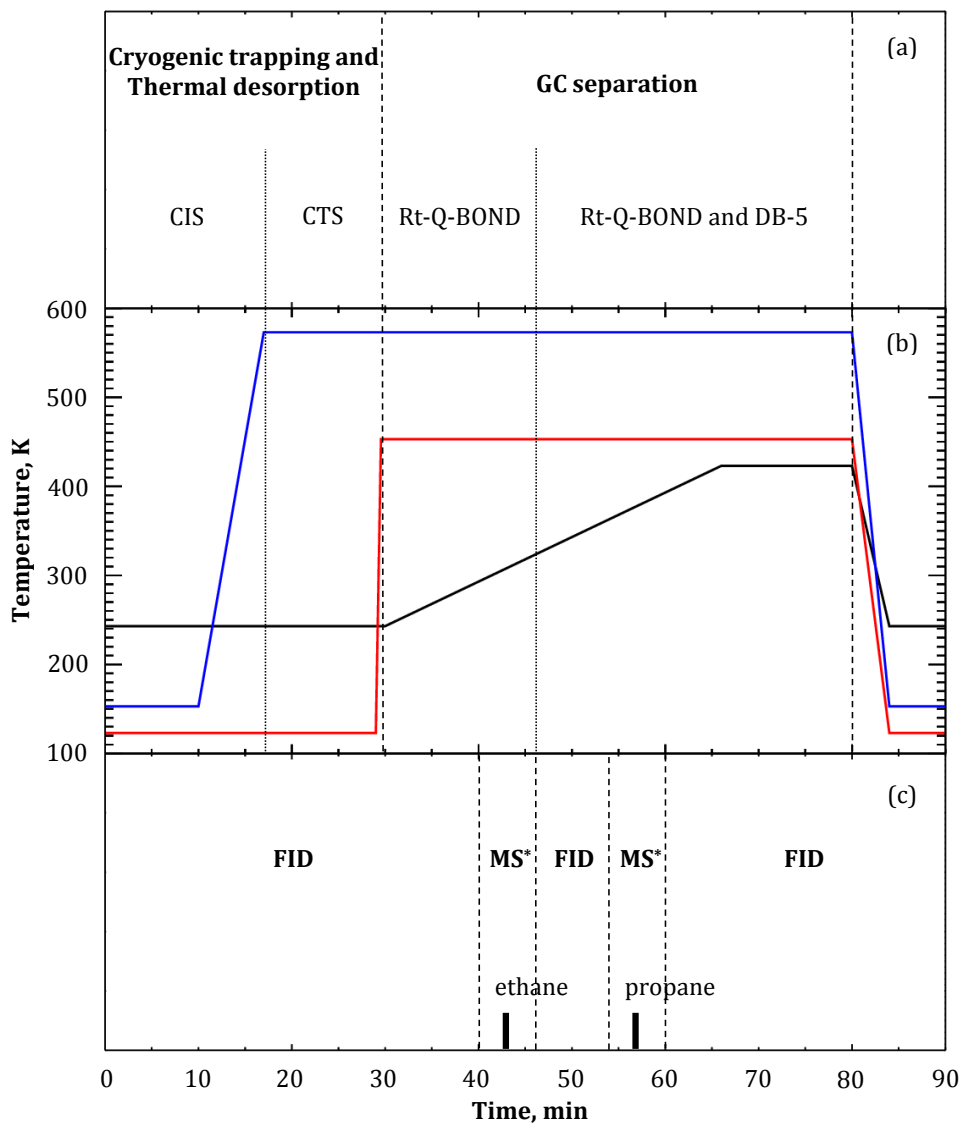
Figure 2.4 Events of TD-GC-C-IRMS method (a) together with the corresponding temperature programs of CIS (blue line), CTS (red line), and GC oven (black line) for one measurement (b), and events of detector selection as well as retention time for ethane and propane (c) (*MS = MSD + IRMS).
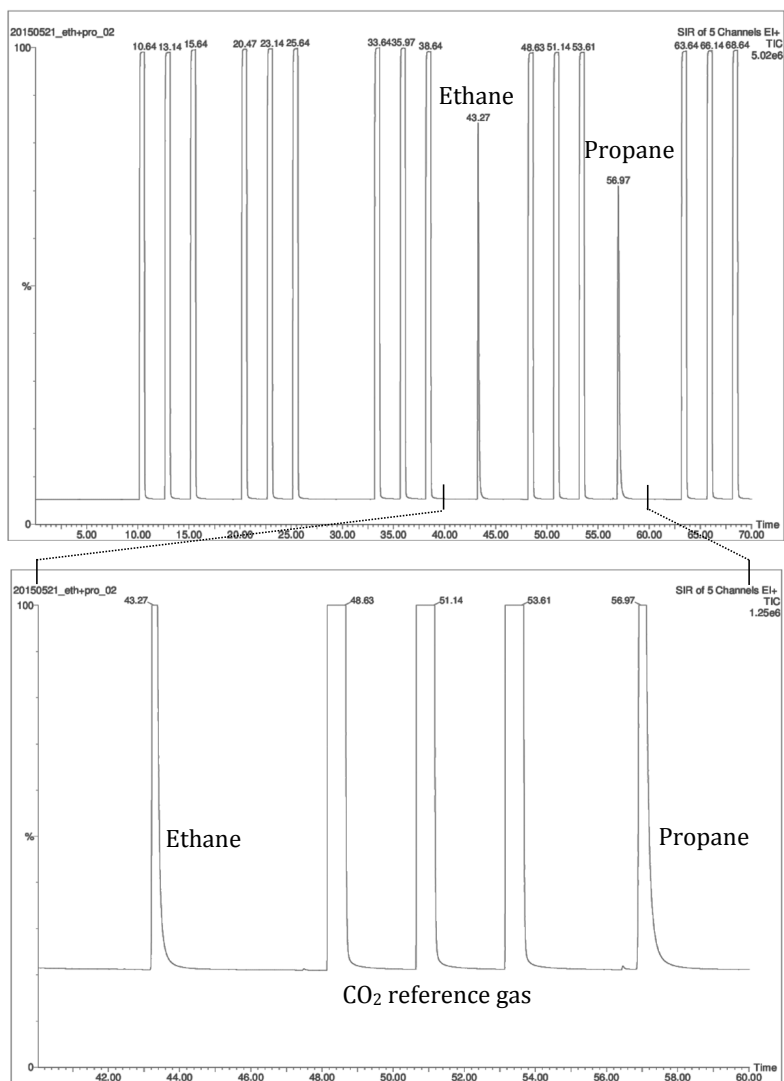
Figure 2.5   IRMS chromatogram of separated ethane and propane displaying *m/z* 44 signal (top panel) and zoomed time window (from 40 to 60 minutes) of ethane and propane elution (bottom panel). This chromatogram was measured during the quality control experiments at 253.2 ± 0.3 K (second measurement).

2.2.1 Quality control experiments

Prior to each KIE experiment at a constant temperature, stability measurements of concentration and $\delta^{13}C$ were carried out to characterize the performances of all elements along the instrumental setup, from the temperature controlled reaction chamber to the TD-GC-C-IRMS. To carry out these tests, the experimental procedure described above was employed. The only difference to the KIE experiments was that there was no oxidation reaction taking place in the reaction chamber. Ethane and propane were injected in the bag. Instead of gaseous H_2O_2, the same volume of pure N_2 was added to the VOC mixture. The UV lamps were off. All stability experiments were conducted for 17 hours, reproducing twelve GC-IRMS measurements of 90 min each. The first measurement started 30 minutes after preparation of the temperature controlled reaction chamber. The averaged concentration changes, represented as ratios ($[C]_t/[C]_0$) × 100 %, and $\delta^{13}C$ of ethane and propane during the stability experiments carried out at 303.0 ± 0.1, 288.0 ± 0.2, 272.7 ± 0.3, 262.9 ± 0.3, 253.2 ± 0.3, and 242.7 ± 0.3 K are illustrated in Figure 2.6. The corresponding average and errors are reported in Table 2.3. Neither a systematic change of ethane or propane concentrations, nor a change in relative concentration of ethane compared to propane was observed. This implies that the reaction chamber did not have significant leak. Moreover, there were no other loss processes of the compounds of interest along the transfer lines or in the TD-GC-C-IRMS system. The outliner in the propane concentration observed during the stability experiment at 288.0 ± 0.2 K might be caused by a flaw in the sampling followed by a deficient absorption on Carbosieve at the initial measurement, leading to a much too high mean value for the whole data set. The profiles of concentration changes and $\delta^{13}C$ of ethane and propane along the time of measurement during the stability experiments are displayed in Figure A.6 (Section A.3 in the Appendix).
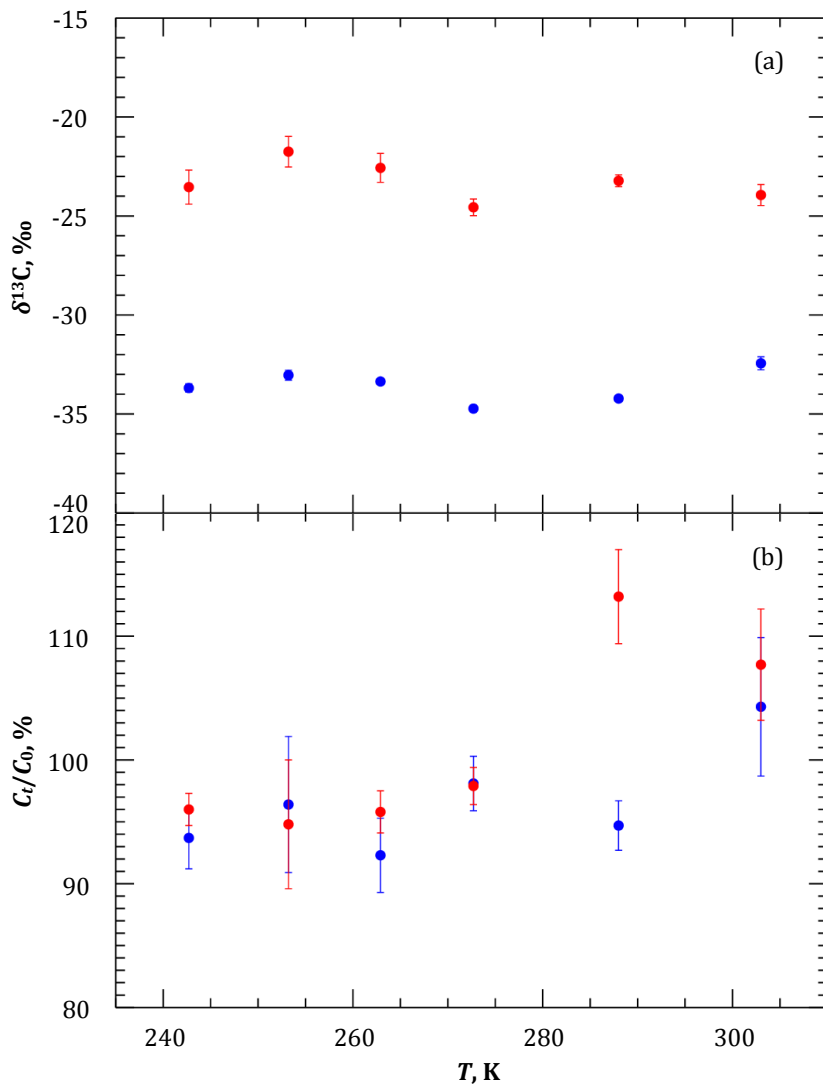
Figure 2.6   Mean values and errors of $\delta^{13}C$ (a) and concentration change expressed by the ratio of the concentration measured during the stability experiment to the initial concentration (b) of ethane (blue) and propane (red) during stability experiments at 303.0 ± 0.1, 288.0 ± 0.2, 272.7 ± 0.3, 262.9 ± 0.3, 253.2 ± 0.3, and 242.7 ± 0.3 K.

Table 2.3 Mean values and errors of $\delta^{13}C$ measured by EA-IRMS and TD-GC-C-IRMS, as well as of the concentration change, expressed by the ratio of the concentration measured during the stability experiment to the initial concentration (for details see text).

T, K	$\delta^{13}C$, ‰		$[C]_t/[C]_0$, %	
	Ethane	**Propane**	**Ethane**	**Propane**
303.0 ± 0.1	-32.44 ± 0.33	-23.94 ± 0.53	104.3 ± 5.6	107.7 ± 4.5
288.0 ± 0.2	-34.22 ± 0.09	-23.22 ± 0.30	94.7 ± 2.0	113.2 ± 3.8
272.7 ± 0.3	-34.73 ± 0.17	-24.56 ± 0.42	98.1 ± 2.2	97.9 ± 1.5
262.9 ± 0.3	-33.36 ± 0.12	-22.57 ± 0.73	92.3 ± 3.0	95.8 ± 1.7
253.2 ± 0.3	-33.04 ± 0.25	-21.75 ± 0.77	96.4 ± 5.5	94.8 ± 5.2
242.7 ± 0.3	-33.69 ± 0.21	-23.65 ± 0.86	93.7 ± 2.5	96.0 ± 1.3
Average	-33.58 ± 0.21	-23.26 ± 0.63		
EA-IRMS	-30.26 ± 0.19	-23.36 ± 0.10		

The compound specific ethane and propane $\delta^{13}C$ values were compared to the bulk measurements, carried out by using Elemental Analysis – Isotope Ratio Mass Spectrometry (EA-IRMS). For EA-IRMS measurements, ethane and propane, 1 mL each, were completely combusted at 1293 K. The stable carbon isotopic ratios of the resulting CO_2 were determined by IRMS. The values are presented in Table 2.3. The good agreement between the compound specific and the bulk measurements for propane shows that no significant isotopic fractionation took place during the multiple steps of the TD-GC-C-IRMS method, i.e. preparation, separation and detection. For ethane, a significant difference of approximately 3 ‰ was observed between the EA- and TD-GC-C-IRMS measurements, although both methods displayed good reproducibility, with uncertainties well below the observed difference. This might be related to the challenges of injecting the light hydrocarbon ethane by syringe in the EA. Nevertheless, the stability of $\delta^{13}C$ values proves a very high accuracy

of the TD-GC-C-IRMS measurements. Higher standard deviation of the concentration measurements, compared to the isotopic ones might be due to small variations in the absorbing efficiency of Carbosieve inside the CIS. Experiments with different ethane amounts introduced in the reaction chamber of 150 ppb and 1000 ppb showed comparable $\delta^{13}C$ value of -32.60 ± 0.37 (from 12 measurements for each experiment), indicating that different absorbed amounts did not introduce any significant isotopic fractionation. Overall, the performances of the sampling and TD-GC-C-IRMS systems were highly reproducible.

2.2.2 KIE experiments

For each temperature, three experiments were conducted. At 242.7 ± 0.3 K four experiments were carried out. The experiment overview including amount of ethane and propane introduced into reaction chamber, amount of H_2O_2 injected into canister, number of UV lamps on, duration of experiment and number of data points obtained from GC-IRMS for each experiment are listed in Table 2.4.

Table 2.4   Experimental conditions for all performed experiments

T, K	Exp. No.	Amounts of precursors			No. of UV lamps on	Exp. duration, hours	GC-IRMS data points
		C_2H_6, µL	C_3H_8, µL	H_2O_2, mL			
303.0 ± 0.1	1	150	150	5	2	9.2	6
	2	150	150	5	2	10.8	7
	3	150	150	5	2	7.7	5
288.0 ± 0.2	4	300	150	5	4	6.2	4
	5	300	150	5	4	7.7	5
	6	300	150	5	2	15.4	10

Table 2.4   Continued.

T, K	Exp. No.	Amounts of precursors			No. of UV lamps on	Exp. duration, hours	GC-IRMS data points
		C_2H_6, µL	C_3H_8, µL	H_2O_2, mL			
272.7 ± 0.3	7	150	150	5	2	10.8	7
	8	150	150	5	2	23.0	15
	9	150	150	10	2	23.0	15
262.9 ± 0.3	10	300	150	5	4	15.4	10
	11	300	150	10	4	10.8	6
	12	300	150	10	4	13.8	9
253.2 ± 0.3	13	300	150	10	4	21.6	13
	14	300	150	20	4	13.8	9
	15	300	150	20	4	16.9	11
242.7 ± 0.3	16	150	150	10	2	9.2	4
	17	300	150	20	4	15.4	10
	18	300	150	20	4	12.3	8
	19	300	150	20	4	10.8	7

2.2.3 $\delta^{13}C$ calculation

All $\delta^{13}C$ values in this work are determined in the laboratory by using a working standard, yet finally derived relatively to the international VPDB carbon reference. Higher $\delta^{13}C$ values results from higher $(^{13}C/^{12}C)_{sample}$. Higher $\delta^{13}C$ values describe 'heavier' compounds and show enrichment in ^{13}C relatively to the ^{12}C. Since the reported values for

the samples used in this work are in the negative range, this means that there is a depletion of ^{13}C in the samples relatively to the reference VPDB.

In the isotope ratio mass spectrometry (IRMS), the ion currents at mass-to-charge ratios m/z 44, 45 and 46 of CO_2 are determined. The peak area ratios ^{45}R and ^{46}R are defined as following:

$$^{45}R = \frac{[^{13}C^{16}O^{16}O] + [^{12}C^{16}O^{17}O]}{[^{12}C^{16}O^{16}O]} = \frac{\text{peak area of } m/z \text{ 45}}{\text{peak area of } m/z \text{ 44}} \qquad (2.1)$$

$$^{46}R = \frac{[^{12}C^{16}O^{18}O] + [^{13}C^{16}O^{17}O] + [^{12}C^{17}O^{17}O]}{[^{12}C^{16}O^{16}O]}$$

$$= \frac{\text{peak area of } m/z \text{ 46}}{\text{peak area of } m/z \text{ 44}} \qquad (2.2)$$

where $[^{i}C^{ii}O^{iii}O]$ are the number concentrations of the isotopologues containing the respective stable carbon and oxygen isotopes. Since the ratios ^{45}R and ^{46}R include the contribution from both ^{13}C and [17]O isotopologues, a correction for [17]O must be carried out to accurately determine the $\delta^{13}C$ of a sample. According to Brand et al. [44], the corrected $\delta^{13}C$ value of CO_2 evolved from carbonate isotopic reference material measurements can be calculated as following:

$$\delta^{13}C = {}^{45}\delta_{VPDB\text{-}CO_2} + 2\frac{^{17}R_{VPDB\text{-}CO_2}}{^{13}R_{VPDB}}\left({}^{45}\delta_{VPDB\text{-}CO_2} - \lambda {}^{46}\delta_{VPDB\text{-}CO_2}\right) \qquad (2.3)$$

where $^{13}R = (^{13}C/^{12}C)$ and $^{17}R = (^{17}O/^{18}O)$ in CO_2; the IUPAC recommended value for $^{17}R_{VPDB\text{-}CO_2}/^{13}R_{VPDB}$ is 0.03518(8) [45]; λ is an isotopic fractionation factor relating the abundances ^{17}O of and ^{18}O and showing a value of 0.528 [44]; the $^{45}\delta_{VPDB-CO_2}$ and $^{46}\delta_{VPDB-CO_2}$ values are defined as:

$$^{45}\delta_{VPDB\text{-}CO_2} = (\frac{^{45}R_{CO_2}}{^{45}R_{VPDB}} - 1)1000‰ \text{ and} \tag{2.4}$$

$$^{46}\delta_{VPDB\text{-}CO_2} = (\frac{^{46}R_{CO_2}}{^{46}R_{VPDB}} - 1)1000‰. \tag{2.5}$$

where the ratios ^{45}R and ^{46}R are described by the Equations 2.1 and 2.2.

Combining the described correction approach with the ratios ^{45}R and ^{46}R determined by IRMS, the corrected $\delta^{13}C$ values of ethane and propane are calculated as:

$$\delta^{13}C = {}^{45}\delta_{ref\text{-}sample} + 0.0704({}^{45}\delta_{ref\text{-}sample} - 0.528{}^{46}\delta_{ref\text{-}sample}) + {}^{13}\delta_{VPDB\text{-}ref} \tag{2.6}$$

where $^{13}\delta_{VPDB\text{-}ref}$ is the $\delta^{13}C$ value of CO_2 working standard gas (WS) calibrated against the international standard VPDB; during all KIE experiments, a WS with $^{13}\delta_{VPDB\text{-}ref} = -35.80$ ‰ was used; the delta values $^{45}\delta_{ref\text{-}sample}$ and $^{46}\delta_{ref\text{-}sample}$ are defined similarly to Equations 2.4 and 2.5 and experimentally derived from IRMS measurements:

$$^{45}\delta_{ref\text{-}sample} = (\frac{^{45}R_{sample}}{^{45}R_{ref}} - 1)1000‰ \text{ and} \tag{2.7}$$

$$^{46}\delta_{ref\text{-}sample} = (\frac{^{46}R_{sample}}{^{46}R_{ref}} - 1)1000‰. \tag{2.8}$$

Equations 2.6-2.8 as well as those describing the statistical error propagation (see Appendix, Section A.2.4-A.2.5) were implemented in an IDL program to automatize the $\delta^{13}C$ and KIE value calculations, as well as to predict their uncertainties. As input, the raw ratios $^{45}R_{sample}$, $^{46}R_{sample}$, $^{45}R_{ref}$ and $^{46}R_{ref}$ registered by the IRMS software MassLynx (see Section 2.1.2) were used.

2.3 Experimental results and discussion

2.3.1 *Experimental rate coefficient determination for the OH oxidation of ethane by employing the relative rate approach*

The rate coefficient, $k(T)$, of the reaction ethane + OH, carried out at different temperatures, was experimentally evaluated by the relative rate method, using propane + OH as reference reaction (Section 1.4).

For T = 303.0 ± 0.1 K, the experimentally observed ethane concentrations expressed as $\ln([ethane]_0/[ethane]_t)$ were plotted against the propane measured concentrations, expressed as $\ln([propane]_0/[propane]_t)$ (Figure 2.7). As described in Section 1.4, a weighted least squares line was fitted to the experimental data. The slope of this line, found to be 0.235 ± 0.016, describes the ratio $k_{ethane}/k_{propane}$ (see Equation 1.12). By employing the $k_{propane}$ value of 11.02 ± 0.43 × 10^{-13} cm^3 molecule^{-1} s^{-1} corresponding to T = 303 K (from Equation 1.9), a k_{ethane} of 2.59 ± 0.73 × 10^{-13} cm^3 molecule^{-1} s^{-1} at 303.0 ± 0.1 K was experimentally derived. Similarly, the reaction rate coefficients were determined at 303.0 ± 0.1, 288.0 ± 0.2, 272.7 ± 0.3, 262.9 ± 0.3, 253.2 ± 0.3, and 242.7 ± 0.3 K (Section A.4 in the Appendix, Figures A.7-A.25).
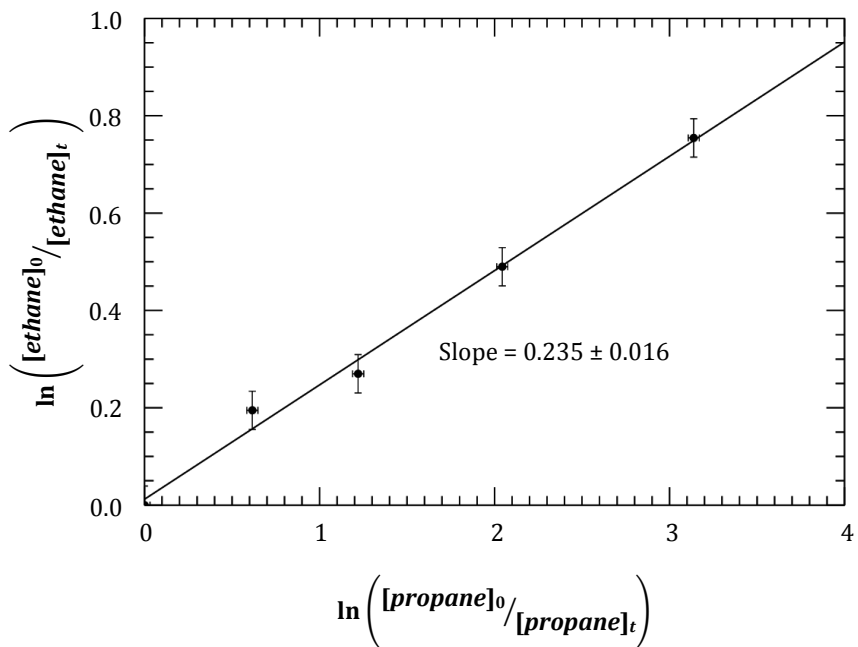
Figure 2.7   Natural logarithms of the ethane and propane concentrations relative to initial concentration (black full circles) during the oxidation reaction by OH at 303.0 ± 0.1 K (Exp. No. 2, Table 2.4), as well as the weighted linear least squares fit to the experimental data (black line).
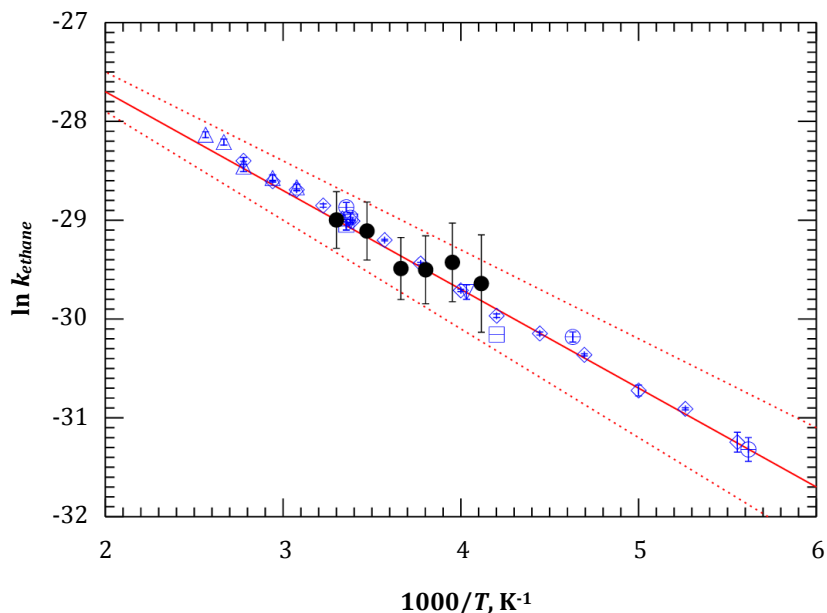
Figure 2.8 Experimentally determined rate coefficients (k_{ethane}, cm^3 molecule^{-1} s^{-1}) for the ethane oxidation by OH (black full circles) at 303.0 ± 0.1, 288.0 ± 0.2, 272.7 ± 0.3, 262.9 ± 0.3, 253.2 ± 0.3, and 242.7 ± 0.3 K. Available data from literature are also shown in blue color: Clarke et al. [46] (diamond), Talukdar et al. [47] (square), Margitan and Watson [48] (square with dash), Zabarnick et al. [49] (circle), Sharkey and Smith [50] (circle with dash), Donahue et al. [51] (triangle), and Stachnik et al. [52] (upside-down triangle). The temperature dependence of the k_{ethane} recommended by the IUPAC Subcommittee on Gas Kinetic Data Evaluation for Atmospheric Chemistry [25] and the uncertainty ranges are depicted by red full and dot lines, respectively.

A summary of the experimentally determined rate coefficients k_{ethane} at different temperatures is presented in Figure 2.8 together with values reported by Clarke et al. [46] (diamond), Talukdar et al. [47], Margitan and Watson [48], Zabarnick et al. [49], Sharkey and Smith [50], Donahue et al. [51], Stachnik et al. [52], as well as the values recommended by the IUPAC Subcommittee on Gas Kinetic Data Evaluation for Atmospheric Chemistry [11]. The latter are derived from Equation 1.8 by using T = 303, 288, 273, 263, 253 and 243 K. For each investigated temperature, the average of the experimentally measured k_{ethane} together with IUPAC recommended values are additionally listed in Table 2.5. The uncertainties propagation calculation is explained in Section A.2.2 in the Appendix.

Table 2.5   Summary of the rate coefficients (k_{ethane}, cm^3 molecule^{-1} s^{-1}), determined by using the relative rate method (for details see text), as well as the recommended IUPAC values, calculated from Equation 1.8 by using T = 303, 288, 273, 263, 253 and 243 K.

T, K	k_{ethane}, 10^{-13} cm^3 molecule^{-1} s^{-1}	
	This work	IUPAC [25]
303.0 ± 0.1	2.55 ± 0.73	2.54 ± 0.99
288.0 ± 0.2	2.28 ± 0.67	2.14 ± 0.89
272.7 ± 0.3	1.56 ± 0.49	1.77 ± 0.78
262.9 ± 0.3	1.54 ± 0.53	1.54 ± 0.71
253.2 ± 0.3	1.66 ± 0.66	1.33 ± 0.64
242.7 ± 0.3	1.34 ± 0.66	1.13 ± 0.57

Figure 2.8 and Table 2.5 imply that the rate coefficients of ethane + OH experimentally determined in this work agree well with the IUPAC recommendations within the error ranges.

2.3.2 Kinetic isotope effect results

For each individual oxidation experiment carried out at a constant temperature, the ethane and propane $\delta^{13}C$ values were found to increase during the oxidation reaction by OH. The change became most pronounced after 80 % conversion of ethane and propane (Figure 2.9). The enrichment of ^{13}C in the reactant during the reaction is expected, since the heavier isotopes accumulate in the precursor due to the kinetic isotope effect [6, 33, 34] (Section 1.5).
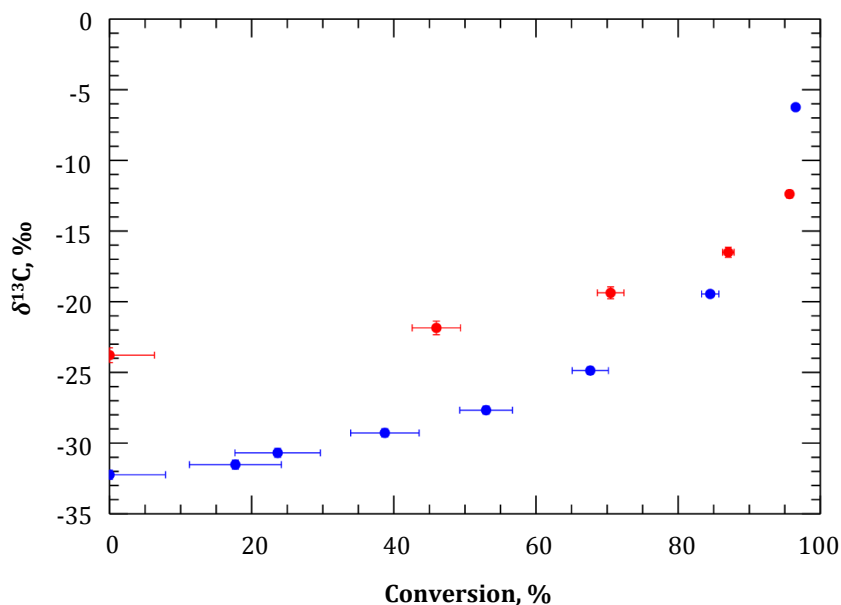
Figure 2.9 $\delta^{13}C$ values observed during the ethane (blue circles) and propane (red circles) oxidation reaction by OH, carried out at 303.0 ± 0.1 K (Exp. No. 2, Table 2.4).

KIE was determined from the temporal evolution of concentrations and δ^{13}C values during the reaction. As shown in Section 1.5 the experimentally obtained $\ln([^{12}C]_t/[^{12}C]_0)$ values were plotted against the $\ln([\delta^{13}C_t+1000]/[\delta^{13}C_0+1000])$ values. A line was fitted to the data by carrying out a weighted least squares linear fit analysis. The slope of this line is an expression of the *KIE*, i.e. *KIE*/(1-*KIE*). Finally, the KIE and ε values for the oxidation of ethane and propane by OH were determined from Equations 1.23 and 1.24 respectively.
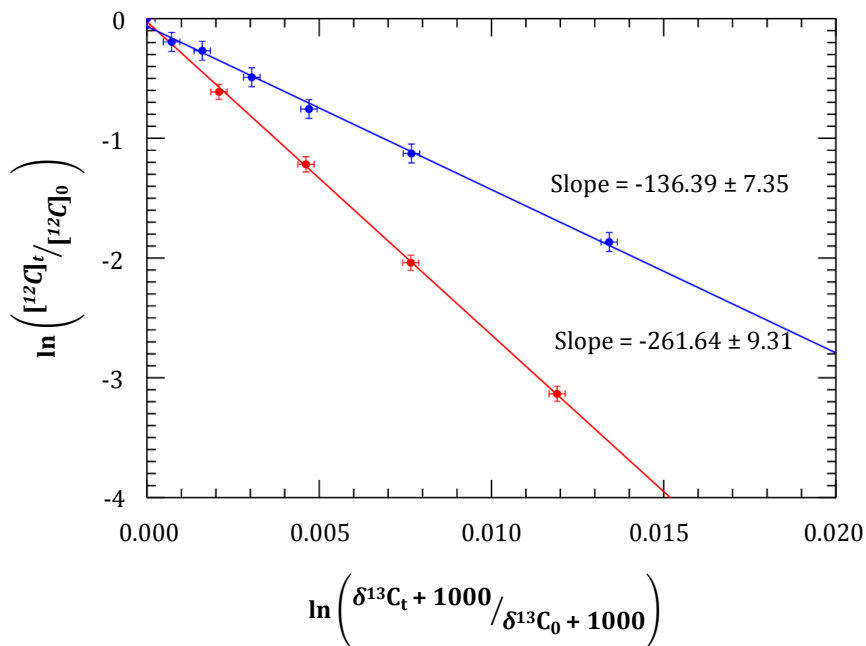
Figure 2.10 The temporal evolution of concentration and isotopic composition of ethane (blue full circles) and propane (red full circles) at 303.0 ± 0.1 K (Exp. No. 2, Table 2.4). The slopes of the fitted lines (blue for ethane, red for propane) to the experimental data are -136.39 ± 7.35 and -261.64 ± 9.31, respectively, translating in $^{OH}\varepsilon$ values of 7.39 ± 0.40 ‰ and 3.84 ± 0.14 ‰ (for detail, see text).

Figure 2.10 shows an example for the experimental KIE determination. The fitted lines to the experimental data have slopes of -136.39 ± 7.35 for ethane and -261.64 ± 9.31 for propane. Thus, the *KIE* of ethane and propane oxidation by OH at 303.0 ± 0.1 K, expressed in $^{OH}\varepsilon$ values, were found to be 7.39 ± 0.40 and 3.84 ± 0.14 ‰, respectively. For each temperature, the same procedure was employed to determine the KIE values for the ethane and propane OH oxidation (see Section A.6 in the Appendix, Figures A.26-A.44). The experimental KIE values from this work, as well as previously reported in the literature [4, 16] are summarized in Table 2.6. An overview of experimental ethane and propane OH oxidation KIE values, showing their temperature dependence, is illustrated in Figure 2.11.

Table 2.6   Summary of experimentally obtained KIE values for oxidation reaction of ethane and propane by OH together with available published data [4, 16].

T , K	$^{OH}\varepsilon$, ‰	
	Ethane	**Propane**
This work		
303.0 ± 0.1	7.16 ± 0.54	3.65 ± 0.36
288.0 ± 0.2	7.45 ± 0.48	3.60 ± 0.31
272.7 ± 0.3	7.36 ± 0.28	3.66 ± 0.15
262.9 ± 0.3	7.61 ± 0.28	3.61 ± 0.34
253.2 ± 0.3	8.89 ± 0.90	4.87 ± 0.56
242.7 ± 0.3	9.42 ± 2.19	4.31 ± 0.70
Literature		
296 ± 4 [16]	8.57 ± 1.95	5.46 ± 0.35
305 ± 3 [4]	-	3.44 ± 0.26
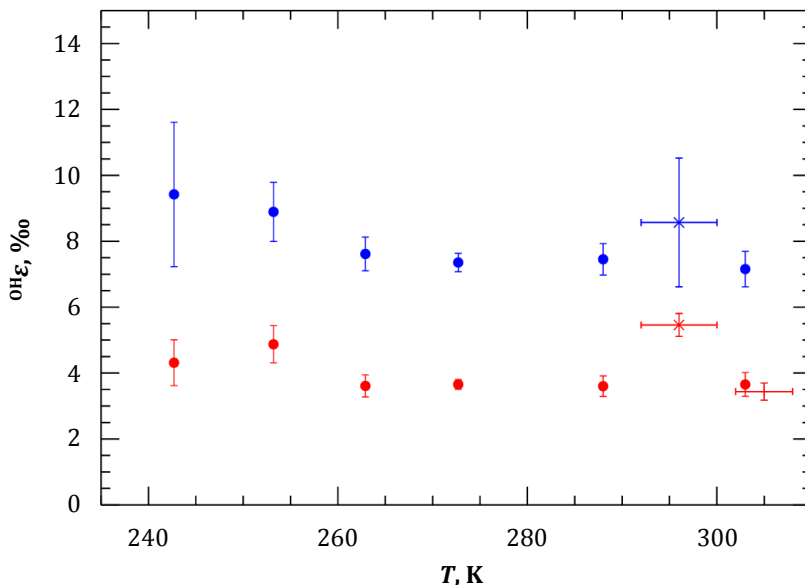
Figure 2.11 Overview of experimental KIE values for the oxidation reaction of ethane (blue color) and propane (red color) by OH from this work (full circles), as well as literature values at room temperature (cross by Anderson et al. [16]) and 10-15 K above it (plus by Rudolph et al. [4]) .

KIE values of ethane at 303.0 ± 0.1 and 288.0 ± 0.2 K were found to be 7.03 ± 0.59 and 7.45 ± 0.48 ‰, respectively, showing good agreement with the value reported by Anderson et al. [16], i.e. 8.57 ± 1.95 ‰ at 296 ± 4 K. It has to be mentioned that within this work, the KIE of ethane measured around room temperature shows a remarkable refinement of the measurement precision, compared to the previous report. KIE of propane at 303.0 ± 0.1 K was determined to be 3.61 ± 0.37 ‰. This $^{OH}\varepsilon$ agrees also very well with the value 3.44 ± 0.26 ‰, reported by Rudolph et al. [4] and is very different from the value by 5.46 ± 0.35 ‰ reported by Anderson et al. [16]. Both KIE values of ethane and propane obtained in this work are also in fairly good agreement with the values predicted using the inverse dependence on carbon number [4] (for detail, see Section 1.6), being 8.3 and 5.5 ‰, respectively.

All derived KIE uncertainties were very small, showing values between 8.39 % and 19.76 % of the average. This proves a significant improvement in the precision of KIE experiments for long-lived hydrocarbons. The ethane OH oxidation KIE measured at 242.7 ± 0.3 K is accompanied yet by a high standard error to the mean, i.e. 9.92 ± 1.96 ‰. Two aspects might be relevant here, both concerning the significantly longer reaction duration compared to other experiments at higher temperatures. Since the rate coefficient for the reaction ethane + OH at 243 K is 2.3 times smaller than at 303 K, the same degree of reactant conversion was reached after longer experiment duration. Moreover, as mentioned in Section 2.2, OH radicals were produced by UV photolysis of gaseous H_2O_2 (Reaction R2.1). At low temperatures, H_2O_2 (melting point, T_M =272.72 K and boiling point, T_B = 425.15 K) has a very low vapor pressure, tending to immediately condense and freeze. Thus, a significant fraction of H_2O_2 will be removed from the OH production reaction, dramatically reducing the ethane conversion at 243 K.

Overall, a slight tendency of KIE increasing at lower temperatures can be observed. In this work, the KIE for the OH oxidation of ethane changes from room temperature down to 243 K on average by approximately 0.4 ± 0.1 ‰ per 10 K. This change is more pronounced at temperatures lower than 263 K.

This might be of high interest for tropospheric research, since, as mentioned in Section 1, temperatures down to 193 K can be found, especially in the upper troposphere. Despite of the main sources of ethane are on the ground, ethane can be found in high concentration in the upper troposphere due to its long life time.

Large changes in KIE at low temperatures may translate in high deviations for global modeling results of ethane isotopic distribution between the case when KIE temperature dependence is considered and when it is neglected. This will be further discussed in Section 4. On the other side, it was shown that carrying out KIE studies is experimentally not possible at temperatures lower than 243 K with the instrumentation used in this work, due to the too long measurement duration which translates in high uncertainties of the KIE determination. Therefore, theoretical studies of KIE temperature dependence employing

quantum mechanical calculations (Section 3) were performed to provide insight in the KIE temperature dependence at temperatures lower than 243 K.

The temperature dependence of propane KIE is inconclusive. Here, it has to be mentioned that all experiments were designed to obtain an optimal reaction progress for ethane, covering its whole dynamical processing range. In most experiments, propane was completely consumed at times when ethane conversion of 50 % to 70 % was reached. Therefore, few data points for the propane concentration and δ^{13}C were measured during each experiment, most of them belonging to the high margin of the conversion range. Considering the δ^{13}C dependence on the extent of the reaction (e.g. Figure 2.9), high imprecision can be anticipated in the propane oxidation KIE calculation, when few points are measured solely in the last segment of the reaction dynamical range.

This study showed that the extent of chemical processing during the OH oxidation was much lower for ethane than for propane, due to reaction rate coefficients differing by a factor of six. This brings challenges in concurrently obtaining accurate KIE values for both compounds. Nevertheless, it was shown that propane was a good reference compound to be used in relative rate method to experimentally derive kinetic information for the reaction ethane + OH. To precisely determine propane oxidation KIE and its temperature dependence, further experiments are necessary, with configurations specially designed for propane measurements.

3   Theoretical KIE determination for C_2H_6 + OH

The KIE temperature dependence of the ethane oxidation by hydroxyl radicals was studied theoretically, including a temperature range where experiments are difficult to be carried out. Quantum mechanical calculations, providing molecular characteristics on the potential energy surface (PES), were used in a transition state theory (TST) framework to determine reaction rate coefficients. The applied theories (Section 3.1) and the methodology to deduce KIE from the theoretically obtained ^{12}k and ^{13}k (Section 3.2) followed by the results and discussion of theoretically determined KIE are described in this chapter.

3.1   Related Theories

In recent years, theoretical techniques based on quantum mechanics have been applied to an increasing degree to study the kinetics and thermodynamics of chemical reactions. Hydrogen abstraction reactions of saturated hydrocarbons by OH radicals are very important in combustion and atmospheric chemistry, therefore, estimation of rate coefficients over wide temperature ranges is necessary [54-65], often outside the experimentally accessible range. In Section 2.3.2, it was stated that experimental challenges to produce OH radicals at temperatures lower than 243 K made exploring the KIE temperature dependence in the whole range of tropospheric temperatures impossible. Therefore, supplemental theoretical techniques were applied, where electronic structure calculations of energies, geometries and vibrational frequencies of the reactants and transition state for the C_2H_6 + OH reaction are combined with the TST to determine rate coefficients.

The stable carbon KIE temperature dependence was investigated by calculating the rate coefficients k_{12} and k_{13} for the C_2H_6 + OH reaction, when different ethane isotopologues

are involved (see detail in Section 1.5). Conventionally, the following stages can be distinguished when determining the thermal rate coefficients:

i) The characterization of the molecular properties on the reaction potential energy surface (PES) employing quantum chemical mechanics. Thus, fundamental properties such as geometries, relative energies, and molecular degrees of freedom were characterized;

ii) The quantification of the state density of reactants and transition states (TS) from molecular properties as determined by the molecular degrees of freedom and their interactions;

iii) The calculation of temperature dependent rate coefficients by employing state density and energetic descriptions of the reaction. Additionally, the tunneling effect was considered.

The theories employed in this work can be divided into two parts. Firstly, quantum mechanical calculations provided molecular properties on the PES for use as input data in the thermal rate coefficients estimation. All theories related to the first part are described in Section 3.1.1. Secondly, the chemical kinetics was investigated using the information obtained from quantum mechanical calculations. This part is presented in Section 3.1.2.

3.1.1 Electronic Structure Calculations

The basis for quantum chemical calculations relies on a differential equation known as the time-independent Schrödinger equation (Equation 3.1). The time-independent Schrödinger equation predicts the stationary state of a molecular system. According to this equation, the Hamiltonian operator ($\hat{H}$) applied upon a certain wavefunction (Ψ) derives the total energy (E) from the stationary state Ψ.

$$\hat{H}\,\Psi = E\,\Psi \tag{3.1}$$

The wavefunction describes the nature of the molecular system. Once the wavefunction is known, any observable properties may be predicted by applying the appropriate mathematical operation to the wavefunction. To solve the Schrödinger equation, and hence, to obtain the form of the wavefunction and the quantized energies for the molecular system of interest, the Hamiltonian operator must first be specified. This consists of one kinetic energy ($\hat{T}$) and one potential energy ($\hat{V}$) operator [66]:

$$\hat{H} = \hat{T} + \hat{V} \tag{3.2}$$

The kinetic energy operator ($\hat{T}$) is expressed as the sum over all individual particles (denoted i); the change in position of each particle with the mass m , here described in Cartesian coordinates x, y, and z [66]:

$$\hat{T} = -\frac{h^2}{8\pi^2}\sum_i \frac{1}{m_i}\left(\frac{\partial^2}{\partial x_i^2}+\frac{\partial^2}{\partial y_i^2}+\frac{\partial^2}{\partial z_i^2}\right) = -\frac{h^2}{8\pi^2}\sum_i \frac{\nabla_i^2}{m_i} \tag{3.3}$$

where h is Planck's constant. In a molecular system, where the wavefunction depends on the position of electrons and nuclei, the Hamiltonian kinetic energy term is divided into two terms describing the motion of electrons, and of nuclei.

The potential energy operator ($\hat{V}$) is expressed as the sum of the electrostatic interactions between two particles (denoted i and j) with the charge q [66]:

$$\hat{V} = \frac{1}{4\pi\varepsilon_0}\sum_i \sum_{j>i} \frac{q_i q_j}{r_{ij}} \tag{3.4}$$

where ε_0 represent the permittivity of vacuum, and r_{ij} the distance between the interacting particles. The potential energy term combines the electrostatic interactions between the electrons and nuclei. Attractive interactions exist between the negatively charged electrons and the positively charged nuclei. A repulsive nature exists for electron-electron and nuclei-nuclei interactions.

The Born-Oppenheimer approximation is applied in the calculation of molecular systems since the Schrödinger equation cannot be analytically solved even for very simple molecules. This concept states that the motion of electrons and nuclei are separable. Electrons are much lighter than the nuclei, resulting in 'instantaneous' rearrangement of the electron motion, compared to the much slower changes in the nuclei configuration. Consequently, the nuclei can be considered stationary and the electron calculations in Schrödinger equation become independent of the nuclear motion. Using the Born-Oppenheimer approximation, the nuclear kinetic energy Hamiltonian term can be neglected when obtaining the electronic wavefunctions and energies. When determining the electronic energy, the Born-Oppenheimer approximation does not directly account for variations in the nuclei coordinates. The solution is to solve the Schrödinger equation for the electrons moving in the static electric potential of the fixed nuclei in a specific arrangement. The calculations are repeated with different arrangements. The set of solutions is used to define the PES of a polyatomic species.

After applying the Born-Oppenheimer approximation the Schrödinger equation can be rewritten as a set of coupled per-electron equations, including the kinetic and potential energy terms (see Equations 3.3 and 3.4) [66]:

$$(\hat{T} + \hat{V}) \, \psi_i = E_i \, \psi_i \tag{3.5}$$

$$\left(-\frac{h^2}{8\pi^2} \frac{\nabla_i^2}{m_e} + \frac{1}{4\pi\varepsilon_0} \left(-\sum_{\alpha}^{\text{nuclei}} \frac{Z_\alpha e^2}{r_{\alpha i}} + \sum_{j>i}^{\text{electron}} \frac{e^2}{r_{ji}} + \sum_{\alpha}^{\text{nuclei}} \sum_{\beta>\alpha}^{\text{nuclei}} \frac{Z_\alpha Z_\beta e^2}{r_{\alpha\beta}} \right) \right) \psi_i = E_i \, \psi_i \tag{3.6}$$

where the mass and charge of the electrons are given by m_e and e, respectively. In Equation 3.6, Z represents the atomic number of the nuclei (α, β).

The complexity of the Schrödinger equation requires the use of sophisticated techniques and algorithms to find the numerical solution. These are chosen, depending on the nature of the molecular system of interest, the required accuracy of results, and

available computational resources. The techniques employed in quantum chemical calculations can be categorized into:

i) *ab initio* methods based on the description of molecular wavefunctions;

ii) density functional theory (DFT) methods based on the description of molecular electron density;

iii) semi-empirical methods that include approximation and parameterization from empirical data.

The *ab initio* calculations can give a very high accuracy of the results but require a high computational cost due to complicated calculations of multi-electron correlation. DFT calculations are an alternative method based on parametrized "correlation-exchange functionals" to reduce the computational costs but give less accurate results than the *ab initio* approaches. Semi-empirical calculations can be performed very fast, but their accuracy and the validity of results strongly rely on applying the appropriate method for a specific system.

In this work, in order to balance computational cost and result accuracy, both *ab initio* and DFT methods were used for electronic calculations.

3.1.1.1 Basis sets used in the electronic structure calculations

To solve the Schrödinger equation by quantum chemical programs, the electronic wavefunction (*ab initio*) or the electronic density (DFT) can be defined using molecular orbitals, ϕ_i, which are described by basis sets (pre-defined sets of basis functions, χ_μ). Therefore, each molecular orbital is expressed as a linear combination of basis functions and molecular orbital expansion coefficients, $c_{\mu i}$:

$$\phi_i \ = \ \sum_\mu c_{\mu i} \chi_\mu \ = \ \sum_\mu c_{\mu i} \left(\sum_p d_{\mu p} g_p \right) \tag{3.7}$$

where $d_{\mu p}$ is a constant which depends on the basis set used, and g_p is a Gaussian-type atomic function or a basis function, representing the sum of all one-electron functions, which are known as 'Gaussian primitives':

$$g_p(\alpha, r) = c x^n y^m z^l \mathrm{e}^{-\alpha r^2} \tag{3.8}$$

where r represents the electron spatial position, α is a constant defining the size or radial extend of the function, and c is a normalization constant depending on α and the powers of x, y, and z (m, n, and l, respectively).

The ability of the functions to describe the molecular orbitals depends on a number of basis functions which include their size and shape. The number of basis functions combined in a basis set varies from a few to hundreds per atom. A higher accuracy of any given calculation can be obtained by increasing the flexibility of describing the electron position by changing the size and shape of the molecular orbitals.

Improving the description of the size and shape of the molecular orbitals can be done by improving the basis set, e.g. by introducing split valence orbitals, additional polarization functions, or diffuse functions in the calculations. Split valence basis sets are used to increase the size range of the molecular orbitals used by allowing for a linear combination of different sized orbitals. E.g. In a double-zeta split valence basis set, two differently sized orbitals are used to construct the molecular orbitals. Similarly, three different sized orbitals are used to construct the molecular orbitals in a triple-zeta basis set. Although the split valence basis sets permit the change in the size of the orbital, they do not permit the shape to change. The change of the orbital shape can be achieved by using either polarized or diffuse functions. The polarized functions are used to change the shape of the orbitals used in the construction of the molecular orbitals, by introducing linear combinations of two differently shaped orbitals. By varying the combination of the different shapes, it is possible to create new orbitals with shapes that may be more useful to accurately describe the molecular orbitals. Polarized functions combine valence orbitals (which would be used to describe the ground state) with orbitals that have higher angular

momentum. For instance, inclusion of polarized functions on a carbon atom would allow for a combination of *p*- and *d*-orbitals. Another way to alter the shape of the orbitals is to introduce diffuse functions. Diffuse functions increase the region where electrons might be found. Diffuse functions are commonly used for systems where long-range electron interaction could be important, e.g. H-bonds, or van der Waals complexes.

3.1.1.2 Dunning's correlation-consistent basis sets

Here, Dunning's correlation-consistent basis sets [67-71] are used. This series of basis sets is designed to converge systematically to the complete-basis-set (CBS) limit using empirical extrapolation techniques. They are valence-only basis sets including larger shells of polarization (correlating) functions and can be augmented with diffuse functions for electronic excited-state calculations, electric field property calculations, and long-range interactions (such as the van der Waals force). The extrapolation to the CBS limit using these basis sets is possible for almost any energetic property because of their rigorous construction.

The augmented Dunning's correlation-consistent polarized Valence with Triple-Zeta (aug-cc-pVTZ) basis set was employed in this work. 14 valence polarization functions present for H and 30 for C and O atoms were included in aug-cc-pVTZ.

The 14 functions describing the electronic structure for H atoms include 3 functions for 3 *s*-orbitals (principal quantum number, $n = 1$-3, and angular quantum number, $l = 0$), 6 functions for 2 sets of *p*-orbitals ($n = 2, 3$, and $l = 1$) and 5 functions for one set of *d*-orbitals ($n = 3$, and $l = 2$).

The 30 functions used for C and O atoms include 4 functions for 4 *s*-orbitals ($n = 1$-4, and $l = 0$), 9 functions for 3 sets of *p*-orbitals ($n = 2$-4, and $l = 1$), 10 functions for 2 sets of *d*-orbitals ($n = 3, 4$, and $l = 2$) and 7 functions for one set of *f*-orbitals ($n = 4$, and $l = 3$).

For diffuse functions, aug-cc-pVTZ basis set places one *s*, one *d*, and one *p* diffuse functions on hydrogen atoms as well as one *s*, one *p*, one *d*, and one *f* diffuse functions on the C and O atoms.

3.1.1.3 *Ab initio* theory

As implied by the Latin translation, "from the beginning", *ab initio* calculations are based on fundamental principles and do not rely on known properties of the species being investigated. Such calculations are normally performed at several levels of theory. Initial investigations may be performed with the most basic approach, Hartree-Fock (HF), which provides approximate results for numerous systems. In case more accurate results are required, greater sophistication is needed, In such cases, higher levels of theory, including Møller-Plesset perturbation (MP), coupled-cluster (CC), and quadratic configuration interaction (QCI) are widely used [72-80].

HF theory describes the wavefunction (Ψ) as a linear combination of the molecular orbitals (φ). The combination is expressed in form of the Slater determinant to preserve the anti-symmetric nature of the wavefunction [66]:

$$\Psi = \frac{1}{\sqrt{n!}} \begin{vmatrix} \varphi_1\alpha(1)\varphi_1\beta(1) & \cdots & \varphi_i\alpha(1)\varphi_i\beta(1) \\ \vdots & \ddots & \vdots \\ \varphi_1\alpha(n)\varphi_1\beta(n) & \cdots & \varphi_i\alpha(n)\varphi_i\beta(n) \end{vmatrix} \tag{3.9}$$

The determinant elements here are products of the molecular orbitals with spin functions (α, β), thus producing spin orbitals.

According to the variational principle, a number of trials can be generated, where the wavefunction as well as the energy of the system described by the simulated wavefunction can be obtained. The best description is that which corresponds to the lowest energy, allowing one to improve the result by varying the parameters to obtain the energetic minimum. Combining the Slater determinant with the variational principle, the HF equations are described as following:

$$\hat{f}\,\varphi_i = \varepsilon_i\,\varphi_i \qquad\qquad (3.10)$$

where $\hat{f}$ is the Fock operator, containing the core Hamiltonian and the Coulomb and exchange operators. The Fock operator describes the average effect on an electron by the field created by the other electrons in their orbitals. The term ε_i represents the energy of a particular molecular orbital, φ_i.

The HF equation can be solved by an iterative method that modifies a trial wavefunction to increasingly approach the true wavefunction, and the corresponding energy will likewise approach the true energy of the system. The end-result of this optimization is a self-consistent field (SCF). Although HF theory provides a good first-order approach in obtaining a description of a molecular system, the lack of full (instantaneous rather than averaged) electron correlation in an HF calculation can lead to significant errors in the final results.

To account for the electron correlation, high-level theories are employed. Configuration interaction (CI) is based on expressing the wavefunction with more than one determinant, unlike the HF theory where the wavefunction is expressed as a single Slater determinant. In CI methods, the additional determinants are created by replacing one or more occupied molecular orbitals in the HF determinant with virtual orbitals. The particular extent to which these substitutions are made is indicated in the name of the method employed. For example, a double substitution, two virtual orbital replaces occupied orbitals or two electrons are excited. CISD is a denotation of CI with single and double substitution. In triple substitutions exchanging three orbitals occurs, and so forth. In the full CI (FCI) calculation, all possible substitutions are made, and the wavefunction is expressed as a linear combination of all of the determinants [66]:

$$\Psi = b_{\mathrm{HF}}\Psi_{\mathrm{HF}} + \sum_{s>0} b_s\Psi_s \qquad\qquad (3.11)$$

where s indexes the terms that run over all substitutions and b is the set of coefficients to be solved for, by minimizing the energy of the resultant total wavefunction.

Although a full CI calculation is capable of producing the exact solution of the Schrödinger equation, limited only by the basis set size, the computational requirements are excessive for commonly available computational resources. As such, it is common to truncate the number of substitutions which are made; single (S), double (D), and triple (T) substitutions are usually included in the calculations. Unfortunately, truncated CI methods are not size-consistent, i.e. the energy for a system containing two fragments separated at great distance no longer equals the sum of the energies of the two fragments calculated independently of one another. Size-consistency is especially important in calculations where bond dissociation occurs, such as in abstraction reactions. An alternative approach that is size-consistent is a coupled cluster (CC) calculation. While more accurate, the method by which the determinants are chosen is much more complex, making the computational demands greater than those of CI.

3.1.1.4 Coupled cluster

Coupled cluster method has found wide acceptance because of the accuracy of the results obtained with this method. The CC represents a similar approach to CI, but constructs multi-electron wavefunctions using the exponential cluster operator to account for electron correlation. The CC exact wavefunction $|\Psi\rangle$ is written as an exponential ansatz [81, 82]:

$$|\Psi\rangle = e^{T}|\Phi_0\rangle \tag{3.12}$$

where Φ_0 is the reference wavefunction and T is the cluster operator, that generates a certain excitation. The exponential function can be written as an infinite power series, i.e. $e^{x} = \sum_{n}(x^{n}/n!)$, such that each excitation also generates all higher excitations. A cluster operator for single excitations thus also includes part of the double, triple, and higher excitations The full cluster operator is written as a linear combination of excited determinants when acting on $|\Phi_0\rangle$, written as [81, 82]:

$$T = T_1 + T_2 + T_3 + \ldots + T_n \tag{3.13}$$

where T_1 is the operator of all single excitations, T_2 is the operator of all double excitations and so on.

CCSD(T) is a commonly used methodology which was employed in this work [83, 84]. CCSD(T) is a combination of coupled cluster with a full treatment of single and double excitations ($T_1 + T_2$) and an estimation of the triple excitations using many body perturbation theory. The full description for CCSD(T) is explained by Pople et al. [83] and Purvis et al. [84].

3.1.1.5 Density functional theory

Density functional theory (DFT) is used to obtain many of the same molecular properties that can be obtained through calculations using *ab initio* theory. The main focus of DFT is the electron density; this is in contrast to *ab initio* theory, where the wavefunction is the core of the calculation. DFT relies on the use of parametrized "exchange-correlation functionals" which approximate the electron interactions. This parametrization is typically derived from benchmark calculations, which introduces an empirical aspect in DFT. Calculations performed with DFT are much less demanding than a corresponding *ab initio* calculation with a comparable degree of electron correlation. Hence, they have become widely used in recent years. DFT is particularly useful in the prediction of geometries and vibrational frequencies of molecules.

DFT methods were originally derived from the Thomas–Fermi–Dirac model that describes electronic structure of many-body systems by electronic density functionals. The Hohenberg-Kohn theorem modernized the DFT methods. It states the existence of a unique functional capable of providing the exact ground state energy and electron density within a molecule. Kohn and Sham approximated the functionals employed by DFT by separation the electronic energy into several terms. The energy of the molecule can be represented as a function of the electron density [66, 85]:

$$E[\rho] = E^T[\rho] + E^V[\rho] + E^J[\rho] + E^{XC}[\rho] \qquad (3.14)$$

where E^T corresponds to kinetic energy terms, E^V is the term including potential energy of nuclear-electron attraction and nuclei repulsion, E^J describes the repulsion between electrons (Coulomb self-interaction of electron density), E^{XC} is the exchange-correlation term including the remaining part of the electron-electron interactions, such as the spin. In this expression, all of the terms are functions of the electron density (ρ) that can be represented as a function of the position of the electron, $\rho(r)$. The energy therefore depends on a function of the position, or rather the energy is a functional of the electron position; hence they are the origin of the term density functional.

In a DFT calculation, the electron density is initially approximated as a superposition of the electron densities of the atoms in the molecule. From the approximated electron density the dependence of the exchange-correlation energy on electron density is calculated. A first-order approximation to determine this dependence is based on the local density approximation, Equation 3.15, where the term ε^{XC} refers to the exchange-correlation energy per electron. From the dependence, the exchange correlation potential, V^{XC}, can then be calculated using Equation 3.16 [66].

$$E^{XC}[\rho] = \int \rho(r)\varepsilon^{XC}[\rho[\rho]]\mathrm{d}r \tag{3.15}$$

$$V^{XC}[\rho] = \frac{\partial E^{XC}[\rho]}{\partial \rho} \tag{3.16}$$

$E^{XC}(\rho)$ is a separable term comprising of the exchange $E^X(\rho)$ and correlation $E^C(\rho)$ parts corresponding to same-spin and mixed-spin, respectively [66]:

$$E^{XC}(\rho) = E^X(\rho) + E^C(\rho). \tag{3.17}$$

Different DFT methods have other descriptions and parameterization for the exchange and correlation terms, and can incorporate e.g. exact exchange, density gradients, the second derivative of the density (Laplacian), and other properties. The E^{XC} can be parameterized incorporating with nonlocal Hartree–Fock exchange energy (E_{HF}^X) yielding hybrid exchange-correlation energy as written [86]:

$$E_{hybrid}^{XC} = cE_{HF}^X + (1-c)E_{DFT}^X + E_{DFT}^C \qquad (3.18)$$

where c is the optimized percentage of HF exchange in the hybrid functional, E_{DFT}^X is the DFT exchange energy and E_{DFT}^C is the DFT correlation energy.

The exchange-correlation potential and approximate electron density can then be used to obtain a description of the molecular orbitals and energy through the Kohn-Sham equation, Equation 3.19 [87]. The Kohn-Sham equation has the same form as that of the Schrödinger equation, where the Hamiltonian has been replaced by the energy density functional. Conversely, the molecular orbitals can also be converted to the electron density, Equation 3.20 [66].

$$\left(-\frac{h^2}{8\pi^2}\frac{\vec{\nabla}_i^2}{m_e} + \frac{1}{4\pi\varepsilon_0}\left(-\sum_{\alpha}^{nuclei}\frac{Z_\alpha e^2}{\Delta r_{\alpha i}} + \sum_{j>i}^{electron}\frac{\rho(r_j)e^2}{\Delta r_{ji}} \right) + V^{XC}(r_i) \right)\psi_i = E_i\,\psi_i \qquad (3.19)$$

$$\rho(r) = \sum_i |\psi_i(r)|^2 \qquad (3.20)$$

There are a number of density functionals available for use in computational calculations. The differences in the functionals relate to the approximation used to examine the dependence of exchange-correlation energy with electron density.

Improvements of the approximation and parameterization have led to the applicability to predict properties such as molecular geometry, vibrational frequencies, and energies. The ability to accurately predict the reaction's properties as well as energies is essential to the study of reactions with transition state theory. The DFT methods used in this work are the hybrid meta exchange-correlation "Minnesota functionals" (M06-2X) [86, 88] and hybrid Becke-style "Half and Half" functional with the Lee, Yang, and Parr correlation functional (BHandHLYP).

3.1.1.6 Minnesota functionals

Minnesota functionals [86, 88] were developed by the group of Prof. Donald Truhlar at the University of Minnesota. These functionals are meta-Generalized Gradient Approximations (GGA) [85, 89], i.e. they include terms that depend on the kinetic energy density and are based on flexible functional forms parametrized on high-quality benchmark databases. The Minnesota functionals have been widely tested in quantum chemistry studies [85, 86, 88, 90, 91].

M06-2X [86, 90] is a high nonlocality global hybrid meta-GGA exchange-correlation functional with 54 % HF exchange. It was recommended for applications involving main group thermochemistry, kinetics, noncovalent interactions, and electronic excitation energies to valence and Rydberg states because of its accuracy in the prediction of molecular geometry, vibrational frequencies and correlation energy [90]. The local terms of the M06-2X functional depends on three variables: spin density (ρ_σ), reduced spin density gradient (x_σ), and spin kinetic energy density (τ_σ). The E^{XC} for M06-2X functional is described thoroughly by Zhao and Truhlar [86].

3.1.1.7 Becke-style functionals

The Becke-style "Half and Half" functional with the Lee, Yang, and Parr correlation functional is defined in a similar manner to Equation 3.18. This functional has proven to be quite accurate in the prediction of molecular geometries and vibrational frequencies [92]. The local density approximation (E_{LDA}^X) is applied to obtain an estimation of the exchange energy; however, the gradient-corrected exchange functional (ΔE_{B88}^X) is included as a correction to improve the accuracy of the results. Finally, the correlation energy is determined by the Lee, Yang, and Parr (E_{LYP}^C) correlation functionals. BHandHLYP functional is written as [92]:

$$E_{HandHLYP}^{XC} = 0.5 E_{HF}^X + 0.5 E_{LDA}^X + 0.5 \Delta E_{B88}^X + E_{LYP.}^C \qquad (3.21)$$

The descriptions in detail of E_{LDA}^X, ΔE_{B88}^X and E_{LYP}^C can be found elsewhere [66, 93, 94].

3.1.2 Reaction Kinetics Calculation

The main objective in reaction kinetics is to determine rates of chemical processes. The rate coefficient for a process can be described as e.g. an Arrhenius equation (Equation 1.7), based on the calculation of the temperature-dependent reaction rates. The most widely used theoretical approach for rate coefficient determination is transition state theory (TST), where the reaction mechanism can be obtained from electronic structure calculations in section 3.1.1.

3.1.2.1 Transition state theory (TST)

Transition state theory or activated complex theory [95-98] is based inherently on the potential energy surface, with a statistical description of classical dynamics along the reaction coordinate. TST is a well-stablished theory, with a very good track record as a predictive tool for temperature dependent rate coefficients of uni- and bimolecular reactions in gas phase. TST is based on three assumptions: First, it assumes there is a dividing surface in a phase space that separates a reactant region from a product region. Typically, it is assumed that this dividing surface, called the transition state (TS), is located at the maximum value on the minimum energy path (MEP) of the potential energy surface connecting the reactant and product. Any trajectory passing through this dividing surface from the reactant side is assumed to cross only once and then form the product. This is also called the non-recrossing rule. Second, the reactant and TS are assumed to maintain the equilibrium Boltzmann energy distribution. Finally, all activated complexes have properties that can be approximated by those of the transition state. Other important approximations include the assumption that the reaction coordinate is separable from the other degrees of freedom and that *ad hoc* corrections for quantum effects, e.g. tunneling probabilities, are valid.

Hydrogen abstraction reaction is a common type of bimolecular reaction. A typical plot of the potential energy versus reaction coordinate for hydrogen abstraction reaction is shown in Figure 3.1. This one-dimensional PES plot along the reaction coordinate

represents the transition of a hydrogen atom from its reactant position to its product position, where the transition state is encountered at the point with highest potential energy along the reaction coordinate. The energy barrier E_b is the potential energy difference between the reactants and TS. The TS thus represents the unstable structure between the reactants and the products:

$$RH + X \rightarrow RH \cdots X \rightarrow [R \cdots H \cdots X]^{\ddagger} \rightarrow R \cdots HX \rightarrow R + HX. \tag{R3.1}$$
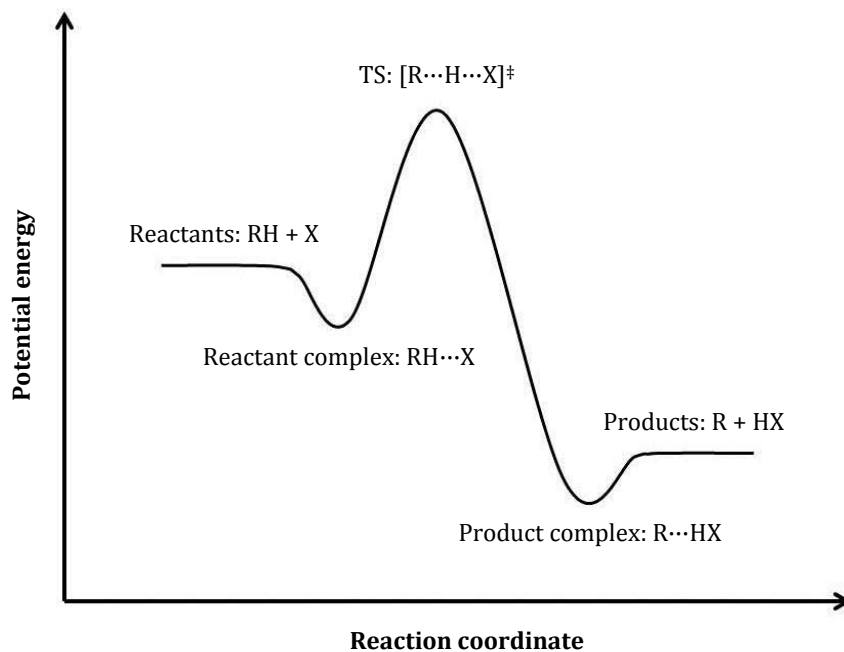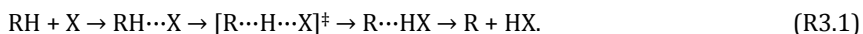
Figure 3.1   An example PES along reaction coordinates for the hydrogen abstraction reaction.

In hydrogen abstraction reactions, two reactants first come together to form a reactant van der Waals complex. If this complex has sufficient energy, it can proceed along the reaction coordinate, reaching the transition state. Once a transition state is passed the

products are formed, first through a van der Waals complex which will then fall apart to produce the separated products.

The temperature dependent rate coefficient, $k(T)$, for a hydrogen abstraction reaction $RH + X \rightarrow R + HX$ is expressed within a TST paradigm as:

$$k(T) = \alpha \frac{k_B T}{h} \frac{Q^{\ddagger}(T)}{Q^R(T)} \kappa(T) \exp\left(\frac{-E_b}{k_B T}\right) \tag{3.22}$$

where α is the reaction symmetry number, k_B is Boltzmann's constant, T is the temperature, h is Planck's constant, $Q^{\ddagger}$ is the transition state partition function, excluding the reaction coordinate, Q^R is the total partition function of the reactant RH and X which includes all degrees of freedom, and $\kappa(T)$ is the tunneling correction factor. The reaction coordinate is treated as a separate translational degree of freedom that takes the system over an E_b. For atmospheric conditions, the accuracy of rate coefficient prediction depends mostly on the accuracy of E_b, and, especially for H-migrations, the tunneling correction. All quantities should account correctly for ZPE (zero-point vibrational energy)

The reaction symmetry number represents the number of indistinguishable ways the reactants may approach the activated complex region, given by:

$$\alpha = \frac{\sigma_R}{\sigma_{TS}} \frac{o_{TS}}{o_R} \frac{g_{TS}}{g_R} \tag{3.23}$$

where σ is the rotational symmetry number, o is the number of optical isomers and g is the electronic state degeneracy for reactants and TS (indicated by subscript R and TS, respectively).

3.1.2.2 Partition functions

Statistical properties of a system in thermodynamic equilibrium are described by the partition functions. The total partition function is the product of partition functions

contributed from translation (t), electronic excitation (e), rotational motion (r), and vibrational motion (v) as:

$$Q(T) = Q_t Q_e Q_r Q_v \tag{3.24}$$

In general, the partition functions can be calculated from the energy levels E_i, the degeneracy of each level g_i, and temperature T:

$$Q(T) = \sum_i g_i exp\left(\frac{-E_i}{k_B T}\right) \tag{3.25}$$

Translational partition function Q_t for a molecule is dependent on molecular mass (m) and temperature (T). The translational partition function can be calculated from the following equation [99]:

$$Q_t = \frac{(2\pi m k_B T)^{\frac{3}{2}}}{h^2} \cdot Vol = \frac{(2\pi m k_B T)^{\frac{3}{2}}}{h^2} \frac{k_B T}{P} \tag{3.26}$$

where k_B is Boltzmann's constant, Vol is volume in m^3, and P is pressure in $N \cdot m^{-2}$.

Electronic partition function Q_e for a molecule is dependent on temperature (T). The electronic partition function is expressed as follows [99]:

$$Q_e = \sum_i g_i exp\left(\frac{-E_i}{k_B T}\right) \tag{3.27}$$

where g_i represents the degeneracy of the ith electronic state located at energy E_i above the ground state. The spin multiplicity of the electrons is accounted for in this way, where the degeneracy of the closed-shell species, e.g. ethane molecule, is one, while a hydroxyl radical and a doublet open shell TS have a degeneracy of 2. We also use it in this work to account for the spin-orbit splitting of the OH radical.

Rotational partition function Q_r for a molecule is dependent on the moments of inertia around the principle axes of rotation (I_A, I_B and I_C) in the molecule, and on temperature. Two general expressions apply, depending on whether the molecule is a linear or nonlinear molecule. In the case of a linear molecule , e.g. OH radical, Equation 3.28 is used to determine the rotational partition function [99]. For a general nonlinear polyatomic molecule, e.g. ethane and TS, Equation 3.29 is used to determine the rotational partition function. The rotational symmetry number (σ) represents the number of indistinguishable orientations that may be obtained by the rigid spatial rotation of the molecule.

$$Q_{r,linear} = \frac{8\pi^2 I k_B T}{\sigma h^2} \tag{3.28}$$

$$Q_{r,nonlinear} = \frac{8\pi^2 (8\pi^3 I_A I_B I_C)^{\frac{1}{2}} (k_B T)^{\frac{3}{2}}}{\sigma h^3} \tag{3.29}$$

In the case of the reaction of OH with ethane, the symmetry groups of ethane, OH, and TS are D_{3d}, $C_{\infty v}$, and C_1, respectively. Hence rotational symmetry numbers for ethane, OH, and TS are 6, 1, and 1, respectively. For ethane with one ^{13}C atom, the two carbon atoms are distinguishable, and thus $\sigma = 3$.

Vibrational partition function Q_v can be determined from the vibrational frequencies, v_i, of each fundamental mode (i). Only the stable modes are considered; transient modes with imaginary frequencies are ignored. In general, the vibrational partition function for harmonic vibrations can be evaluated from the Equation 3.30 [99]. The zero-point energy of each vibration is normally excluded from this calculation, but rather is included in the energy component in the final calculation of the rate coefficient.

$$Q_v = \prod_i \left(\frac{1}{1 - \exp\left(\frac{-h v_i}{k_B T}\right)} \right)^{-1} \tag{3.30}$$

3.1.2.3 Anharmonicity of vibration

Traditionally, the harmonic oscillator approximation is used to compute the vibrational partition function and the energy levels of given potential energy surface by simple functions of fundamental mode frequencies (Equation 3.30). These harmonic oscillators are uncoupled i.e. vibrational frequencies of fundamental modes are independent of each other and the total energy is the sum of vibrational energies of each fundamental mode. Unfortunately, the harmonic approximation can lead to the fairly inaccurate partition functions and rate coefficients. A possible improvement involves the use of Morse energy potentials. These reproduce the energy profile of a vibration more faithfully, because it explicitly includes the effect of bond breaking, accounts for the energetic asymmetry of real bonds, and allows for non-zero transition probability for overtone and combination bands. When anharmonicity is introduced, the third- and higher-order derivatives of potential energy are taken into account and as a consequence the fundamental modes are no longer independent but coupled.

Anharmonicity constants can be obtained by using second-order vibrational perturbation theory (VTP2) which allows for the generation of the full cubic force field and semi-diagonal quartic force field of the potential energy through finite differences from the analytic second derivatives. Partition functions for anharmonic approximated vibrational energy levels can then be computed from anharmonicity constants and harmonic vibrational frequencies using direct count methods aided by Monte Carlo sampling, as discussed in more detail below.

3.1.2.4 Internal rotation treatment

Internal rotations should be accounted for in the prediction of thermodynamic and kinetic properties because 1) the difference between an internal and harmonic vibration leads to different absolute state densities and a different energy-dependence, and 2) multiple conformers exist for hindered internal rotors, which cannot be described by a single structure. Most internal rotors are hindered internal rotors, for which the potential

energy depends on the angle of rotation. Inclusion of the modes corresponding to hindered internal rotors as harmonic oscillators in Equation 3.30 usually results in significant error associated with the total partition function. As such, separate expressions have been developed to approximate the partition function of the hindered internal rotor. When applicable, the modes corresponding to hindered internal rotation are excluded from Equation 3.30 and the approximated hindered internal rotational partition function (Q_{hr}) is added instead to Equation 3.24. Q_{hr} is characterized by the number of minima and maxima per 2π rotation, and by the symmetry of the potential energy, and whether the mass distribution around the rotor axis can be approximated as symmetric. For ethane and the TS of ethane + OH, one mode corresponds to the rotation of the methyl group. The potential energy surface for the CH_3 internal rotation is 3-fold symmetric with a symmetrical mass distribution. The partition function Q_{hr} [100] can be calculated as :

$$Q_{hr} = \frac{1}{\sigma_{hr}} \sum_i \exp\left(\frac{-E_{hr,i}}{k_B T}\right) \tag{3.31}$$

where $E_{hr,i}$ is the energy eigenvalue at i^{th} state and σ_{hr} is 3 for ethane and 1 for an unsymmetrical internal rotor.

The potential energy function $V(\chi)$ and the reduced moment of inertia $I(\chi)$ or rotational constant $B(\chi)$ as a function of dihedral angle are required to calculate internal rotor eigenvalues, and can be described as the following Fourier expansions.

$$V(\chi) = V_0 + \sum_n V_n cos\big(n\sigma_V(\chi + \varphi_V)\big) \tag{3.32}$$

$$I(\chi) = I_0 + \sum_n I_n cos\big(n\sigma_I(\chi + \varphi_I)\big) \tag{3.33}$$

$$B(\chi) = B_0 + \sum_n B_n cos\big(n\sigma_B(\chi + \varphi_B)\big) \tag{3.34}$$

In above expressions, χ represents the dihedral angle in radians, σ is the symmetry number, φ is a phase angle in radians, and the subscripts V, I, and B refer to parameters for

potential energy function, reduced moment of inertia, and rotational constant, respectively. The parameters σ and φ are simply for convenience in curve fitting.

3.1.2.5 Semi-classical transition state theory (SCTST)

SCTST was developed by Miller and co-workers [101-105] to remove some of the approximations made in traditional TST by incorporating explicitly non-separable coupling among all degrees of freedom including the reaction coordinate in the transition state region. Moreover, SCTST accounts for multidimensional semi-classical tunneling along the curved reaction path and automatically includes the effects of fully-coupled anharmonic vibrational modes. This eliminates the need for *ad hoc* corrections as in TST. The SCTST thermal rate coefficients were reported to be in close agreement with those of full quantum dynamic calculations and experiments [36, 103-107]. However, the SCTST method has been limited to very small reaction systems, to only 6 atoms, because of the large number of quantum states that must be computed for larger systems [36, 103-107].

SCTST has been described extensively in the literature [101-105]. The microcanonical rate coefficient, $k(E)$, is written:

$$k(E) = \frac{1}{h}\frac{G^{\ddagger}(E)}{\rho(E)} \tag{3.35}$$

where h is Planck's constant, $\rho(E)$ is the density of states of the reactant, and $G^{\ddagger}(E)$ is the cumulative reaction probability (CRP).

The canonical rate coefficient, $k(T)$, can be expressed as the thermal average of $k(E)$:

$$k(T) = \frac{1}{h}\frac{\int_{-\infty}^{\infty} G^{\neq}(E)\exp\left(\frac{-E}{k_B T}\right)dE}{Q^R(T)} \tag{3.36}$$

where k_B is Boltzmann's constant, T is the temperature, and Q^R is the total partition function of the reactant(s).

The center of mass translations are rigorously separable. At moderate temperatures, it is a good approximation to treat the overall rotations as separable from the vibrations (including internal rotations), so that Equation 3.31 can be written:

$$k(T) = \frac{1}{h} \frac{Q_t^{\ddagger} Q_r^{\ddagger}}{Q_t^R Q_r^R} \frac{\int_{-\infty}^{\infty} G_v^{\ddagger}(E_v) \exp\left(\frac{-E_v}{k_B T}\right) dE_v}{Q_v^R(T)} \tag{3.37}$$

in which vibrational energy E_v is the variable of integration. The corresponding CRP is given by

$$G_v^{\ddagger}(E_v) = \sum_{n_1} \sum_{n_2} \cdots \sum_{n_{F-2}} \sum_{n_{F-1}} P_n(E_v) \tag{3.38}$$

where F number of internal degrees of freedom of the transition state orthogonal to the reaction coordinate. The semi-classical tunneling probability P_n is given by

$$P_n(E_v) = \frac{1}{1 + \exp[2\theta(n, E)]} \tag{3.39}$$

The barrier penetration integral $\theta(n,E)$ and related quantities are given by

$$\theta(n, E) = \frac{\pi \Delta E}{\Omega_F} \frac{2}{1 + \sqrt{1 + \frac{4 x_{FF} \Delta E}{\Omega_F{}^2}}} \tag{3.40}$$

where

$$\Delta E = \Delta V_0 + E_0 - E + \sum_{k=1}^{F-1} \omega_k \left(n_k + \frac{1}{2}\right) + \sum_{k=1}^{F-1} \sum_{l=k}^{F-1} x_{kl} \left(n_k + \frac{1}{2}\right)\left(n_l + \frac{1}{2}\right) \tag{3.41}$$

$$\Omega_F = \overline{\omega}_F - \sum_{k=1}^{F-1} \bar{x}_{kF} \left(n_k + \frac{1}{2}\right) \text{ with } \overline{\omega}_F = -i\omega_F \text{ and } \bar{x}_{kF} = -ix_{kF} \tag{3.42}$$

In these expressions, ω_k is the harmonic vibrational frequency of the kth vibrational mode, ω_F is the imaginary frequency associated with the reaction coordinate, x_{kl} are the vibrational anharmonicity constants that describe coupling among the degrees of freedom orthogonal to the reaction coordinate, x_{kF} are the (pure imaginary) coupling terms between the reaction coordinate and the orthogonal degrees of freedom, x_{FF} is the (pure real) anharmonicity constant for the reaction path, and ΔV_0 is the classical barrier height. The term E_0 is a constant, which depends on the cubic and quartic force constants. Terms labeled as anharmonic zero-point energies, E_{ZPE}, of the orthogonal modes always incorporate E_0:

$$E_{ZPE} = E_0 + \frac{1}{2}\sum_{k=1}^{F-1}\omega_F + \frac{1}{4}\sum_{k=1}^{F-1}\sum_{l=k}^{F-1} x_{kl}. \tag{3.43}$$

The partition function for anharmonic vibrations for reactants can be computed by:

$$Q_v^R = \int_0^{E_{max}} \rho(E_v)\exp\left(\frac{-E_v}{k_BT}\right)dE_v \tag{3.44}$$

where E_{max} is ideally equal to infinity, but for computational purposes is set to a large but finite energy.

3.2   Computational Details

The electronic structure calculations associated with *ab initio* and density functional are sufficiently complicated so that sophisticated software packages are required. In this work, the Gaussian09 software package [108] at Max-Planck Institute of Chemistry, Mainz, Germany was used to obtain the geometries, vibrational frequencies, and energies of the molecular species involved in hydrogen abstraction reaction of ethane by the OH radical. The MultiWell program suite [109, 110] version 2014.1 was employed to calculate thermal

rate coefficients for reactions R1.8, R1.9a, and R1.9b as well as the temperature dependence of the overall KIE.

3.2.1 Geometry Optimizations

The molecular geometries of stationary points including ethane, OH radical, TS, ethyl radical and water were initially constructed in GaussView [108]. Geometry optimizations for the local minima and transition states were performed using *opt* keyword with the Berny algorithm using GEDIIS [111] in redundant internal coordinates [112, 113]. The initially constructed geometries for all stationary points were optimized at BHandHLYP/cc-pVDZ. Then, the BHandHLYP/cc-pVDZ optimized geometries of involved species were again re-optimized at M06-2X/aug-cc-pVTZ using *VeryTight* keyword for extremely tight optimization convergence criteria, using a benchmark-quality 99,974 DFT integration grid and very tight SCF convergence criteria

The geometry of TS was initially located by performing a search along the molecular potential energy surface using the quadratic Synchronous Transit Quasi-Newton (STQN) method [114] at BHandHLYP/cc-pVDZ by using *opt=QST3* keyword which requires three molecular specifications including the reactant, product, and initial TS structures. The BHandHLYP/cc-pVDZ QST3 optimized TS geometry was further re-optimized at M06-2X/aug-cc-pVTZ, as above.

3.2.2 Anharmonic Vibrational Frequencies

The force constants and the resulting harmonic vibrational frequencies as well as zero-point energies of the involved species were computed by determining the second derivatives of the energy with respect to the Cartesian nuclear coordinates along vibrational modes and then transforming to mass-weighted coordinates. Calculation of the vibrational frequencies and zero-point energies as well as anharmonicity constants were performed on the optimized geometries for each species by VPT2 using *freq=anharm* keyword at M06-2X/aug-cc-pVTZ, which involves calculating the third, and part of the

fourth derivatives of the PES. Scale factors for harmonic vibrational frequencies and zero-point energies of 0.971 were introduced [115].

The keyword *(Iso=13)* was used to indicate ^{13}C atom in ^{13}C isotopes of ethane, TS and ethyl radicals (R1.8, R1.9a, and R1.9b). The different positions of the label carbon in the TS and ethyl radicals lead to distinguishable mechanisms R1.8, R1.9a, and R1.9b.

3.2.3 Internal rotation

The modes for internal rotation were further characterized at the M06-2X level of theory. For the symmetric rotation of the methyl group in ethane and the TS, the barrier for internal rotation was optimized; for the TS, this implies optimizing a second order saddle point. The rotation of the OH moiety along the CHO axis was investigated by calculating the energy profile along the angle of rotation, using reduced-dimensionality optimizations where the CCOH dihedral angle was fixed. The inclusion of internal rotation in the kinetic calculations is discussed in more detail below.

3.2.4 Energy Barriers

Energy calculations were performed on the M06-2X/aug-cc-pVTZ optimized structures using *ab initio* theory coupled cluster calculations with single, double, and triple substitutions, i.e. CCSD(T). These energy calculations were performed using an augmented Dunning's correlation-consistent polarized valence with double, triple-, and quadruple zeta basis set (aug-cc-pVxZ, x = D,T,Q), with extrapolation to the complete basis set limit (CBS) using the 3-parameter expression aug-Schwartz6 (DTQ) [116].

3.2.5 Thermal rate coefficients and KIE

Computer programs SCTST [101-103, 105, 106] and ADENSUM [117-119] for computing the CRP for the TS and the partition function for the reactants, accounting for anharmonic coupled vibrations and internal rotation , were used in conjunction with program THERMO to compute the thermal rate coefficients $k(T)$; all three codes are

included in the MULTIWELL Program Suite. For the number of samples for the semi-classical calculations in ADENSUM and SCTST, the keyword *BEST* was used to specify the number of samples in each energy bin as 10^5 samples per bin. In all calculations, the energy grain size used for computing the numerical density of states was set to 5 cm^{-1}, which is $\ll k_B T$, even at the lowest temperatures considered in this work. The maximum energy, E_{max} was set to 20,000 cm^{-1}, which is sufficiently high so that it does not significantly truncate the thermal population distribution at T ≤ 2000 K. The temperature dependent KIE (ε) can be calculated from $k_{12}(T)$ and $k_{13}(T)$ as Equation 1.24.

3.3 Results and Discussion

3.3.1 Electronic properties of stationary points

The optimized geometries at the M06-2X/aug-cc-pVTZ level of theory for stationary points involving in the reaction C_2H_6 + OH $\rightarrow$ C_2H_5 + H_2O (Reaction R1.1) including reactants (C_2H_6 + OH), reactant complex (RC), transition state (TS), product complex (PC) and products (C_2H_5 + H_2O) are shown in Figure 3.2. Their optimized geometrical parameters at the same level of theory are listed in Table 3.1. The coordinates of optimized structures can be found in section A.6.1 in the Appendix.
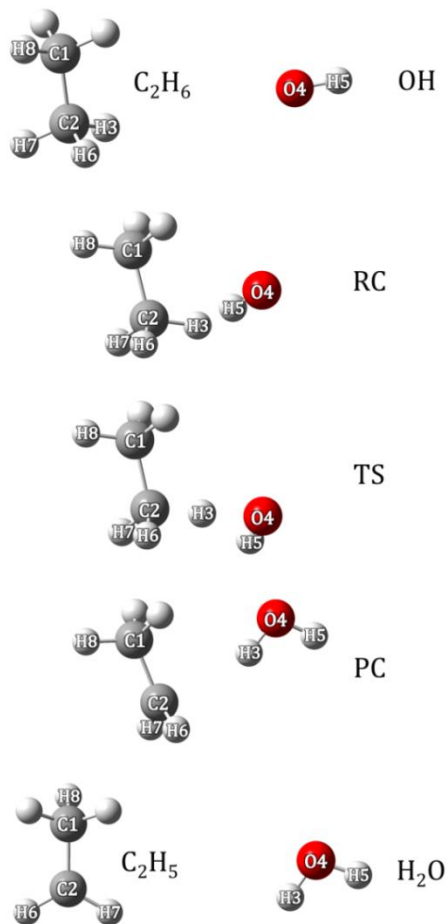
Figure 3.2 Optimized geometries of stationary points including reactants (C_2H_6 + OH), reactant complex (RC), transition state (TS), product complex (PC) and products (C_2H_5 + H_2O) at M06-2X/aug-cc-pVTZ.

Table 3.1 Optimized geometrical parameters of stationary points including reactants (C_2H_6 + OH), reactant complex (RC), transition state (TS), product complex (PC) and products (C_2H_5 + H_2O) at M06-2X/aug-cc-pVTZ. Values in parentheses were taken from literatures (see table footnote).

Parameters	C_2H_6 + OH	RC	TS	PC	C_2H_5 + H_2O
Bond length (Å)					
C1-C2	1.524 (1.523/1.522)[e] (1.524)[g] (1.536)[j]	1.524 (1.534)[a] (1.516)[b]	1.512 (1.524)[a] (1.511)[b] (1.511/1.513)[e]	1.486 (1.499)[a] (1.503)[b]	1.484 (1.492)[l]
C2-H3	1.090 (1.094/1.091)[e] (1.090)[g] (1.091)[j]	1.092 (1.100)[a] (1.088)[b]	1.161 (1.180)[a] (1.187)[b] (1.22/1.18)[c] (1.189)[d] (1.270/1.173)[e] (1.187)[f]	2.301 (2.325)[a] (1.492)[b]	n/a
H3-O4	n/a	3.071 (2.632)[a] (1.581)[b] (2.578)[f]	1.435 (1.384)[a] (1.322)[b] (1.27/1.34)[c] (1.322)[d] (1.287/1.361)[e] (1.322)[f]	0.964 (0.970)[a] (1.017)[b]	0.959 (0.957)[h] (0.958)[k]
O4-H5	0.972 (0.970)[i]	0.973 (0.975)[a] (0.973)[b]	0.970 (0.974)[a] (0.971)[b] (0.95/0.97)[c] (0.971)[d] (0.973/0.968)[e]	0.959 (0.966)[a] (0.966)[b]	0.959 (0.957)[h] (0.958)[k]
C2-H6	1.090 (1.094/1.091)[e] (1.090)[g] (1.091)[j]	1.092 (1.089)[b]	1.089 (1.087)[b] (1.102/1.089)[e]	1.080 (1.085)[b]	1.079 (1.081)[l]

Table 3.1   Continued

Parameters	C$_2$H$_6$ + OH	RC	TS	PC	C$_2$H$_5$ + H$_2$O
Bond length (Å)					
C2-H7	1.090 (1.094/1.091)[e] (1.090)[g] (1.091)[j]	1.089 (1.089)[b]	1.088 (1.087)[b] (1.102/1.089)[e]	1.080 (1.085)[b]	1.078 (1.081)[l]
C1-H8	1.090 (1.094/1.091)[e] (1.090)[g] (1.091)[j]	1.089 (1.089)[b]	1.092 (1.089)[b]	1.097 (1.093)[b]	1.097 (1.099)[l]
Bond angles (degree)					
C1-C2-H3	111.2 (111.4/111.3)[e] (112.0)[g] (110.9)[j]	111.5 (111.0)[a] (109.7)[b]	108.2 (107.0)[a] (107.7)[b] (107.7/108.0)[e]	85.3 (85.9)[a] (106.5)[b]	n/a
C2-H3-O4	n/a	96.4 (168.3)[a] (159.4)[b]	170.3 (178.0)[a] (169.6)[b] (170.66/165.57)[c] (169.0)[d] (179.2/169.9)[e]	156.9 (159.6)[a] (169.9)[b]	n/a
H3-O4-H5	n/a	17.2 (175.1)[a] (95.1)[b]	96.8 (96.1)[a] (97.6)[b] (97.6)[d] (95.7/96.0)[e]	105.5 (104.0)[a] (100.4)[b]	105.3 (104.52)[h] (104.48)[k]
H3-C2-H6	107.6 (108)[j]	108.5 (105.0)[b]	104.5 (104.3)[b] (104.3/104.2)[e]	99.3 (102.8)[b]	n/a
H3-C2-H7	107.6 (108)[j]	106.8 (109.1)[b]	106.5 (106.7)[b] (104.2/106.6)[e]	99.4 (103.4)[b]	n/a
H6-C2-H7	107.6 (108)[j]	106.8 (108.3)[b]	109.9 (110.0)[b]	117.2 (112.0)[b]	117.7 (117.8)[l]

Table 3.1   Continued

Parameters	C$_2$H$_6$ + OH	RC	TS	PC	C$_2$H$_5$ + H$_2$O
Bond length (Å)					
C1-C2-H6	111.2 (111.4/111.3)[e] (112.0)[g] (110.9)[j]	111.5 (112.0)[b]	113.7 (113.9)[b]	120.4 (115.5)[b]	120.8 (120.7)[l]
C1-C2-H7	111.2 (111.4/111.3)[e] (112.0)[g] (110.9)[j]	111.5 (112.4)[b]	113.4 (113.5)[b]	120.5 (115.0)[b]	120.8 (120.7)[l]
C1-C2-H8	111.2 (111.4/111.3)[e] (112.0)[g] (110.9)[j]	111.0 (110.1)[b]	110.7 (110.8)[b]	111.2 (109.8)[b]	111.8 (111.7)[l]
Dihedral angels (degree)					
C1-C2-H3-O4	n/a	74.0 (318.3)[a]	-78.23 (180.0)[a] (-176.1/-49.1)[e]	0.2 (0.0)[a]	n/a
C2-H3-O4-H5	n/a	41.0 (259.6)[a] (52.5)[b]	-46.4 (180.0)[a] (39.3)[b] (-34.83/-35.82)[c] (-3.4/-24.0)[e]	179.9 (180.0)[a] (36.0)[b]	n/a
O4-H3-C2-H6	n/a	-49.3	160.3 (-54.3/-25.5)[e]	-120.0	n/a
O4-H3-C2-H7	n/a	-164.0	43.9 (61.9/74.3)[e]	120.2	n/a
H6-C1-C2-H8	-60.0 (-60.0)[g] (-60.0)[j]	-59.4	-63.6	-81.9	-90.0 (-90.0)[l]
H7-C1-C2-H8	60.0 (60.0)[g] (60.0)[j]	59.4	62.9	82.0	90.0 (90.0)[l]

Table 3.1 footnote:

[a] Computed at UMP2/aug-cc-pVDZ by Hashimoto and Iwata [57]

[b] Computed at MP2/6-31G(d,p) by Martell et al. [58]

[c] Computed at BHandHLYP/ 6-311G(d,p) and MP2/6-311G(d,p) by G. Bravo-Pérez et al. [54]

[d] Computed at MP2/6-31G(d,p) by Aliagas and Gronert [59]

[e] Computed at CASSCF(6,6)/cc-pVTZ and CASPT2(6,6)/cc-pVTZ for ethane;
CASSCF(6,6)/cc-pVTZ and UMP2/cc-pVTZ for TS by Yan et al. [56]

[f] Computed at MP2/6-31G(d,p) by Sekušak et al. [60]

[g] Experiment by Harmony [61]

[h] Experiment by Benedict et al. [62]

[i] Experiment by Huber et al. [63]

[j] Experiment by Herzberg [64]

[k] Experiment by Hoy and Bunker [65]

[l] Computed at CCSD(T)/cc-pVTZ from NIST database [120]

The optimized geometries of stationary points are in good agreement with available experimental and theoretical studies, except those of the reactant complex which are found to be less stable than in the previous studies. The optimized geometry of ethane was found to be in a staggered form. The transition state in the reaction can be described approximately as a collinear arrangement (170.3°) between the carbon atom of ethane, the hydrogen atom undergoing abstraction, and the oxygen atom of hydroxyl radical (C⋯H⋯O). An almost collinear arrangement between the OH, hydrogen, and carbon atoms seems to be typical for hydrogen atom abstraction reactions by OH radicals. The arrangement of TS C-H bonds was found to be staggered as well as the reactant. This implies that the reactant ethane does not require rotating energy in order to turn into the transition state. The O-H bond of hydroxyl radical lies in eclipsed arrangement to C-H bond at abstracted carbon. After the hydrogen atom was abstracted, it was found that the plane of sp^2-carbon in ethyl radical was perpendicular to a C-H bond of sp^3-carbon. The TS was confirmed by fundamental mode analysis having only one imaginary frequency whose mode corresponds to movement of the hydrogen atom being abstracted, away from the carbon atom to which it is bonded, and toward the abstracting oxygen atom. The M06-2X imaginary frequency of TS was found to be 683i cm^{-1}. The imaginary frequency often

correlates to the width of the barrier and has a significant role in the tunneling effect, which plays a critical role at low temperature.

M06-2X method results gives reliable optimized geometries and vibrational frequencies but not energies. Therefore, CCSD(T) calculations extrapolated to the complete basis set (CBS) were introduced to calculate more accurate energies for ethane, hydroxyl radical, RC, TS, and PC. This refinement of the PES by CCSD(T)/CBS results in a slight increase in the reaction barrier height E_b, with energy differences for the TS of 0.74, 0.65, and 1.28 kcal mol^{-1} relative to the reactants, RC, and PC, respectively. In SCTST, the term E_v in equation 3.37 is described by the energy difference between reactants and TS, while the relative energies of the RC and PC contribute to the tunneling effect description through the term ΔE in Equations 3.40-3.41.

The potential energies derived above are subsequently corrected for vibrational zero-point energy (ZPE), where each stationary point has a different ZPE due to its different vibrational characteristics. The M06-2X/aug-cc-pVTZ harmonic ZPE correction (scaled by 0.971 [115]) thus leads to the altering of E_b in both forward and reverse directions, which has a substantial effect in rate coefficient calculation. ZPE correction lifts up the PES by around 49-52 kcal mol^{-1}, but only affects the relative energies by a few kcal mol^{-1}.

In SCTST calculation, the CRP (comparable to vibrational partition function of TS in conventional TST) and the vibrational partition function of reactants account for the anharmonicity of vibration. Therefore, anharmonicity analysis for ethane and TS vibrations were carried out. Anharmonicity constants of fundamental modes were also included in refined ZPE calculation for ethane and TS. Harmonic vibrational frequencies for all stationary points and anharmonicity constants for ethane and TS are additionally listed in Section A.6.3 in the Appendix.

Some of the low-frequency modes in TS and ethane are not vibrations, but rather are associated with internal rotation. The TS mode at 55 cm^{-1} is best described as a rotation

along HO⋯H⋯C_2H_5 (C2–O4 axis) in the TS. The rotation along CH_3–CH_2OH (C1–C2 axis) is found at 343 cm^{-1} in the TS, and at 306 cm^{-1} in the reactants. The barrier heights for internal rotation for OH rotation in TS, CH_3 rotation in TS and CH_3 rotation in ethane calculated at M06-2X/aug-cc-pVTZ level of theory were found to be 0.08, 2.40, and 2.78 kcal mol^{-1}, respectively. This indicates that the internal rotations play an important role on the potential energy surface. As these modes are fundamentally different from vibrations, their description as anharmonic vibrations is not correct, and leads to inaccurate partition functions. Hence a hindered rotor treatment is required in the rate calculations.

The potential energy (V) profiles for CH_3 rotation along C1–C2 axis in TS and ethane as a function of dihedral angle (χ) were found to be 3-fold symmetrical, corresponding to three sets of C–H bond eclipses taken pairwise. In contrast, the potential energy profile for OH rotation along C2–O4 axis in TS is illustrated in Figure 3.3, and shows two energy maxima with heights of 0.076 kcal mol^{-1} at 80 and 160 degrees, corresponding to O4–H5 and C2–H6 or C2–H6 eclipses. Another maximum with the height of 0.042 kcal mol^{-1} at 300 degrees relates to O4–H5 bond and ethyl C2–H3 repulsion. The potential energy function as a function of the dihedral angle $V(\chi)$ for OH rotation along C2–O4 axis in the TS can be described by Fourier expansions (Equation 3.32) as following:

$$V(\chi) = 41.19 + 30.70 \cos(\chi - 121.55) + 12.26 \cos\big(2(\chi - 121.5)\big)$$
$$- 19.21 \cos\big(3(\chi - 121.5)\big)$$

(3.45)

where V corresponds to potential energy as a consequence of OH internal rotation in cal mol^{-1} and is χ represents dihedral angle in degree. The moment of inertia for this rotation was nearly constant along the rotation, and was approximated as a constant I = 0.8517 amu $Å^2$.
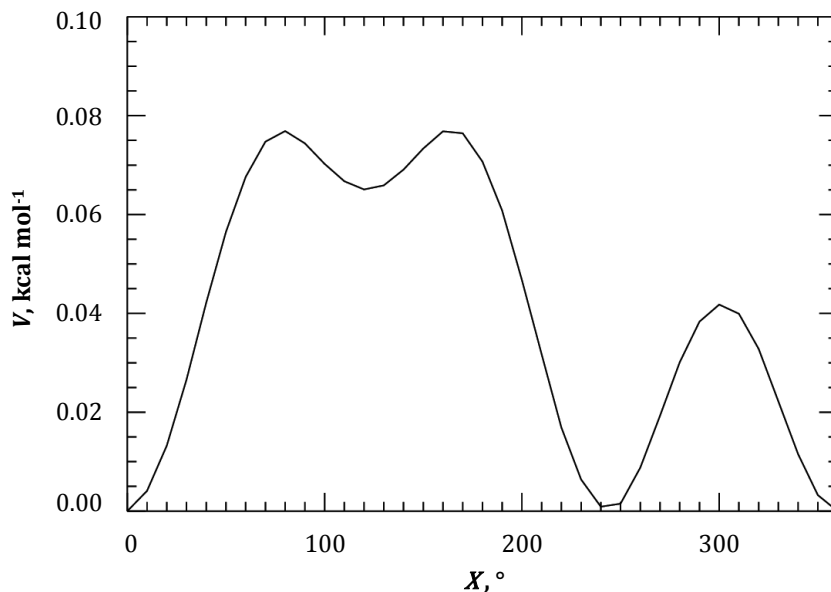
Figure 3.3 Potential energy profile (V) in kcal mol^{-1} for OH rotation in TS as a function of dihedral angle (χ) along C2–O4 axis calculated at M06-2X/aug-cc-pVTZ.

ZPEs are not only dependent on the vibrational frequencies of coupled fundamental modes, but they are also dependent on the internal rotations and low-frequency wagging modes i.e. modes at 101 and 153 cm^{-1} in TS. ZPEs for these modes were described as harmonic vibrations due to the erroneous coupling with the internal rotations.

The composite method used in this study thus calculates the energies using CCSD(T)/CBS on M06-2X/aug-cc-pVTZ optimized geometry and includes anharmonic ZPE corrections (anharm) for most modes, harmonic treatment for two specific vibrational modes (see above), as well as internal rotation treatments (int.rot) calculated at M06-2X/aug-cc-pVTZ level of theory. We denote this by CCSD(T)/CBS//M06-2X/aug-cc-pVTZ//anharm+int.rot. The PES is shown in Figure 3.4.
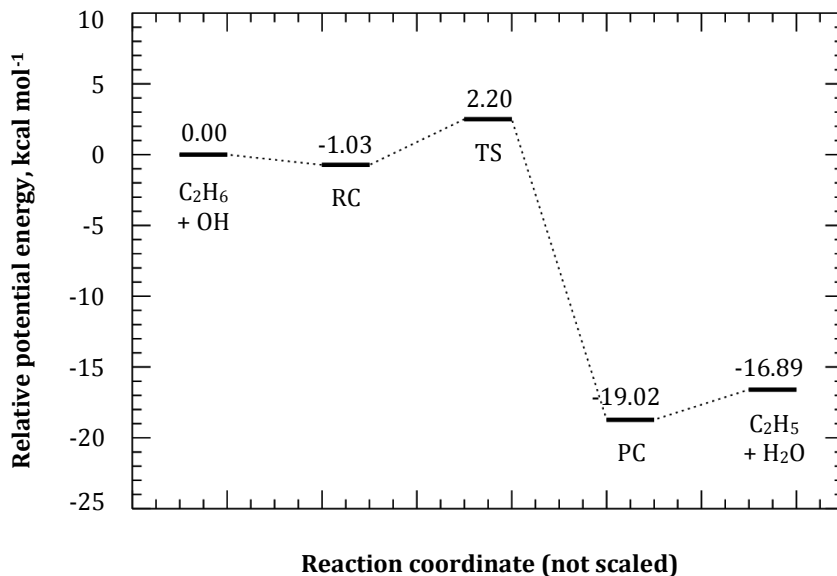
Figure 3.4 ZPE corrected PES for the reaction $C_2H_6 + OH \rightarrow C_2H_5 + H_2O$ obtained at CCSD(T)/CBS//M06-2X/aug-cc-pVTZ//anharm+int.rot presenting relative potential energies of stationary points: reactants ($C_2H_6 + OH$), reactant complex (RC), transition state (TS), product complex (PC), and products ($C_2H_5 + H_2O$) along the reaction coordinate (not scaled).

The refined energy barriers calculated by CCSD(T)//M06-2X/aug-cc-pVTZ//anharm+int.rot level of theory are shown in Table 3.2. Calculated values in this work are in good agreement with the literature values [54, 57, 60]. The full list of energies calculated at M06-2X/aug-cc-pVTZ and CCSD(T)/CBS levels of theory as well as ZPE calculated at M06-2X/aug-cc-pVTZ level of theory can be found in Table A.3 in the Appendix.

Table 3.2   Relative energies in kcal mol^{-1} including ZPE correction in forward and reverse directions calculated at CCSD(T)/CBS//M06-2X/aug-cc-pVTZ// anharm+int.rot level of theory together with the values from the literature.

Relative energies	This study	Literature		
		Bravo-Pérez et al.[a] [54]	Hashimoto and Iwata[b] [57]	Sekušak et al.[c] [60]
Forward direction				
Reactants – TS	2.20	4.71/5.10	4.11/3.58/2.02	5.5/2.9
RC – TS	3.23	-	4.35/3.89/2.32	6.1
Reverse direction				
PC – TS	21.22	-	26.17/21.97/19.95	20.4

Table 3.2 footnote:

[a] Computed at CCSD(T)//BHandHLYP/6-311G(d,p) and CCSD(T)//MP2/6-311G(d,p) [54]
[b] Computed at UMP2/aug-cc-pVDZ, UMP4//UMP2/aug-cc-pVDZ and CCSD(T)//UMP2/aug-cc-pVDZ [57]
[c] Computed at MP2/6-31G(d,p) and G2(MP2) for E_b from reactants to TS [60]

In this work, three different isotopic reaction mechanisms (Reactions R1.9-R1.11) corresponding to different carbon isotopologues along the reaction coordinate are perceived. In this section, Reaction R1.9, R1.11 and R1.10 are denoted by R12, R13a and R13b, respectively, and their stationary points are labeled with C12, C13a, and C13b, correspondingly. To explain these notations briefly, R12 refers to the reaction that its species contain solely ^{12}C atoms; R13 mentions the species of reaction involve one ^{13}C atom; R13a is the mechanism that ^{12}C atom is site of hydrogen abstraction whilst R13b is that ^{13}C atom is site of hydrogen abstraction.

As mentioned earlier, the ZPE is a function of the different vibrational frequencies. C12, C13a and C13b species of ethane, RC, TS, and PC have different reduced masses for

vibration as well as different coordinates of ^{12}C and ^{13}C atom, thus their vibrational frequencies change with the isotopes, leading to different ZPEs. Thus, while the potential energies remain identical, this leads to different PES. PES's of R12, R13a and R13b are shown in Table 3.3 in form of forward and reverse barriers. The energy barrier of R12 is very slightly smaller than those of R13a and R13b (by less than 0.02 kcal mol^{-1}). This could result in non-negligible positive KIE values of the order of just less than 1 % difference in $k(T)$, compared to typical ^{13}C/^{12}C KIE of the order of per mill (‰).

Table 3.3 Relative energies E_{rel} including ZPE correction for forward and reverse direction of different isotopic reaction mechanisms namely R12, R13a and R13b in kcal mol^{-1} calculated at CCSD(T)/CBS//M06-2X/aug-cc-pVTZ// anharm+int.rot level of theory.

E_{rel}	R12	R13a	R13b
Forward direction			
TS – Reactants	2.5005	2.5094	2.5159
TS – Reactant complex	3.2260	3.2265	3.2228
Reverse direction			
TS – Product complex	21.2219	21.2200	21.1999

3.3.2 Calculated thermal rate coefficients and KIE

The method for the KIE determination in the theoretical study is based on different information than the experimental study. Experimentally KIE determination was obtained by an adapted method based on the relative rate concept i.e. monitoring the relationship in the changes of isotopic composition and concentration (see detail in Section 1.5), without determining the actual rate coefficient. On the other hand, theoretical KIE determination is accomplished by calculating absolute rate coefficients for a reaction in which the species

contain solely ^{12}C atoms, k_{12}, and of a reaction involving one ^{13}C atom, k_{13} (Equation 1.23), and then deriving their ratio.

A summary of the SCTST calculated thermal rate coefficients in the temperature range of 150 – 400 K for different isotopic mechanisms: R12 (k_{12}), R13a (k_{13a}), R13b (k_{13b}), and total R13 (k_{13}) where $k_{13} = k_{13a} + k_{13b}$, is presented in Figure 3.5 together with experimentally determined values reported in this work (for details, see Section 2.3) and from literature by Clarke et al. [46], Donahue et al. [51], Talukdar et al. [47], Sharkey and Smith [50], Zabarnick et al. [49], Stachnik et al. [52], Margitan and Watson [48], as well as the values recommended by the IUPAC Subcommittee on Gas Kinetic Data Evaluation for Atmospheric Chemistry [25] derived from Equation 1.8. The SCTST calculated k_{12}, k_{13a}, k_{13b}, and k_{13} values for each temperature in that temperature range are additionally listed in Table 3.4.

From Figure 3.5, the calculated k_{12} in the temperature range of 200-400 K have a good agreement with experimental values from this work and IUPAC recommended values within error ranges. At higher temperatures, the temperature dependence is identical for experimental and theoretical data. Below ~330 K, the theoretically predicted k(T) shows a curved Arrhenius plot, leading to a relative increase of the rate coefficient relative to the experimental data. This curvature is likely indicative of an overestimation of the tunneling effect, which becomes increasingly important at lower temperatures and enhances the rate of reaction. At temperatures lower than 200 K, the calculated k_{12} values are in the same order of magnitude as the experimental values but up to a factor of two overestimated.

The k_{12} values were calculated directly from mechanism R12 because there is only one involved isotopic mechanism. For k_{13} values, there are two isotopic mechanisms to be considered (R13a and R13b), thus k_{13} values were evaluated by the summation of k_{13a} value k_{13b}, as the total rate coefficient is the sum of the two reaction channels available, i.e. H-abstraction from the ^{12}C or the ^{13}C carbon in the isotopically labelled ethane.
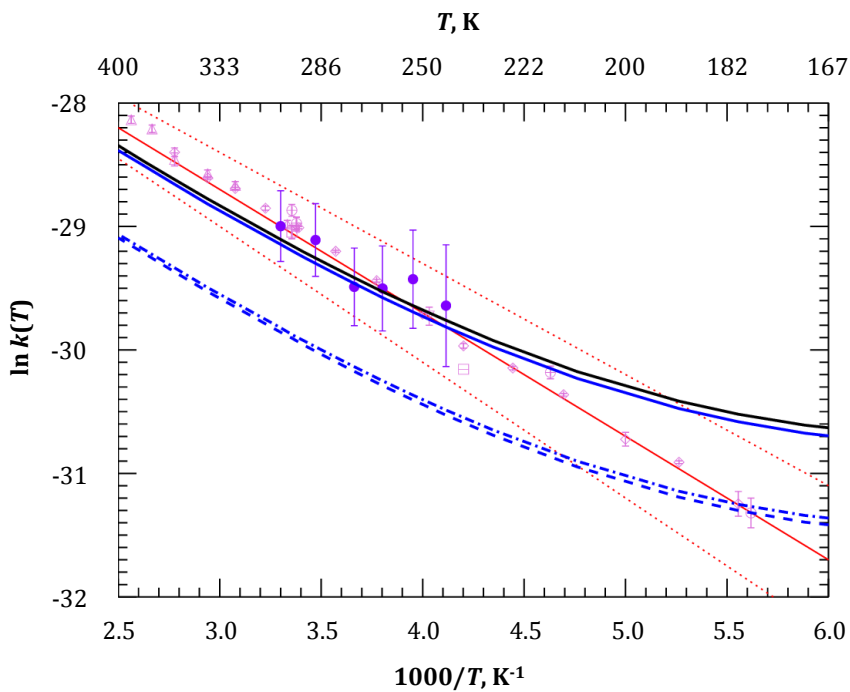
Figure 3.5 SCTST calculated thermal rate coefficients ($k(T)$, cm^3 molecule^{-1} s^{-1}) for the reaction $C_2H_6 + OH \rightarrow C_2H_5 + H_2O$ in different isotopic mechanisms: k_{12} (black solid line), k_{13} (blue solid line), k_{13a} (blue dash-and-dot line), and k_{13b} (blue dash line) comparing with experimental $k(T)$ values from this work (purple full circles) (For details, see Section 2.3), literature data (light purple symbols): Clarke et al. [46] (diamond), Donahue et al. [51] (triangle), Talukdar et al. [47] (square), Sharkey and Smith [50] (circle with dash), Zabarnick et al. [49] (circle), Stachnik et al. [52] (upside-down triangle), and Margitan and Watson [48] (square with dash), and IUPAC recommended values and their uncertainties [25] (Red lines).

Table 3.4   The values of k_{12}, k_{13}, k_{13a} and k_{13b} in cm^3 molecule^{-1} s^{-1}

T, K	k, 10^{-13} cm^3 molecule^{-1} s^{-1}			
	k_{12}	k_{13}	k_{13a}	k_{13b}
150	0.465	0.434	0.224	0.211
160	0.476	0.446	0.229	0.217
170	0.509	0.477	0.245	0.232
180	0.556	0.523	0.268	0.255
190	0.618	0.582	0.298	0.284
210	0.785	0.742	0.380	0.363
230	1.009	0.958	0.489	0.469
243	1.185	1.127	0.575	0.552
253	1.336	1.273	0.649	0.624
263	1.500	1.430	0.729	0.701
273	1.679	1.604	0.817	0.787
283	1.871	1.788	0.911	0.878
293	2.074	1.985	1.010	0.975
298	2.180	2.087	1.062	1.025
303	2.289	2.192	1.115	1.077
340	3.181	3.056	1.553	1.503
360	3.720	3.578	1.817	1.761
380	4.292	4.133	2.098	2.035
400	4.895	4.718	2.394	2.324

The calculated values of k_{13a} and k_{13b} are about half of k_{12} calculated values, as these represent only H-abstraction from one half of the ethane reactant. They are of the same order of magnitude, yet slightly different (by less than 6 %). In the temperature range considered here, the calculated total values of k_{13} (by the combination of the calculated values of k_{13a} and k_{13b}) are slightly smaller than those of k_{12} and the difference increases gradually with decreasing temperature from 3.6 % at 400 K to 6.7 % at 150 K. These differences in the calculated values of k_{12} and k_{13} will be evaluated as KIE values (Equation 1.24).

The Arrhenius-Kooij equations of k_{12} and k_{13} for the reaction $C_2H_6 + OH \rightarrow C_2H_5 + H_2O$ in the tropospheric relevant temperature range of 230 – 400 K are expressed as following:

$$k_{12} = (7.0 \pm 0.1) \times 10^{-13} \left(\frac{T}{298}\right)^{1.75 \pm 0.01} \exp\left(\frac{-347 \pm 6}{T}\right) \qquad (3.46)$$

$$k_{13} = (7.1 \pm 0.1) \times 10^{-13} \left(\frac{T}{298}\right)^{1.72 \pm 0.01} \exp\left(\frac{-364 \pm 6}{T}\right) \qquad (3.47)$$

where k is rate coefficients in cm^3 molecule^{-1} s^{-1} and T is temperature in K.

To probe the sensitivity of the theoretical predictions to a number of key parameters, additional calculations using variations of the kinetic model were performed. Figure 3.6 shows the change in k_{12}, approximately 18 % at room temperature and 40 % at 150 K, as a result of altering E_b for reactants to TS by 0.1 kcal mol^{-1}, i.e. of the order of the expected accuracy of the level of theory used in the calculation. A decrease in E_b shifts the k_{12} values up, and vice versa, but does not change the temperature dependence or the curvature significantly. Figure 3.7 displays the changes in calculated k_{12} when 1) anharmonicity of molecular vibration is excluded, i.e. all vibrational modes are described as harmonic vibrations and 2) the stability of RC is increased by 1 kcal mol^{-1}. Exclusion of vibrational anharmonicity decreases the k_{12} values by 30 % at room temperature and 60 % at 150 K as well as slightly increases k_{12} temperature dependence. The lowering of the RC energy relative to the TS raises the possibility of increased tunneling effect at low

temperature resulting in the increase of the curvature of the Arrhenius plot, and concomitantly increases the overestimation of k_{12} at low temperature.
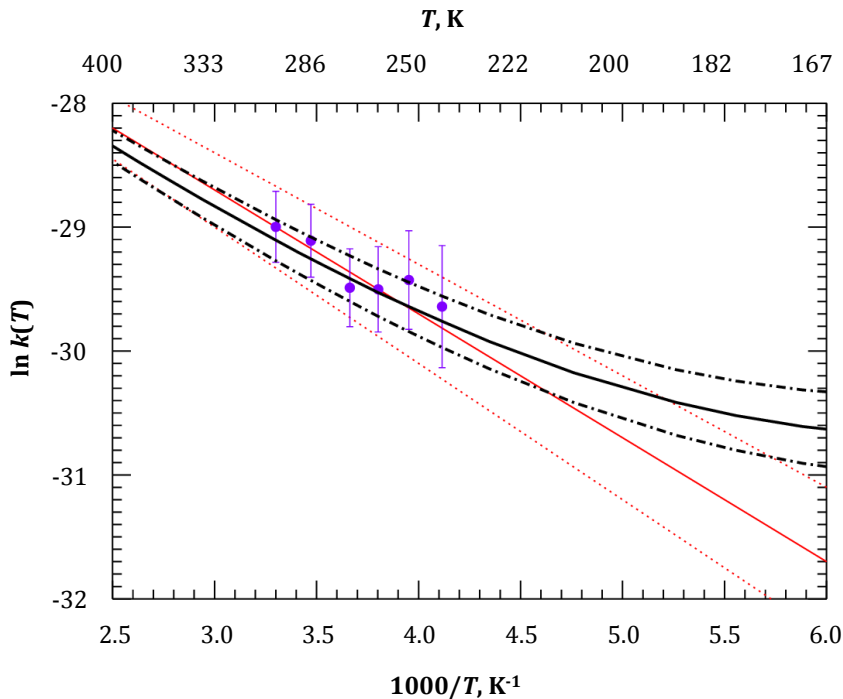
Figure 3.6   Additional SCTST calculation for sensitivity of R12 thermal rate coefficients (k_{12}, cm^3 molecule^{-1} s^{-1}) (black solid line) to k_{12} with E_b changed up and down by 0.1 kcal mol^{-1} (black dash with dot line) together with experimental $k(T)$ values from this work (purple circles) as well as IUPAC recommended values [25] (red).
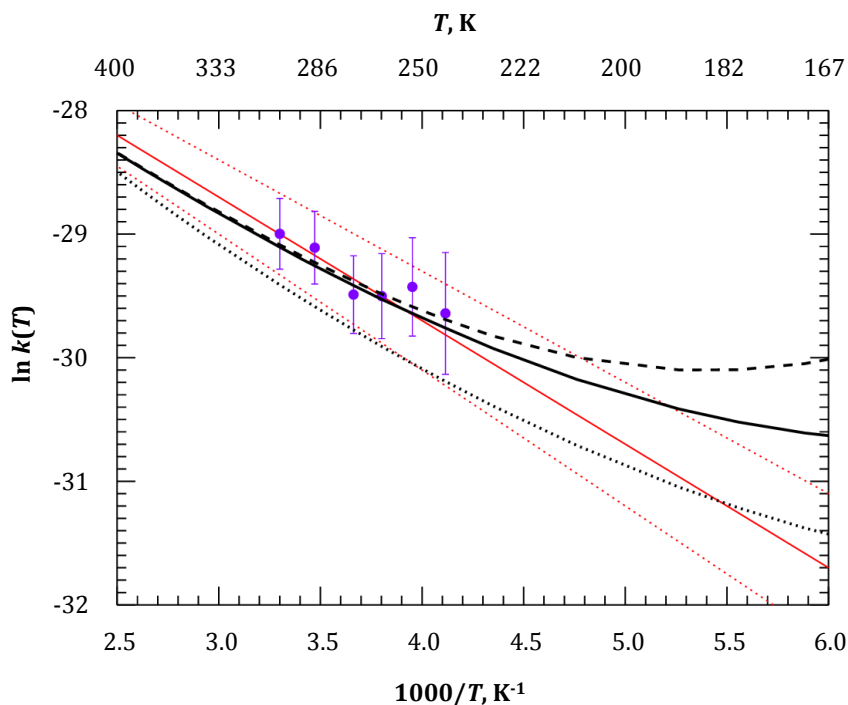
Figure 3.7   Additional SCTST calculation for sensitivity of R12 thermal rate coefficients (k_{12}, cm^3 molecule^{-1} s^{-1}) (black solid line) to k_{12} without vibrational anharmonicity (black dot line) and k_{12} with RC lowered by 1 kcal mol^{-1} (black dash line) together with experimental $k(T)$ values from this work (purple circles) as well as IUPAC recommended values [25] (red).

The temperature dependence of KIE for the reaction C_2H_6 + OH → C_2H_5 + H_2O calculated from the k_{12} and k_{13} absolute values are shown in Figure 3.8 together with experiment values of KIE from this work and reported value by Anderson et al. [16]. The calculated KIE values are additionally listed in Table 3.5.
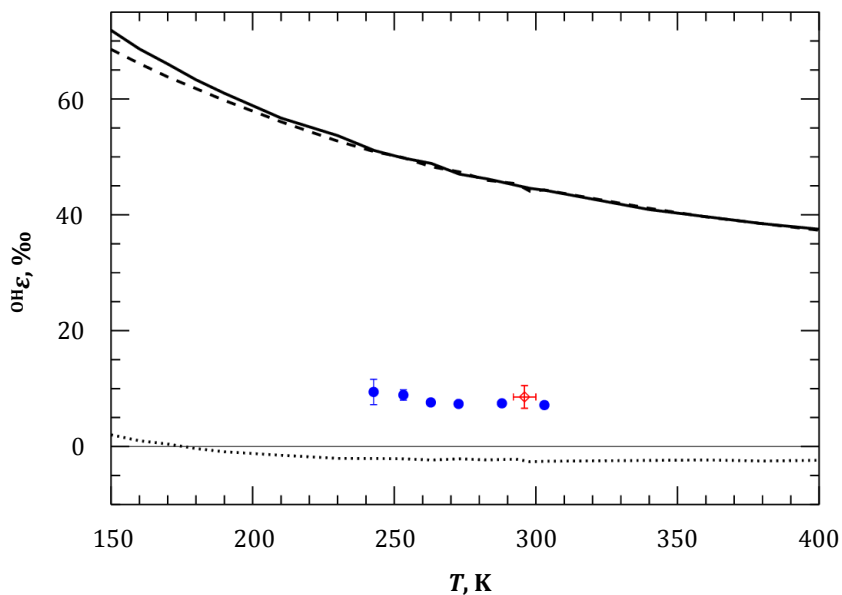
Figure 3.8 Calculated KIE values for the reaction $C_2H_6 + OH \rightarrow C_2H_5 + H_2O$ (black full line), calculated KIE values by stabilizing the RC by 1 kcal mol^{-1} (black dash line), calculated KIE values without vibrational anharmonicity (black dot line), and experimental $^{OH}\varepsilon$ values from this work (full blue circles) (For details, see Section 2.3) as well as a value reported by Anderson et al. [16] (red diamond).

Table 3.5   SCTST calculated KIE values for the reaction $C_2H_6 + OH \rightarrow C_2H_5 + H_2O$.

T(K)	$^{OH}\varepsilon$, ‰
150	71.856
160	68.641
170	66.038
180	63.313
190	60.986
210	56.708
230	53.676
243	51.091
253	49.819
263	48.878
273	47.019
283	46.187
293	45.100
298	44.562
303	44.252
340	40.903
360	39.687
380	38.471
400	37.516

The calculated KIE values using SCTST differ from experimental values by approximately a factor of six. These differences are too large to be serviceable for those small KIEs prediction. The theoretical study shows slightly negative temperature dependence of KIE for the reaction $C_2H_6 + OH \rightarrow C_2H_5 + H_2O$ which is in agreement with experimental result. Furthermore, other theoretical studies for hydrogen abstraction reactions also report the negative KIE temperature dependence for the reaction $CH_4 + OH \rightarrow CH_3 + H_2O$ by Lin et al. [35] and for the reaction $CH_4 + Cl \rightarrow CH_3 + HCl$ by Barker et al. [36].

The sensitivity of the theoretical predictions to the KIEs was investigated by calculations using variations of kinetic model relating to the previous sensitivity analysis for the rate coefficients. Altering E_b for reactants to TS by $\pm$ 0.1 kcal mol^{-1} for the calculations of k_{12} and k_{13} in the same direction does not affect the KIE values. Exclusion of anharmonic vibrational characteristic lowers the KIE values as well as the temperature dependence of KIE. Some KIE values calculated without anharmonic vibration treatment are negative at temperature higher than 180 K. Increasing the stability of RC by 1 kcal mol^{-1} results in slightly lowering KIE values, especially at lower temperatures. An analysis of other contributing factors to the KIE shows that our values are still affected by the computationally erroneous anharmonicity constants x_{ij} related to internal rotation, wagging, and their coupling. This occurs through the anharmonic ZPE corrections, specifically the factor E_0 in eq. 3.43. The induced error is estimated to be sufficient to account for the factor of 6 described above and even beyond. Unfortunately, correcting E_0 requires a custom re-implementation of its complex evaluation, and is outside the scope of the present work.

At present, the reaction $C_2H_6 + OH \rightarrow C_2H_5 + H_2O$ is the biggest system that has been studied theoretically for stable carbon KIE. Those systems dealing with methane reactions are relatively small comparing with those with ethane reactions, thus it is possible to achieve higher accuracy from very high levels of *ab initio* calculations. For ethane, in contrast, the bigger size of system disallows calculations at the same level as is possible for

methane in a tractable time frame. Additionally, the existence of C-C axis in ethane triggers the complication of calculation in term of internal rotation treatments which is necessary in KIE calculation, while having two carbon atoms leads to two slightly different TS. It is highly recommended that theoretical studies attempt higher levels of theory for the KIE of the reaction $C_2H_6 + OH \rightarrow C_2H_5 + H_2O$, to try and improve the result. At the current accuracy achieved, it is not possible to confidently conclude whether the KIE of the $C_2H_6 + OH$ reaction shows a temperature-dependence, especially as the experimental data likewise does not unequivocally show temperature dependence.

4 Implication of using observed KIE for C_2H_6 + OH for ambient stable carbon isotopic ratio interpretation

A remarkable improvement of the precision in the experimental determination of the KIE for the ethane oxidation by OH at room temperature was achieved. Secondly, a slight KIE increasing at lower temperatures was found, this trend being supported by theoretical KIE calculations. These findings will be implemented in a simple sensitivity study on isotopic fractioning during ethane atmospheric degradation. The study refers to the unique work on interpreting ethane ambient measurements by global modeling [17], which used a constant KIE value, measured at room temperature [16].

4.1 Interpretation of ambient ethane isotopic ratio observations

Ethane δ^{13}C has the potential to be used as tracer for chemical aging during atmospheric transport (see Section 1.7). Measurements of isotopic composition complementarily to concentration provide more constraints on VOC budgets and removal. Initially, major trace gases, CO_2, CH_4 and CO were used for such studies. Brenninkmeijer et al. showed from δ^{13}C measurements in the lower troposphere that in situ CH_4 oxidation plays no important role in CO formation [121]. Due to very high δ^{13}C values, they could differentiate masses originating from biomass burning showing a tropical signature (i.e. arising mostly form C4 plant combustions). Recently, due to emerging development of the isotopic measurement techniques, gases in ppt to few ppb ranges of concentration were investigated. Nara et al. found maritime propane sources for the observed air over the western North Pacific and eastern Indian Ocean [9]. In contrast, the observed ethane δ^{13}C value could be explained only by entrainment of free troposphere air. An elaborate study combining ambient concentration and isotope ratio measurements with global modelling was carried out by Stein and Rudolph [17]. Underestimation of calculated mixing ratios signalized missing ethane sources in the available inventories. For atmospheric ethane δ^{13}C

values, they mostly found fairly good agreement between the simulated and observed data. Yet, the model predictions for the coastal sites of New Zealand show a very narrow range of isotopic ratios for both southern summer and winter, being around -17 ‰ (Figure 4.1), while measurements at Baring Head, New Zealand gave a strong distinction for the two seasons with -22 and -29.7 ‰, respectively [2].
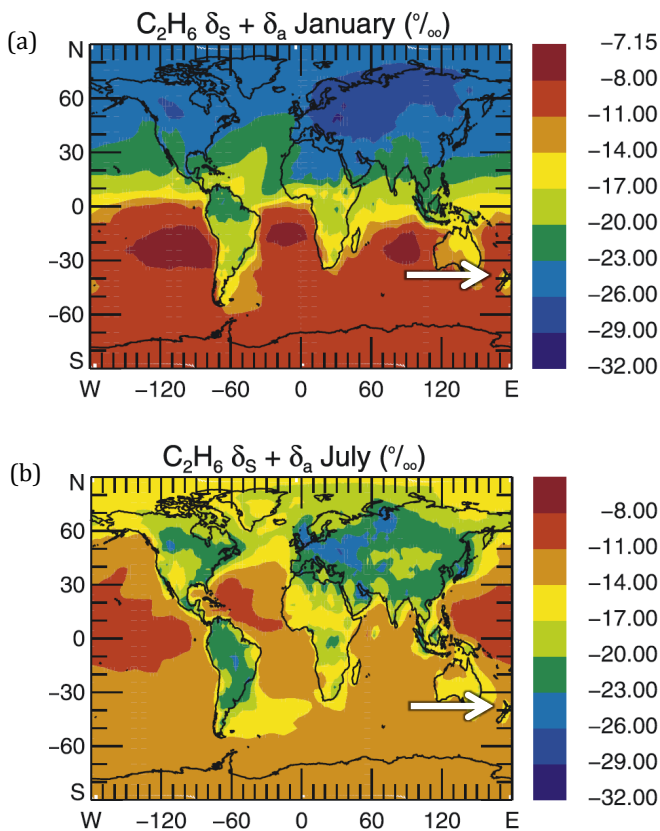
Figure 4.1 Modelled stable carbon isotope ratios of ethane ($\delta^{13}C$) in January and July 1995 (a and b, respectively) near surface calculated using MOZART-2. The area around Baring Head, New Zealand is pointed by white arrow. (Taken from Stein and Rudolph [17])

4.2　Role of the precision improvement of KIE determination

Figure 4.2 shows the ethane isotopic fractionation, i.e. the change in stable carbon isotope ratios ($\delta^{13}C_t - \delta^{13}C_0$), depending on the extent of its atmospheric processing. Two dependences and their uncertainty ranges are plotted. To determine the isotopic fractioning versus ethane chemical conversion, the KIE determined in this study, as well the value reported by Anderson et al. [16] were employed to obtain the curves (see Equation 1.22).
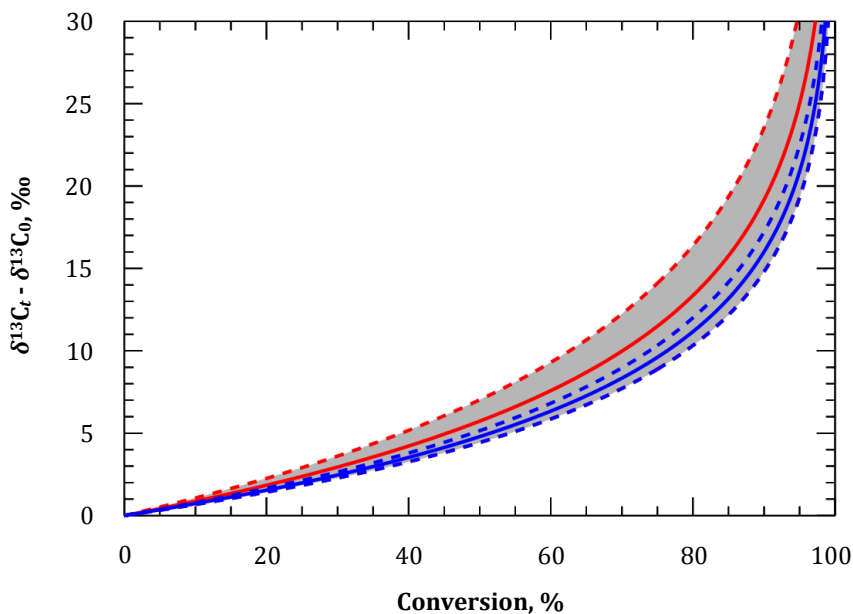
Figure 4.2　Change in stable carbon isotope ratios ($\delta^{13}C_t - \delta^{13}C_0$) with the conversion of ethane during its oxidation by OH and uncertainty ranges (full and dash lines, respectively) calculated using the KIE determined in this work at 303.0 ± 0.1 K (blue) and the one reported at 296 ± 4 K by Anderson et al. [16] (red and grey shade).

In this work, a remarkable refinement of the KIE measurement precision for the ethane oxidation by hydroxyl radicals, measured around the room temperature, was achieved, compared to a previous report [16]. Values of 7.16 ± 0.54 and 7.45 ± 0.48 ‰ at 303.0 ± 0.1 and 288.0 ± 0.2 K, respectively, were obtained in this work in comparison to 8.57 ± 1.95 ‰ at 296 ± 4 K, reported by Anderson et al. [16].

Considering a global average $\delta^{13}C$ value for ethane source of -27 ‰ [17] and the value measured at Baring Head in March 1996, i.e. -22 ‰, a pronounced chemical aging can be concluded. Figure 4.2 shows that in case of using Anderson et al. KIE value (8.57 ± 1.95 ‰), ethane chemical conversion of 0.38 to 0.54 can be derived. This translates in deviations of 62 % in calculating the time experienced from the emission to measurement, when using the lower and higher limits of conversion. In contrast, using KIE value from this work (7.16 ± 0.54 ‰) resulted in much narrower uncertainty limits of 15 % deviation which can be derived from ethane chemical conversion of 0.49 to 0.54.

4.3 Role of KIE temperature dependence

Tropospheric temperatures vary a lot by latitude, longitude and altitude, being generally much lower than the room temperature. Values down to 193 K can be reached in the upper troposphere. Thus, the KIE temperature dependence should be considered when applying the 'isotopic hydrocarbon clock' concept for interpreting ambient ethane measurements. Figure 4.3 shows the change in stable carbon isotope ratios ($\delta^{13}C_t - \delta^{13}C_0$) during the chemical oxidation of ethane by OH derived from experimental KIEs determined at highest and lowest temperatures investigated in this work: i.e. 7.16 ± 0.54 ‰ at 303.0 ± 0.1 K and 9.42 ± 2.19 ‰ at 242.7 ± 0.3 K.

It is to be seen that for older air masses containing ethane, there are significant deviations between the isotopic fractioning values calculated for room temperature or implementing the KIE temperature dependence. Exemplarily, at 90 % conversion of ethane, using the KIE value determined at 242.7 ± 0.3 K, a change in the stable carbon isotope ratio

of 21 ± 5 ‰ is derived instead of 16 ± 1 ‰ by using the KIE value determined at 303.0 ± 0.1 K. It implies that with the temperature dependence of KIE, the change in stable carbon isotope ratios can differ for 25 % for extremely processed ethane, which may lead to significantly different outcome for the ambient studies when comparing observed and computed results.
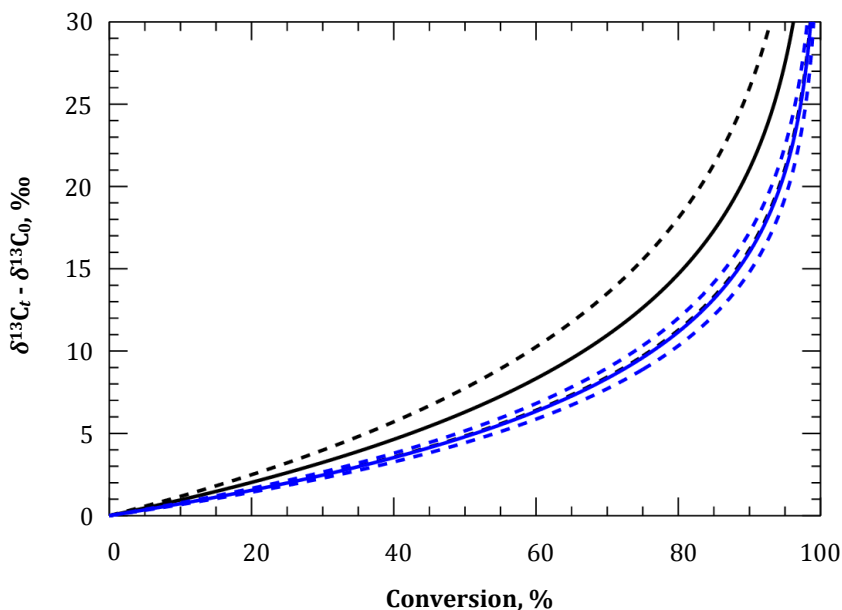
Figure 4.3   Change in stable carbon isotope ratios ($\delta^{13}C_t - \delta^{13}C_0$) with the conversion of ethane in the chemical oxidation process by OH evaluated from KIE determined in this work at 303.0 ± 0.1 K (blue lines) and at 242.7 ± 0.3 K (black lines). The uncertainty ranges are depicted by full and dot lines, respectively.

On the other hand, Figures 4.2 and 4.3 show an overlap of ethane isotopic fraction ranges during its chemical degradation obtained by implementing the KIE temperature dependence from this work and the KIE determined by Anderson et al. [16]. Therefore, it could be argued that introducing temperature dependent KIE in global modeling will not

alter the results presented by Stein and Rudolph [17]. In this study, the authors conclude that the modeled ethane δ ^{13}C of -17 ‰ in average overestimates the observed δ ^{13}C of -22 ‰ (March 1996) and -29.7 ‰ (July 1996) in the costal sites of New Zealand. They claim a reason of this disagreement by the fact that local sources were ignored. It is to be mention here that a constant and high $^{OH}\varepsilon$ of 8.59 ‰ was employed in the simulations. This might translates in too high, but similar isotopic ratios for January and July (Figure 4.1). The differentiation might be achieved, when considering local sources and the temperature dependence of ethane fractioning during its atmospheric degradation. Lighter ethane in the late winter can be due to mixing of fresh ethane (δ^{13}C = -32 ‰ [2]) originating from the natural gas fields situated 300 - 400 km north of the sampling site, Baring Head. The fresh ethane can be transported with the northerlies which are typical for this period of the year. On the contrary, the South Pole night starts in March. Very cold clean air flows over Baring Head from south-southeast [6], thus it is isolated from contact with new emissions for long time. Consequently, the highly processed ethane might experience a higher fractionation at lower temperatures, explaining the higher δ ^{13}C observed in this time of the year. Overall, the implementation of ethane KIE temperature dependence in atmospheric studies will definitively not bring a completely new isotopic global distribution, but will deliver a finer structure of it.

Here, simple considerations of the refined KIE measurement precision and the KIE temperature dependence together with the 'isotopic hydrocarbon clock' concept were made to calculate stable carbon isotopic ratios of atmospheric ethane. It was shown that both improvements obtained in the experimental work might bring a better understanding of the atmospheric processes.

5 Conclusions

The aim of this work was to examine the temperature dependence of stable carbon (^{12}C/^{13}C) KIE for the ethane oxidation by hydroxyl radicals in the tropospherically relevant temperature range. To this end, comprehensive experimental and theoretical investigations were carried out. Furthermore, a framework application for testing the observed KIE for atmospheric studies is presented.

Oxidation reactions of ethane with OH radicals were carried out in a temperature controlled reaction chamber at temperatures in the range of 243 to 303 K. Propane was added to the reaction system as a reference compound to verify the ethane oxidation chemistry. Both ethane and propane were characterized by natural isotope abundances.

Prior to isotopic measurements, following objectives were achieved to ensure high performance of the used instrumentation:

i. Developing of a temperature controlled reaction chamber and testing for the accuracy and stability of inside temperature required during the reaction;

ii. Developing and testing of appropriate experimental procedures to attain high chemical conversion of ethane, especially at low temperatures;

iii. Developing and testing of a TD-GC-C-IRMS method for accurate component specific determination of δ^{13}C values for ethane, including the pre-preparation of the samples withdrawn from the reaction chamber;

Thus, a high degree of temperature accuracy was attained, resulting in temperature standard deviations within 0.3 K. Furthermore, even at 243 K, where the OH production is strongly inhibited by the very low vapor pressure of H_2O_2, conversions of the very long lived ethane up to 82.3 % were reached within 20 hours. Component specific isotopic measurements of ethane were performed by TD-GC-C-IRMS. Reaction rate coefficients for the ethane oxidation by OH radicals in the temperature range 243-303 K were derived

from temporal evolution of ethane concentration, showing values of $(1.34 \pm 0.66) \times 10^{-13}$ cm^3 molecule^{-1} s^{-1} to $(2.55 \pm 0.73) \times 10^{-13}$ cm^3 molecule^{-1} s^{-1}, respectively. They were validated based on propane concentration measurements by employing a relative rate technique. The observed coefficients show good agreement with experimental values reported in the literature. Moreover, they are well imbedded in the range of IUPAC recommended temperature dependence.

The KIE values were derived for each tested temperature from the dependence of the ethane δ^{13}C and concentration on the reaction extent. Both KIE values for ethane oxidation by OH determined around room temperatures (288 and 303 K) show a remarkable improvement of the measurement precision compared to the only available value reported in literature, being 7.45 ± 0.48 and 7.16 ± 0.54 ‰, respectively, versus 8.57 ± 1.95 reported by Anderson et al. at 296 ± 4 K [16]. Overall, the reproducibility of $^{OH}\varepsilon$ values was approximatively 19.76 % of the average.

Over the investigated temperature range, a slight increasing tendency of KIE toward lower temperatures, being approximately 0.4 ± 0.1 ‰ per 10 K.

Theoretical KIE study was performed to provide insight in the KIE temperature dependence for a larger temperature range, including temperatures lower than 243 K, where the experimental investigations are limited. Since the ^{12}C/^{13}C KIE is very small, a highly accurate molecular description of reaction pathway is required. Therefore, the conventional kinetics method, such as conventional transition state theory, is not sufficient to be utilized for the accurate KIE determination.

Quantum mechanical calculation methodologies were selected for the ethane + OH system, to attain the optimal balance between computational resource and level of theory. The M06-2X method of density functional theory with an aug-cc-pVTZ basis set was used to calculate the geometry optimization using a benchmark-quality 99,974 DFT integration grid and very tight SCF convergence criteria were considered. It is important to include anharmonic vibrational frequencies and internal rotation treatments for stationary points

along the reaction coordinate of $C_2H_6 + \bullet OH \rightarrow \bullet C_2H_5 + H_2O$ in this calculation. High-level theory CCSD(T) using aug-cc-pVxZ (x = D,T,Q) basis sets, with extrapolation to the complete basis set limit (CBS) was further used to ontain more accurate energies. The extrapolation to CBS was achieved by using the 3-parameter expression aug-Schwartz6 (DTQ).

Semi-Classical Transition State Theory (SCTST) including vibrational anharmonicity, tunneling effect and internal rotation treatment was carried out to obtain thermal rate coefficients for three different isotopic reaction mechanisms, i.e. R12, R13a, and R13b, corresponding to pure ^{12}C ethane and ethane containing a ^{13}C either at the H abstraction site, or at the not involved one, respectively. The calculated ^{12}k and ^{13}k were employed to derive theoretical KIE values in the temperature range of 150-400 K.

The theoretically obtained rate coefficients show good agreement with experimental values from this work and other literatures, as well as with IUPAC recommended values, within error ranges. In contrast, the calculated KIE values differ from the experimental values observed here by approximately a factor of six. However, slightly negative temperature dependence of theoretical KIE supports the experimental findings.

At the best of my knowledge, the reaction $C_2H_6 + OH \rightarrow C_2H_5 + H_2O$ is the biggest chemical system that has been hitherto theoretically investigated for stable carbon KIE determination from absolute rate coefficient calculations. Yet, limited tractable time frame and computing resource determined the level of the implemented theory for the KIE prediction. At the currently achieved accuracy it is not possible to confidently describe a temperature dependence of the KIE, especially since the experimental data likewise does not unequivocally show temperature dependence. Nevertheless, this study opens the possibility for comparisons among unique theories. Additionally, higher levels of theory are suggested for further calculations i.e. geometry optimizations, anharmonicity frequencies, tunneling effect and internal rotation.

A very simple implementation of the refined experimental KIE values in investigating the isotopic fractioning of ethane during its chemical degradation in the

atmosphere shows a remarkable improvement of precision for stable carbon isotopic ratio calculations of atmospheric ethane.

For applications in the future, precise KIE data obtained in this study, together with KIE temperature dependence from experiments and quantum calculations at higher levels of theory will be implemented in global chemical transport models. The modelled results will be compared with available ethane isotopic and concentration measurements. In this way, the global ethane isotopic distribution will be better predicted and thus, its sources, transport and sinks will be better constrained.

List of Abbreviations

aug-cc-pVTZ	Augmented Dunning's correlation-consistent polarized valence triple-zeta basis set
B	Rotational constant
BHandHLYP	Becke-half-and-half-Lee, Yang, and Par correlation functionals
c	Molecular orbital expansion coefficient
C	Concentration
CBS	Complete basis set
CC	Coupled-cluster
CCN	Cloud condensation nuclei
cc-pVDZ	Dunning's correlation-consistent polarized valence with double-zeta basis set
CCSD(T)	Coupled-cluster with a full treatment of single and double excitations and a perturbative estimation of the triple excitations
CI	Configuration interaction
CIS	Cooled injection system
CISD	Configuration interaction with single and double substitution
CRP	Cumulative reaction probability
CTS	Cryogenic trapping system
DFT	Density functional theory
DTQ	3-parameter expression augmented Schwartz6

E	Energy
E_a	Activation energy
EA	Elemental analysis
E_b	Barrier Height
EPC	Electronic pneumatic control
E_r	Relative energy
E_v	Vibrational energy
Exp.	Experiment
FCI	Full configuration interaction
FEP	Fluorinated ethylene propylene
FID	Flame ionize
GC	Gas chromatograph or gas chromatography
GGA	Meta-generalized Gradient Approximations
g	Electronic state degeneracy
g_p	Gaussian-type atomic function
h	Planck's constant
HF	Hartree-Fock
hr	Hindered internal rotor, -rotation, -rotational
I	Moment of inertia
ID	Inside diameter
IRMS	Isotope ratio mass spectrometry
IUPAC	International Union of Pure and Applied Chemistry

KIE	Kinetic isotope effect
J	Repulsion
k, k(T)	Rate coefficient
k_B	Boltzmann's constant
L	Length
LDA	Local density approximation
LN_2	Liquid nitrogen
LV-WSOC	Low-volatile water-soluble organic aerosol
LYP	Lee, Yang, and Par correlation functionals
m	mass
M06-2X	Minnesota 06 global hybrid functional with 54 % HF exchange
MEP	Minimum energy path
MP	Møller-Plesset perturbation
MS	Mass spectrometry
MSD	Mass spectrometric detector
N_C	Carbon number
o	Number of optical isomer
OD	Outside diameter
OVOC	Oxygenated volatile organic compound
P	Pressure
PAN	Peroxyacetyl nitrate
PC	Product complex

PES	Potential energy surface
P_n	Semi-classical tunneling probability
q	Charge
Q	Partition function
QCI	Quadratic configuration interaction
r	distance
RC	Reactant complex
RT	Retention time
SCF	Self-consistent field
SCTST	Semi-classical transition state theory
SL	Sample loop
SRR	Structure-reactivity relationship
t	Time
T	Temperature
TD	Thermal desorption
TDSL	Thermo Desorption System Large
TS	Transition state
TSQN	Synchronous Transit Quasi-Newton
TST	Transition state theory
UV	Ultraviolet
V	Potential energy
VOC	Volatile organic compound

Vol	Volume
VPDB	Vienna Peedee belemnite
VTP2	Second-order vibrational perturbation theory
WS	Working standard
x	Vibrational anharmonicity constant
XC	Exchange-correlation
ZPE	Zero-point energy

List of Figures

List of Tables

References

1. Finlayson-Pitts, B.J. and J.N. Pitts, *Chapter 4 - Photochemistry of Important Atmospheric Species*, in *Chemistry of the Upper and Lower Atmosphere*, 2000, Academic Press: San Diego. 86-129.

2. Rudolph, J., et al., *A novel method for compound specific determination of $\delta^{13}C$ in volatile organic compounds at ppt levels in ambient air.* Geophysical Research Letters, 1997. **24**(6): 659-662.

3. Rudolph, J. and E. Czuba, *On the use of isotopic composition measurements of volatile organic compounds to determine the "photochemical age" of an air mass.* Geophysical Research Letters, 2000. **27**(23): 3865-3868.

4. Rudolph, J., E. Czuba, and L. Huang, *The stable carbon isotope fractionation for reactions of selected hydrocarbons with OH-radicals and its relevance for atmospheric chemistry.* Journal of Geophysical Research: Atmospheres, 2000. **105**(D24): 29329-29346.

5. Goldstein, A.H. and S.L. Shaw, *Isotopes of Volatile Organic Compounds: An Emerging Approach for Studying Atmospheric Budgets and Chemistry.* Chemical Reviews, 2003. **103**(12): 5025-5048.

6. Rudolph, J., *Gas Chromatography–Isotope Ratio Mass Spectrometry*, in *Volatile Organic Compounds in the Atmosphere*, ed. by R. Koppmann, 2007, Blackwell Publishing Ltd.: Oxford. 388-466.

7. Brenninkmeijer, C.A.M., *Applications of stable isotope analysis to atmospheric trace gas budgets.* EPJ Web of Conferences, 2009. **1**: 137-148.

8. Wintel, J., et al., *Stable carbon isotope ratios of toluene in the boundary layer and the lower free troposphere.* Atmos. Chem. Phys., 2013. **13**(21): 11059-11071.

9. Nara, H., S. Toyoda, and N. Yoshida, *Measurements of stable carbon isotopic composition of ethane and propane over the western North Pacific and eastern Indian Ocean: A useful indicator of atmospheric transport process.* Journal of Atmospheric Chemistry, 2007. **56**(3): 293-314.

10. Saito, T., et al., *Stable carbon isotopic compositions of light hydrocarbons over the western North Pacific and implication for their photochemical ages.* Journal of Geophysical Research: Atmospheres, 2002. **107**(D4): ACH 2-1-ACH 2-9.

11. Saito, T., et al., *Photochemical histories of nonmethane hydrocarbons inferred from their stable carbon isotope ratio measurements over east Asia.* Journal of Geophysical Research: Atmospheres, 2009. **114**(D11).

12. Saito, T., et al., *Stable carbon isotope ratios of ethane over the North Pacific: Atmospheric measurements and global chemical transport modeling.* Journal of Geophysical Research: Atmospheres, 2011. **116**(D2).

13. Rudolph, J., *The tropospheric distribution and budget of ethane.* Journal of Geophysical Research: Atmospheres, 1995. **100**(D6): 11369-11381.

14. Tsunogai, U., N. Yoshida, and T. Gamo, *Carbon isotopic compositions of C2-C5 hydrocarbons and methyl chloride in urban, coastal, and maritime atmospheres over the western North Pacific.* Journal of Geophysical Research: Atmospheres, 1999. **104**(D13): 16033-16039.

15. Rudolph, J., et al., *Stable carbon isotope composition of nonmethane hydrocarbons in emissions from transportation related sources and atmospheric observations in an urban atmosphere.* Atmospheric Environment, 2002. **36**(7): 1173-1181.

16. Anderson, R.S., et al., *Carbon Kinetic Isotope Effects in the Gas Phase Reactions of Light Alkanes and Ethene with the OH Radical at 296 ± 4 K.* J. Phys. Chem. A, 2004. **108**: 11537-11544.

17. Stein, O. and J. Rudolph, *Modeling and interpretation of stable carbon isotope ratios of ethane in global chemical transport models.* Journal of Geophysical Research: Atmospheres, 2007. **112**(D14): D14308.

18. Simpson, I.J., et al., *Long-term decline of global atmospheric ethane concentrations and implications for methane.* Nature, 2012. **488**(7412): 490-494.

19. Schultz, M.G., et al., *The Global Atmosphere Watch reactive gases measurement network.* Elementa: Science of the Anthropocene, 2015. **3**: 67.

20. Pozzer, A., et al., *Observed and simulated global distribution and budget of atmospheric C2-C5 alkanes.* Atmos. Chem. Phys., 2010. **10**(9): 4403-4422.

21. Xiao, Y., et al., *Global budget of ethane and regional constraints on U.S. sources.* Journal of Geophysical Research: Atmospheres, 2008. **113**(D21): D21306.

22. Etiope, G. and P. Ciccioli, *Earth's Degassing: A Missing Ethane and Propane Source.* Science, 2009. **323**(5913): 478.

23. Atkinson, R., *Atmospheric chemistry of VOCs and NOx.* Atmospheric Environment, 2000. **34**(12–14): 2063-2101.

24. Möller, D., *Chemistry of the Climate System*, 2014, Walter de Gruyter: Berlin.

25. Atkinson, R., et al., *Evaluated kinetic and photochemical data for atmospheric chemistry: Volume II - gas phase reactions of organic species.* Atmos. Chem. Phys., 2006. **6**(11): 3625-4055.

26. Spicer, C.W., et al., *Unexpectedly high concentrations of molecular chlorine in coastal air.* Nature, 1998. **394**(6691): 353-356.

27. Gupta, M.L., et al., *Global atmospheric distributions and source strengths of light hydrocarbons and tetrachloroethene.* Journal of Geophysical Research: Atmospheres, 1998. **103**(D21): 28219-28235.

28.   H. Ehhalt, D., *Photooxidation of trace gases in the troposphere Plenary Lecture.* Physical Chemistry Chemical Physics, 1999. **1**(24): 5401-5408.

29.   Finlayson-Pitts, B.J. and J.N. Pitts Jr., *Chapter 5 - Kinetics and Atmospheric Chemistry*, in *Chemistry of the Upper and Lower Atmosphere*, 2000, Academic Press: San Diego. 130-178.

30.   Finlayson-Pitts, B.J. and J.N. Pitts Jr., *Fundamentals and Experimental Techniques*, in *Atmospheric Chemistry*1986, Wiley-VCH Verlag GmbH & Co. KGaA, Weinheim. 1244-1244.

31.   Craig, H., *Isotopic standards for carbon and oxygen and correction factors for mass-spectrometric analysis of carbon dioxide.* Geochimica et Cosmochimica Acta, 1957. **12**(1–2): 133-149.

32.   Coplen Tyler, B., *Reporting of stable hydrogen, carbon, and oxygen isotopic abundances (Technical Report)*, in *Pure and Applied Chemistry,* 1994. **66**(2): 273.

33.   Gensch, I., et al., *Temperature dependence of the kinetic isotope effect in β-pinene ozonolysis.* Journal of Geophysical Research: Atmospheres, 2011. **116**(D20): D20301/1-D20301/10.

34.   Gensch, I., A. Kiendler-Scharr, and J. Rudolph, *Isotope ratio studies of atmospheric organic compounds: Principles, methods, applications and potential.* International Journal of Mass Spectrometry, 2014. **365–366**: 206-221.

35.   Lin, H., et al., *Temperature Dependence of Carbon-13 Kinetic Isotope Effects of Importance to Global Climate Change.* Journal of the American Chemical Society, 2005. **127**(9): 2830-2831.

36.   Barker, J.R., T.L. Nguyen, and J.F. Stanton, *Kinetic Isotope Effects for Cl + CH₄ → HCl + CH₃ Calculated Using ab Initio Semiclassical Transition State Theory.* The Journal of Physical Chemistry A, 2012. **116**(24): 6408-6419.

37.   Cantrell, C.A., et al., *Carbon kinetic isotope effect in the oxidation of methane by the hydroxyl radical.* Journal of Geophysical Research: Atmospheres, 1990. **95**(D13): 22455-22462.

38.   Rudolph, J. and F.J. Johnen, *Measurements of light atmospheric hydrocarbons over the Atlantic in regions of low biological activity.* Journal of Geophysical Research: Atmospheres, 1990. **95**(D12): 20583-20591.

39.   Irei, S., et al., *Transboundary Secondary Organic Aerosol in Western Japan Indicated by the δ13C of Water-Soluble Organic Carbon and the m/z 44 Signal in Organic Aerosol Mass Spectra.* Environmental Science & Technology, 2014. **48**(11): 6273-6281.

40.   Anderson, R.S., et al., *Method for Measuring Carbon Kinetic Isotope Effects of Gas-Phase Reactions of Light Hydrocarbons with the Hydroxyl Radical.* J. Phys. Chem. A, 2003. **107**: 6191-6199.

41.   Goldstein, S., et al., *Photolysis of Aqueous H_2O_2: Quantum Yield and Applications for Polychromatic UV Actinometry in Photoreactors.* Environ. Sci. Technol., 2007. **41**: 7486-7490.

42.   Iannone, R., R. Koppmann, and J. Rudolph, *The stable-carbon kinetic isotope effects of the reactions of isoprene, methacrolein, and methyl vinyl ketone with ozone in the gas phase.* Atmos. Environ., 2008. **42**: 8728-8737.

43.   Merritt, D.A., et al., *Performance and Optimization of a Combustion Interface for Isotope Ratio Monitoring Gas Chromatography/Mass Spectrometry.* Analytical Chemistry, 1995. **67**(14): 2461-2473.

44.   Brand, W.A., S.S. Assonov, and T.B. Coplen, *Correction for the ^{17}O interference in $δ(^{13}C)$ measurements when analyzing CO_2 with stable isotope mass spectrometry (IUPAC Technical Report).* Pure and Applied Chemistry, 2010. **82**(8): 1719-1733.

45.   Rosman, K.J.R. and P.D.P. Taylor, *Isotopic compositions of the elements 1997 (Technical Report).* Pure and Applied Chemistry, 1998. **70**(1): 217-235.

46.   Clarke, J.S., et al., *Testing Frontier Orbital Control: Kinetics of OH with Ethane, Propane, and Cyclopropane from 180 to 360 K.* The Journal of Physical Chemistry A, 1998. **102**(48): 9847-9857.

47.   Talukdar, R.K., et al., *Kinetics of the reactions of OH with alkanes.* International Journal of Chemical Kinetics, 1994. **26**(10): 973-990.

48.   Margitan, J.J. and R.T. Watson, *Kinetics of the reaction of hydroxyl radicals with nitric acid.* The Journal of Physical Chemistry, 1982. **86**(19): 3819-3824.

49.   Zabarnick, S., J.W. Fleming, and M.C. Lin, *Kinetics of hydroxyl radical reactions with formaldehyde and 1,3,5-trioxane between 290 and 600 K.* International Journal of Chemical Kinetics, 1988. **20**(2): 117-129.

50.   Sharkey, P. and I.W.M. Smith, *Kinetics of elementary reactions at low temperatures: rate constants for the reactions of OH with HCl ($298 \geq T/K \geq 138$), CH_4 ($298 \geq T/K \geq 178$) and C_2H_6 ($298 \geq T/K \geq 138$).* Journal of the Chemical Society, Faraday Transactions, 1993. **89**(4): 631-637.

51.   Donahue, N.M., J.G. Anderson, and K.L. Demerjian, *New Rate Constants for Ten OH Alkane Reactions from 300 to 400 K: An Assessment of Accuracy.* The Journal of Physical Chemistry A, 1998. **102**(18): 3121-3126.

52.   Stachnik, R.A., L.T. Molina, and M.J. Molina, *Pressure and temperature dependences of the reaction of hydroxyl radical with nitric acid.* The Journal of Physical Chemistry, 1986. **90**(12): 2777-2780.

53.   *PubChem Compound Database; CID=784*, National Center for Biotechnology Information.

54. Bravo-Pérez, G., et al., *Quantum chemical and conventional TST calculations of rate constants for the OH + alkane reaction.* Chemical Physics, 2005. **310**(1–3): 213-223.

55. Huynh, L.K., A. Ratkiewicz, and T.N. Truong, *Kinetics of the Hydrogen Abstraction OH + Alkane → H_2O + Alkyl Reaction Class: An Application of the Reaction Class Transition State Theory.* The Journal of Physical Chemistry A, 2006. **110**(2): 473-484.

56. Yan, T., W.L. Hase, and C. Doubleday, *Energetics, transition states, and intrinsic reaction coordinates for reactions associated with $O(^3P)$ processing of hydrocarbon materials.* The Journal of Chemical Physics, 2004. **120**(19): 9253-9265.

57. Hashimoto, T. and S. Iwata, *Theoretical Study on the Weakly-Bound Complexes in the Reactions of Hydroxyl Radical with Saturated Hydrocarbons (Methane, Ethane, and Propane).* The Journal of Physical Chemistry A, 2002. **106**(11): 2652-2658.

58. Martell, J.M., et al., *Properties of Transition Species in the Reaction of Hydroxyl with Ethane from ab Initio Calculations and Fits to Experimental Data.* The Journal of Physical Chemistry, 1995. **99**(21): 8661-8668.

59. Aliagas, I. and S. Gronert, *Accuracy of G2 Calculations for the Reactions of Hydroxyl Radicals with Alkanes.* The Journal of Physical Chemistry A, 1998. **102**(15): 2609-2612.

60. Sekušak, S., et al., *Reaction-Path Dynamics of Hydroxyl Radical Reactions with Ethane and Haloethanes.* The Journal of Physical Chemistry A, 1997. **101**(23): 4245-4253.

61. Harmony, M.D., *The equilibrium carbon–carbon single-bond length in ethane.* The Journal of Chemical Physics, 1990. **93**(10): 7522-7523.

62. Benedict, W.S., N. Gailar, and E.K. Plyler, *Rotation-Vibration Spectra of Deuterated Water Vapor.* The Journal of Chemical Physics, 1956. **24**(6): 1139-1165.

63. Huber, K., *IV. Constants of Diatomic Molecules.* Molecular Spectra and Molecular Structure, 1979, Springer US: New York. 716.

64. Herzberg, G. and J.W.T. Spinks, *Electronic spectra and electronic structure of polyatomic molecules, Molecular Spectra and Molecular Structure Vol. 3,* 1966, Prentice Hall Inc.: London. 120-160

65. Hoy, A.R. and P.R. Bunker, *A precise solution of the rotation bending Schrödinger equation for a triatomic molecule with application to the water molecule.* Journal of Molecular Spectroscopy, 1979. **74**(1): 1-8.

66. Foresman, J.B. and Æ. Frisch, *Exploring chemistry with electronic structure methods,* 1996, Gaussian Inc.: Pittsburgh.

67. Dunning, T.H., *Gaussian basis sets for use in correlated molecular calculations. I. The atoms boron through neon and hydrogen.* The Journal of Chemical Physics, 1989. **90**(2): 1007-1023.

68. Kendall, R.A., T.H. Dunning, and R.J. Harrison, *Electron affinities of the first-row atoms revisited. Systematic basis sets and wave functions.* The Journal of Chemical Physics, 1992. **96**(9): 6796-6806.

69. Woon, D.E. and T.H. Dunning, *Gaussian basis sets for use in correlated molecular calculations. III. The atoms aluminum through argon.* The Journal of Chemical Physics, 1993. **98**(2): 1358-1371.

70. Peterson, K.A., D.E. Woon, and T.H. Dunning, *Benchmark calculations with correlated molecular wave functions. IV. The classical barrier height of the $H+H_2 \rightarrow H_2+H$ reaction.* The Journal of Chemical Physics, 1994. **100**(10): 7410-7415.

71. Davidson, E.R., *Comment on "Comment on Dunning's correlation-consistent basis sets".* Chemical Physics Letters, 1996. **260**(3–4): 514-518.

72. Li, Q.S., Q. Zhao, and S. Zhang, *An Integrated Molecular Orbital + Molecular Orbital (IMOMO) Study of the O + H–R → OH + R• Reaction Class.* The Journal of Physical Chemistry A, 2004. **108**(30): 6430-6436.

73. Li, Q.S., Y. Zhang, and S. Zhang, *Dual Level Direct ab Initio and Density-Functional Theory Dynamics Study on the Unimolecular Decomposition of CH_3OCH_2 Radical.* The Journal of Physical Chemistry A, 2004. **108**(11): 2014-2019.

74. Nguyen, H.M.T., et al., *Direct ab initio dynamics studies of the reactions of HNO with H and OH radicals.* Chemical Physics Letters, 2004. **388**(1-3): 94-99.

75. Ryzhkov, A., et al., *Theoretical and experimental studies of the gas-phase Cl-atom initiated reactions of benzene and toluene.* Adv. Quantum Chem., 2008. **55**: 275-295.

76. Bankiewicz, B., et al., *Kinetics of 1,4-Hydrogen Migration in the Alkyl Radical Reaction Class.* The Journal of Physical Chemistry A, 2009. **113**(8): 1564-1573.

77. Huynh, L.K., M. Tirtowidjojo, and T.N. Truong, *Theoretical study on kinetics of the $H_2CO + O2 → HCO + HO_2$ reaction.* Chemical Physics Letters, 2009. **469**(1-3): 81-84.

78. Li, Q.S., J. Yang, and S. Zhang, *Reaction-Path Dynamics and Theoretical Rate Constants for the $CH_nF_{4-n} + O_3 → HOOO + CH_{n-1}F_{4-n}$ (n = 2,3) Reactions.* The Journal of Physical Chemistry A, 2006. **110**(38): 11113-11119.

79. Takahashi, K., O. Yamamoto, and T. Inomata, *Direct measurements of the rate coefficients for the reactions of some hydrocarbons with chlorine atoms at high temperatures.* Proc. Combust. Inst., 2002. **29**: 2447-2453.

80. Johnson, M.A. and T.N. Truong, *High-Level ab Initio and Density Functional Theory Evaluation of Combustion Reaction Energetics: NO_2 and HONO Elimination from Dimethylnitramine.* The Journal of Physical Chemistry A, 1992. **103**(44): 8840-8846.

81. Bartlett, R.J. and G.D. Purvis, *Many-body perturbation theory, coupled-pair many-electron theory, and the importance of quadruple excitations for the correlation problem.* International Journal of Quantum Chemistry, 1978. **14**(5): 561-581.

82. Pople, J.A., et al., *Electron correlation theories and their application to the study of simple reaction potential surfaces.* International Journal of Quantum Chemistry, 1978. **14**(5): 545-560.

83. Pople, J.A., M. Head-Gordon, and K. Raghavachari, *Quadratic configuration interaction. A general technique for determining electron correlation energies.* The Journal of Chemical Physics, 1987. **87**(10): 5968-5975.

84. Purvis, G.D. and R.J. Bartlett, *A full coupled-cluster singles and doubles model: The inclusion of disconnected triples.* The Journal of Chemical Physics, 1982. **76**(4): 1910-1918.

85. Cohen, A.J., P. Mori-Sánchez, and W. Yang, *Challenges for Density Functional Theory.* Chemical Reviews, 2012. **112**(1): 289-320.

86. Zhao, Y. and D. Truhlar, *The M06 suite of density functionals for main group thermochemistry, thermochemical kinetics, noncovalent interactions, excited states, and transition elements: two new functionals and systematic testing of four M06-class functionals and 12 other functionals.* Theoretical Chemistry Accounts, 2008. **120**(1-3): 215-241.

87. Kohn, W. and L.J. Sham, *Self-Consistent Equations Including Exchange and Correlation Effects.* Physical Review, 1965. **140**(4A): A1133-A1138.

88. Zhao, Y., N.E. Schultz, and D.G. Truhlar, *Design of Density Functionals by Combining the Method of Constraint Satisfaction with Parametrization for Thermochemistry, Thermochemical Kinetics, and Noncovalent Interactions.* Journal of Chemical Theory and Computation, 2006. **2**(2): 364-382.

89. Perdew, J.P., K. Burke, and M. Ernzerhof, *Generalized Gradient Approximation Made Simple.* Physical Review Letters, 1996. **77**(18): 3865-3868.

90. Hohenstein, E.G., S.T. Chill, and C.D. Sherrill, *Assessment of the Performance of the M05–2X and M06–2X Exchange-Correlation Functionals for Noncovalent Interactions in Biomolecules.* Journal of Chemical Theory and Computation, 2008. **4**(12): 1996-2000.

91. Riley, K.E., et al., *Stabilization and Structure Calculations for Noncovalent Interactions in Extended Molecular Systems Based on Wave Function and Density Functional Theories.* Chemical Reviews, 2010. **110**(9): 5023-5063.

92. Becke, A.D., *A new mixing of Hartree–Fock and local density-functional theories.* The Journal of Chemical Physics, 1993. **98**(2): 1372-1377.

93. Lee, C., W. Yang, and R.G. Parr, *Development of the Colle-Salvetti correlation-energy formula into a functional of the electron density.* Physical Review B, 1988. **37**(2): 785-789.

94. Miehlich, B., et al., *Results obtained with the correlation energy density functionals of becke and Lee, Yang and Parr.* Chemical Physics Letters, 1989. **157**(3): 200-206.

95. Atkins, P. and J. Paula., *Atkin's Physical Chemistry*. 10th ed., 2014, Oxford Press University: Oxford.

96. McQuarrie, D. and J. Simon, in *Physical Chemistry: A Molecular Approach,* 1997, University Science Books: Sausalito, CA. 1165-1168.

97. Truhlar, D.G. and B.C. Garrett, *Variational Transition State Theory.* Ann. Rev. Phys. Chem., 1984. **35**: 159-189.

98. Truhlar, D.G., B.C. Garrett, and S.J. Klippenstein, *Current Status of Transition-State Theory.* The Journal of Physical Chemistry, 1996. **100**(31): 12771-12800.

99.   Gasser, R. and W. Richards, *An Introduction to Statistical Thermodynamics*, 1995, World Scientific: New Jersey. 33-46.

100.   Ellingson, B.A., et al., *Statistical thermodynamics of bond torsional modes: Tests of separable, almost-separable, and improved Pitzer–Gwinn approximations.* The Journal of Chemical Physics, 2006. **125**(8): 84305.

101.   Miller, W.H., *Semiclassical limit of quantum mechanical transition state theory for nonseparable systems.* The Journal of Chemical Physics, 1975. **62**(5): 1899-1906.

102.   Miller, W.H., *Semi-classical theory for non-separable systems:. Construction of "good" action-angle variables for reaction rate constants.* Faraday Discussions of the Chemical Society, 1977. **62**(0): 40-46.

103.   Miller, W.H., et al., *Ab initio calculation of anharmonic constants for a transition state, with application to semiclassical transition state tunneling probabilities.* Chemical Physics Letters, 1990. **172**(1): 62-68.

104.   Cohen, M.J., et al., *Cumulative reaction probabilities for $H+H_2 \rightarrow H_2+H$ from a knowledge of the anharmonic force field.* Chemical Physics Letters, 1992. **192**(4): 407-416.

105.   Hernandez, R. and W.H. Miller, *Semiclassical transition state theory. A new perspective.* Chemical Physics Letters, 1993. **214**(2): 129-136.

106.   Nguyen, T.L., J.F. Stanton, and J.R. Barker, *A practical implementation of semi-classical transition state theory for polyatomics.* Chemical Physics Letters, 2010. **499**(1–3): 9-15.

107.   Nguyen, T.L., J.F. Stanton, and J.R. Barker, *Ab Initio Reaction Rate Constants Computed Using Semiclassical Transition-State Theory: $HO + H_2 \rightarrow H_2O + H$ and Isotopologues.* The Journal of Physical Chemistry A, 2011. **115**(20): 5118-5126.

108. Frisch, M.J., et al., *Gaussian 09*, 2009, Gaussian, Inc.: Wallingford, CT, USA.

109. Barker, J.R., *Multiple-Well, multiple-path unimolecular reaction systems. I. MultiWell computer program suite.* International Journal of Chemical Kinetics, 2001. **33**(4): 232-245.

110. Barker, J.R., *Energy transfer in master equation simulations: A new approach.* International Journal of Chemical Kinetics, 2009. **41**(12): 748-763.

111. Li, X. and M.J. Frisch, *Energy-Represented Direct Inversion in the Iterative Subspace within a Hybrid Geometry Optimization Method.* Journal of Chemical Theory and Computation, 2006. **2**(3): 835-839.

112. Peng, C., et al., *Using redundant internal coordinates to optimize equilibrium geometries and transition states.* Journal of Computational Chemistry, 1996. **17**(1): 49-56.

113. Pulay, and G. Fogarasi, *Geometry optimization in redundant internal coordinates.* The Journal of Chemical Physics, 1992. **96**(4): 2856-2860.

114. Peng, C. and H. Bernhard Schlegel, *Combining Synchronous Transit and Quasi-Newton Methods to Find Transition States.* Israel Journal of Chemistry, 1993. **33**(4): 449-454.

115. Alecu, I.M., et al., *Computational Thermochemistry: Scale Factor Databases and Scale Factors for Vibrational Frequencies Obtained from Electronic Model Chemistries.* Journal of Chemical Theory and Computation, 2010. **6**(9): 2872-2887.

116. Martin, J.M.L., *Calibration Study of Atomization Energies of Small Polyatomics*, in *Computational Thermochemistry*1998, American Chemical Society. 212-236.

117. Wang, F. and D.P. Landau, *Efficient, Multiple-Range Random Walk Algorithm to Calculate the Density of States.* Physical Review Letters, 2001. **86**(10): 2050-2053.

118.   Basire, M., P. Parneix, and F. Calvo, *Quantum anharmonic densities of states using the Wang–Landau method.* The Journal of Chemical Physics, 2008. **129**(8): 081101.

119.   Nguyen, T.L. and J.R. Barker, *Sums and Densities of Fully Coupled Anharmonic Vibrational States: A Comparison of Three Practical Methods.* The Journal of Physical Chemistry A, 2010. **114**(10): 3718-3730.

120.   Johnson III, R.D. *NIST Computational Chemistry Comparison and Benchmark Database, NIST Standard Reference Database Number 101, Release 16a*. 2013; Available from: http://cccbdb.nist.gov/.

121.   Brenninkmeijer, C.A.M., et al., *The ^{13}C, ^{14}C, and ^{18}O isotopic composition of CO, CH_4, and CO_2 in the higher southern latitudes lower stratosphere.* Journal of Geophysical Research: Atmospheres, 1995. **100**(D12): 26163-26172.

Appendices

A.1   Examples for chromatograms

A.1.1 Blank concentration measurement

Blank concentration measurement was performed to test the cleanliness of reaction chamber before carrying on the KIE experiments. The blank concentration measurements employed the similar TD-GC-C-IRMS setup and method with those for KIE experiments (described in Section 2.1.2), after the reaction bags had been cleaned. Examples of the chromatograms obtained during the blank concentration measurements using different detectors and software are displayed in Figure A.1 and Figure A.2.
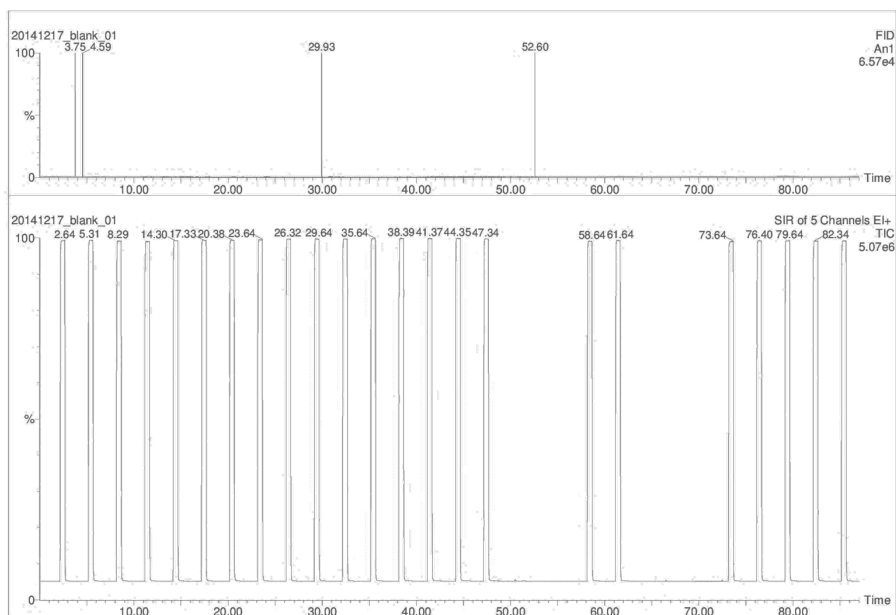
Figure A.1   Blank concentration chromatograms reported by MassLynx Inorganic using the FID (top panel) and IRMS (bottom panel) signals.
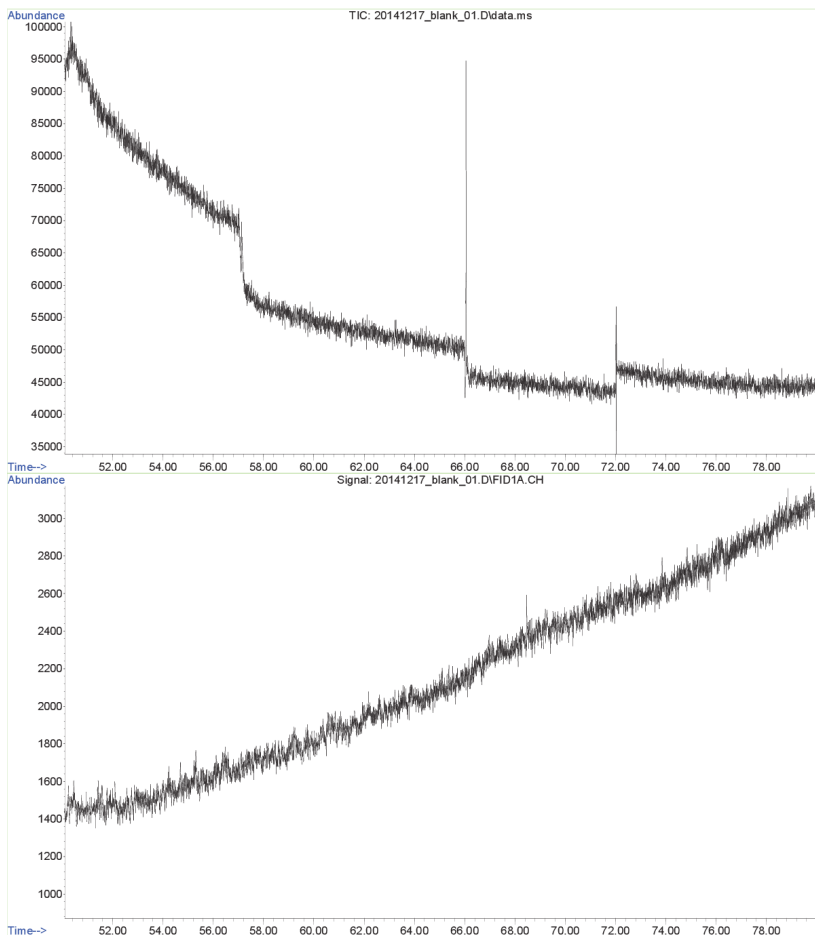
Figure A.2   Blank concentration chromatograms reported by ChemStation using the MSD (top panel) and FID (bottom panel) signals.

Figure A.1 and Figure A.2 show that the reaction chamber is free from the studied trace gases, ethane and propane. The electronic signals appearing on the FID and MSD chromatograms as well as the steep baseline on FID are on a very low level (~1000 times lower than those for ethane/propane) and they might be explained by the temperature program.

A.1.2 Example chromatograms from FID, MSD and IRMS

This section includes examples of chromatograms for ethane and propane measurements. Figures A.3 and A.4 show data from one measurement reported by different software and different detectors. The MSD spectra of the compounds eluting at RT = 43.27 min and RT = 56.97 min, corresponding to ethane and propane, respectively; are depicted in Figure A.5. All chromatograms shown in this section correspond to the second measurement of the quality control experiments at 253.2 ± 0.3 K. As shown, the peaks are base-line separated, indicating an optimal gas-chromatographic method. FID does not show ethane and propane peaks because they were completely transfered into MSD and IRMS.
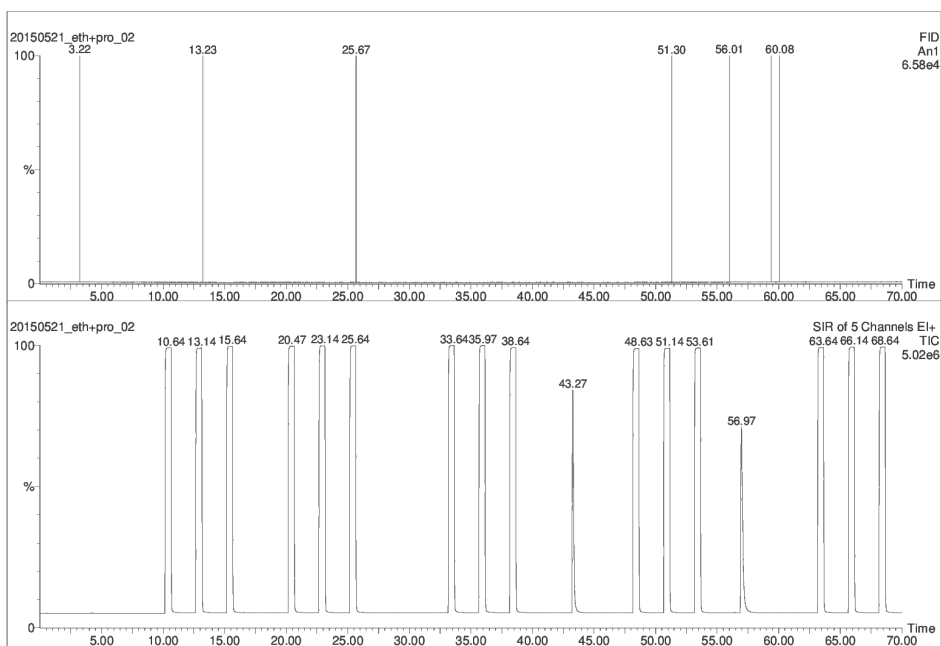
Figure A.3 Chromatograms reported during a KIE experiment by MassLynx Inorganic with FID (top panel) and IRMS (bottom panel) detectors. The peaks at RT = 43.27 min and RT = 56.97 min (top panel) correspond to ethane and propane, respectively.
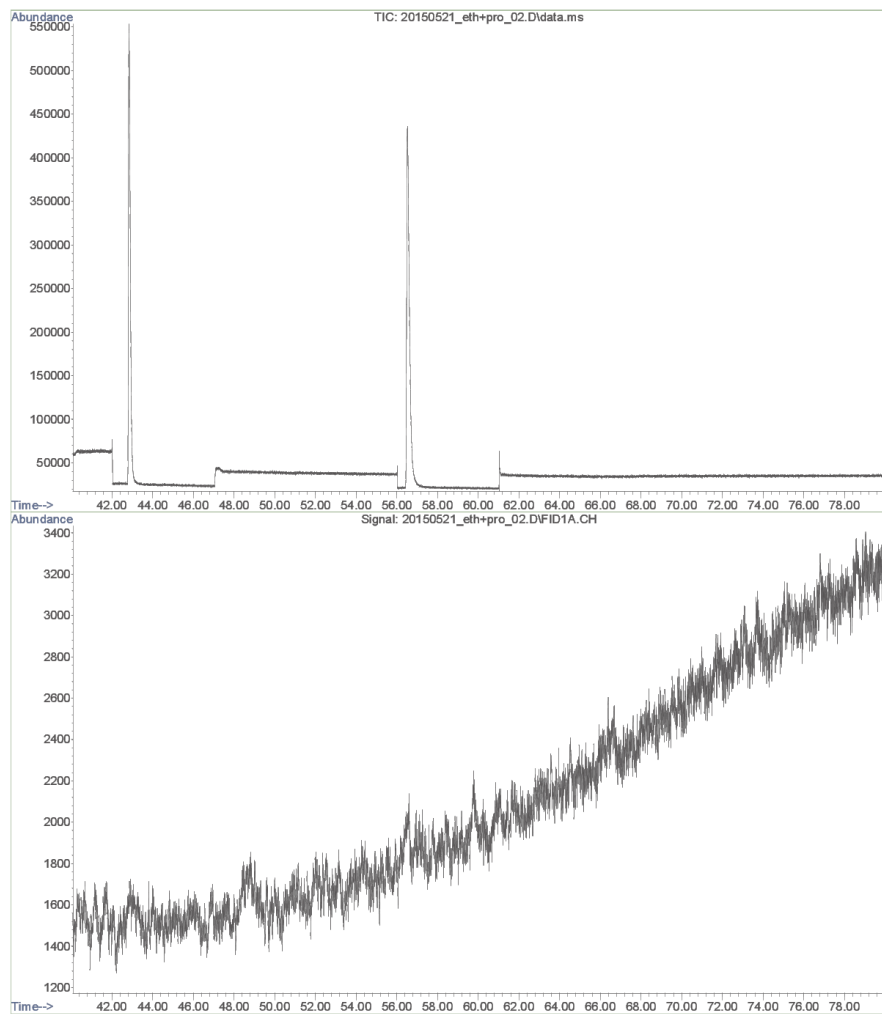
Figure A.4 Chromatograms reported during a KIE experiment by ChemStation with MSD (top paneltop panel) and FID (bottom panel) detectors. The peaks at RT = 42.85 min and RT = 56.53 min (top panel) correspond to ethane and propane, respectively.
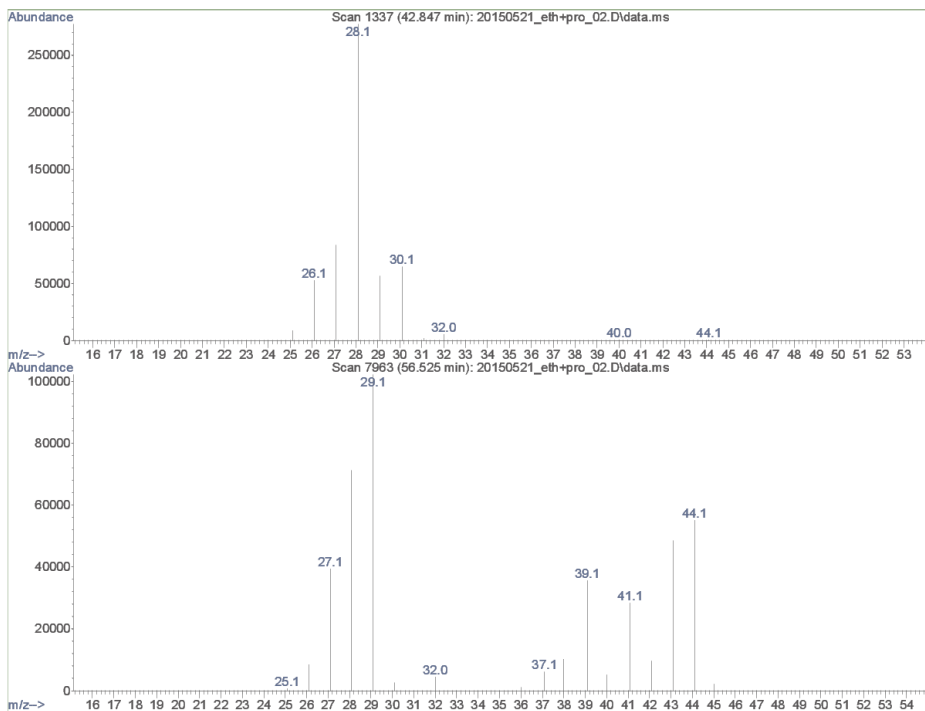
Figure A.5   Spectra of the peaks eluting at RT = 42.85 min (top panel) and at RT = 56.53 min (bottom panel) reported by ChemStation with MSD detector, indicating ethane and propane, respectively.

A.2   Evaluation of uncertainties

The statistical errors reported in this work are calculated by propagating the uncertainties through all steps of KIE calculations. These include the determination of the relative concentrations $[C]_t/[C]_0$, of δ^{13}C values together with the ^{17}O correction (see Section 2.3). The final error propagation step regards deriving of KIE from concentration and isotopic composition experimental data.

A.2.1 Relative concentration

The error of $[C]_t/[C]_0$ is calculated by using:

$$\frac{\Delta\left(\frac{[C]_t}{[C]_0}\right)}{\left(\frac{[C]_t}{[C]_0}\right)} = \sqrt{\left(\frac{\Delta[C]_t}{[C]_t}\right)^2 + \left(\frac{\Delta[C]_0}{[C]_0}\right)^2}$$

(A2.1)

where $[C]_t/[C]_0$ are relatively derived from the peak areas of m/z 44. $\Delta[C]_t/[C]_0$ and $\Delta[C]_t/[C]_t$ represent the relative errors for the concentration measurements at times 0 and t. These can be derived from the concentration stability measurements, by determining the standard error to the mean for all concentration measurements. For simplifying, since the control measurements were not carried out for the whole range of ethane and propane concentrations, the relative errors at different times were considered equal:

$$\frac{\Delta[C]_t}{[C]_t} = \frac{\Delta[C]_0}{[C]_0}.$$

(A2.2)

Thus Equation A2.1 became:

$$\Delta\left(\frac{[C]_t}{[C]_0}\right) = \sqrt{2} \cdot \frac{[C]_t}{[C]_0} \cdot \frac{\Delta[C]_0}{[C]_0}$$

(A2.3)

A.2.2 Relative rate approach

In relative rate calculation, the ratio of the oxidation reaction rate constants $k_{ethane}/k_{propane}$ was obtained from Equation 1.13, representing the slope of the line fitted to the experimental data, plotted as $\ln([ethane]_0/[ethane]_t)$ vs. $\ln([propane]_0/[propane]_t)$. The slope and its error $b_{RR} \pm \Delta b_{RR}$, were computed by using the data visualization software IDL (Interactive Data Language). The employed procedure was 'fitexy' (http://idlastro.gsfc.nasa.gov/ftp/pro/math/fitexy.pro) to find the best straight-line fit to data with errors in both coordinates. To this end, the errors of $\ln([ethane]_0/[ethane]_t)$ and $\ln([propane]_0/[propane]_t)$ had to be determined. By replacing $[ethane]_0$ and $[propane]_0$ with $[C]_0$ and $[ethane]_t$ and $[propane]_t$ with $[C]_t$, the error of $\ln([C]_0/[C]_t)$ can be described according to the Section A2.1:

$$\Delta\left(\ln\left(\frac{[C]_0}{[C]_t}\right)\right) = \sqrt{2} \cdot \frac{\Delta[C]_0}{[C]_0}. \tag{A2.4}$$

k_{ethane} was then derived from equation 1.11 as:

$$k_{ethane} = \frac{k_{propane}}{b_{RR}}. \tag{A2.5}$$

Thus, the errors of k_{ethane} can be derived as following.

$$\frac{\Delta\left(\frac{k_{propane}}{b_{RR}}\right)}{\left(\frac{k_{propane}}{b_{RR}}\right)} = \sqrt{\left(\frac{\Delta k_{propane}}{k_{propane}}\right)^2 + \left(\frac{\Delta b_{RR}}{b_{RR}}\right)^2} \tag{A2.6}$$

$$\Delta k_{ethane} = \Delta\left(\frac{k_{propane}}{b_{RR}}\right) = \frac{k_{propane}}{b_{RR}} \cdot \sqrt{\left(\frac{\Delta k_{propane}}{k_{propane}}\right)^2 + \left(\frac{\Delta b_{RR}}{b_{RR}}\right)^2} \tag{A2.7}$$

The error bars depicted in Figure 2.8 were calculated by using the Equation A2.7, where the reaction rate constant for OH oxidation for propane and its error $k_{propane} \pm \Delta k_{propane}$ were the IUPAC recommended values.

A.2.3 Chemical conversion of the reactants

The error bars for the chemical conversion of ethane and propane, $1 - ([C]_t/[C]_0)$, depicted in Figure 2.9, were derived by using Equation A2.3.

A.2.4 Delta values calculation

For each sample, $\delta^{13}C$ of ethane and propane were determined and corrected for ^{17}O by employing Equation 1.20. The $\delta^{13}C$ error was calculated as:

$$\Delta\delta^{13}C = \sqrt{\left(1.0704 \cdot \Delta^{45}\delta_{ref\text{-}sample}\right)^2 + \left(0.0372 \cdot \Delta^{46}\delta_{ref\text{-}sample}\right)^2 + \Delta^{13}\delta_{VPDB\text{-}ref}{}^2}. \tag{A2.8}$$

The errors for the delta values $\Delta^{45}\delta_{ref\text{-}sample}$ and $\Delta^{46}\delta_{ref\text{-}sample}$ are similarly determined (see Equations 1.21 and 1.22).

$$\Delta^{45}\delta_{ref-sample} = 1000 \cdot \Delta\left(\frac{^{45}R_{sample} - {}^{45}R_{ref}}{^{45}R_{ref}}\right) \tag{A2.9}$$

$$\Delta^{46}\delta_{ref-sample} = 1000 \cdot \Delta\left(\frac{^{46}R_{sample} - {}^{46}R_{ref}}{^{45}R_{ref}}\right) \tag{A2.10}$$

$$\Delta^{45}\delta_{ref-sample} = 1000 \cdot \sqrt{\frac{\Delta\,^{45}R_{sample}{}^2 + \Delta\,^{45}R_{ref}{}^2}{^{45}R_{ref}{}^2} + \frac{\Delta\,^{45}R_{ref}{}^2 \cdot \left({}^{45}R_{sample} - {}^{45}R_{ref}\right)^2}{^{45}R_{ref}{}^4}} \tag{A2.11}$$

$$\Delta^{46}\delta_{ref-sample} = 1000 \cdot \sqrt{\frac{\Delta\,^{46}R_{sample}{}^2 + \Delta\,^{46}R_{ref}{}^2}{^{46}R_{ref}{}^2} + \frac{\Delta\,^{46}R_{ref}{}^2 \cdot \left({}^{46}R_{sample} - {}^{46}R_{ref}\right)^2}{^{46}R_{ref}{}^4}} \tag{A2.12}$$

For each experiment, the standard errors of the mean, $\Delta^{45}R_{ref}$ and $\Delta^{46}R_{ref}$ were determined from the $^{45}R_{ref}$ and $^{46}R_{ref}$ of the 15 standard gas peaks. $\Delta^{45}R_{sample}$ and $\Delta^{46}R_{sample}$

for ethane and propane were derived from the $\delta^{13}C$ stability measurements (see Section 2.1.3).

A.2.5 KIE calculation

For each experiment, the *KIE* value was obtained by employing Equation 1.15. Similarly to Section 2.3, a linear least-squares approximation was computed for the experimental data expressed as $\ln([^{12}C]_t/[^{12}C]_0)$ versus $\ln((\delta^{13}C_t+1000)/(\delta^{13}C_0+1000))$ together with their errors. The errors for the y axis $\ln([^{12}C]_t/[^{12}C]_0)$ were evaluated as described in equations A2.4. For the x axis, errors of the delta values measured at the beginning and during the reaction, $\Delta\delta13C_0$ and $\Delta\delta^{13}C_t$ respectively, were necessary.

$$\frac{\Delta\left(\frac{1000+\delta^{13}C_t}{1000+\delta^{13}C_0}\right)}{\left(\frac{1000+\delta^{13}C_t}{1000+\delta^{13}C_0}\right)} = \sqrt{\left(\frac{\Delta\delta^{13}C_t}{1000+\delta^{13}C_t}\right)^2 + \left(\frac{\delta^{13}C_0}{1000+\delta^{13}C_0}\right)^2} \tag{A2.13}$$

$$\Delta\left(ln\left(\frac{1000+\delta^{13}C_t}{1000+\delta^{13}C_0}\right)\right) = \left(\frac{1000+\delta^{13}C_t}{1000+\delta^{13}C_0}\right)\cdot\Delta\left(\frac{1000+\delta^{13}C_t}{1000+\delta^{13}C_0}\right)$$

$$= \sqrt{\left(\frac{\Delta\delta^{13}C_t}{1000+\delta^{13}C_t}\right)^2 + \left(\frac{\delta^{13}C_0}{1000+\delta^{13}C_0}\right)^2} \tag{A2.14}$$

The slope and its error, $b_{KIE} \pm \Delta b_{KIE,}$ were derived by employing the IDL procedure 'fitexy' (see above). Subsequently, KIE errors were calculated by using Equation A2.15:

$$\Delta KIE = \frac{\Delta b_{KIE}}{(b_{KIE}+1)^2} \tag{A2.15}$$

A.3 Stability of TD-GC-C-IRMS

Stability experiment was described in Section 2.2.1. Concentration change and δ^{13}C of ethane and propane as function of time in stability experiment are shown in Figure A.6.
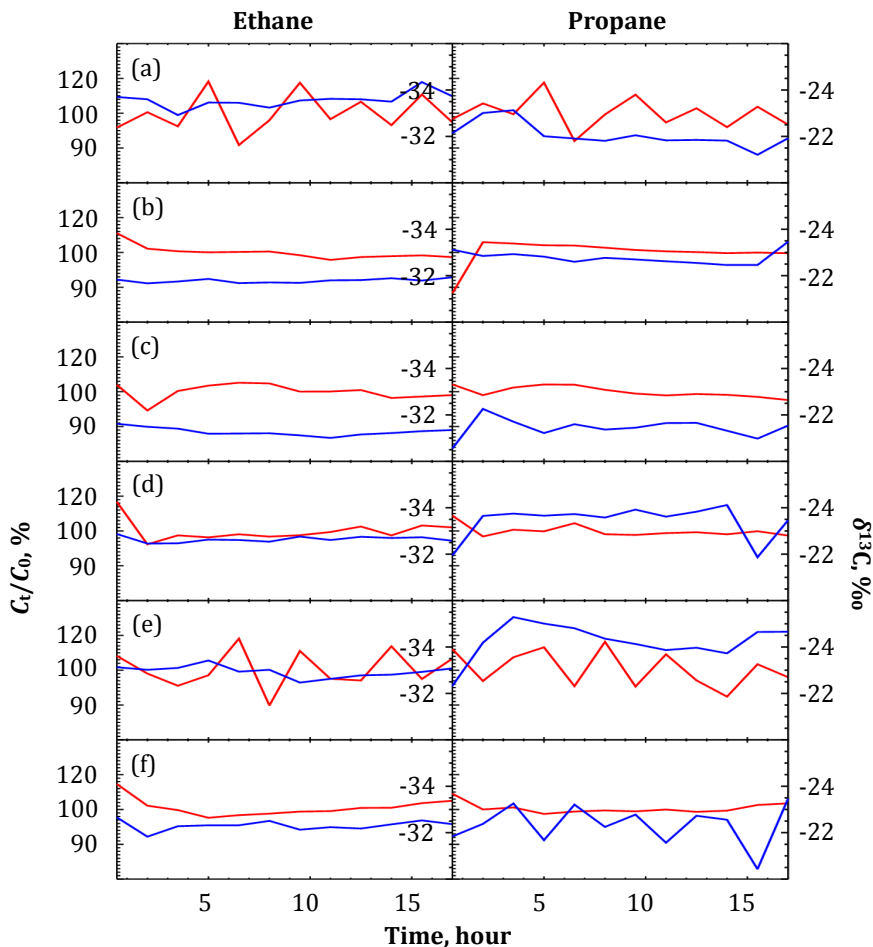
Figure A.6 Concentration change (red lines) and δ^{13}C (blue lines) of ethane (left) and propane (right) for 12 measurements during 17 hours in stability experiment at (a) 303.0 ± 0.1, (b) 288.0 ± 0.2, (c) 272.7 ± 0.3, (d) 262.9 ± 0.3, (e) 253.2 ± 0.3, and (f) 242.7 ± 0.3 K

A.4 Results for relative rate experiment

In the following table, the IUPAC recommended reaction rate constants for the oxidation of propane by OH at the investigated temperature ($k_{propane}$), as well as the experimentally derived k_{ethane} are listed. The details of the relative rate approach used for this are described in Section 2.3.1. Figures A.7-A.25 illustrate the linear least-squares regression analyses, carried out for the experimental data expressed as $\ln([ethane]_0/[ethane]_t)$ versus $\ln([propane]_0/[propane]_t)$.

Table A.1   IUPAC recommended $k_{propane}$ at the investigated temperatures, the slopes of the lines fitted to the experimental data expressed as $\ln([ethane]_0/[ethane]_t)$ vs. $\ln([propane]_0/[propane]_t)$ (see Figures A.7-A.25), the observed k_{ethane} for all experiments, as well as the averaged k_{ethane} at the investigated temperatures. $k_{propane}$ and k_{ethane} are expressed in 10^{-13} cm^3 molecule^{-1} s^{-1}.

T, K	$k_{propane}$	Exp. No.	slope	k_{ethane}	$k_{ethane,AVG}$
		1	0.248 ± 0.018	2.73 ± 0.77	
303.0 ± 0.1	11.0 ± 0.43	2	0.235 ± 0.016	2.59 ± 0.73	2.55 ± 0.73
		3	0.211 ± 0.019	2.32 ± 0.66	
		4	0.233 ± 0.009	2.32 ± 0.68	
288.0 ± 0.2	9.97± 0.41	5	0.217 ± 0.006	2.16 ± 0.64	2.28 ± 0.67
		6	0.236 ± 0.006	2.35 ± 0.69	
		7	0.182 ± 0.012	1.62 ± 0.51	
273.0 ± 0.3	8.92 ± 0.39	8	0.176 ± 0.006	1.57 ± 0.49	1.56 ± 0.49
		9	0.167 ± 0.005	1.49 ± 0.47	

Table A.1   Continued.

T, K	$k_{propane}$	Exp. No.	slope	k_{ethane}	$k_{ethane,AVG}$
		10	0.172 ± 0.008	1.42 ± 0.47	
263.0 ± 0.3	8.22 ± 0.38	11	0.173 ± 0.010	1.42 ± 0.47	1.54 ± 0.53
		12	0.218 ± 0.012	1.79 ± 0.59	
		13	0.179 ± 0.045	1.35 ± 0.52	
253.0 ± 0.3	7.53 ± 0.36	14	0.228 ± 0.070	1.72 ± 0.70	1.66 ± 0.66
		15	0.255 ± 0.036	1.92 ± 0.69	
		16	0.187 ± 0.031	1.28 ± 0.48	
		17	0.101 ± 0.036	6.93 ± 0.30	
243.0 ± 0.3	6.84 ± 0.35	18	0.257 ± 0.025	1.76 ± 0.65	1.34 ± 0.66
		19	0.237 ± 0.018	1.63 ± 0.59	
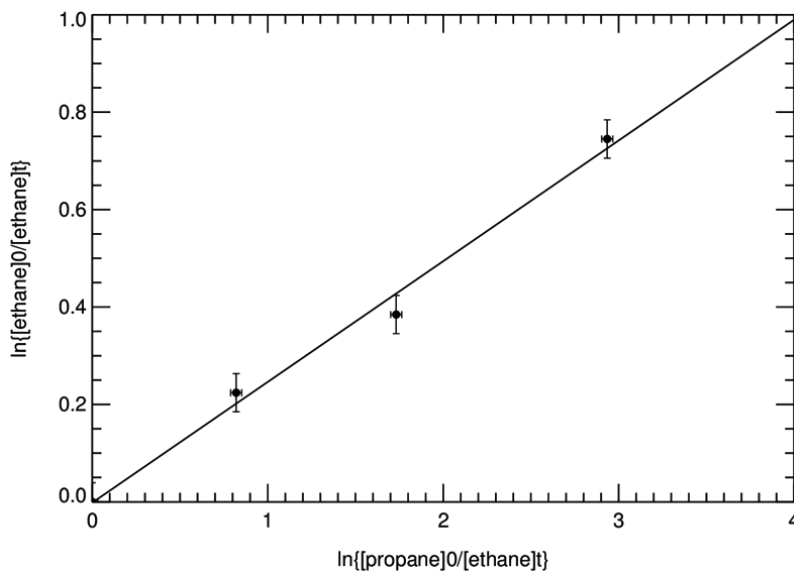
Figure A.7   Relative rate analysis at 303.0 ± 0.1 K (Exp. No. 1, Table A.1).
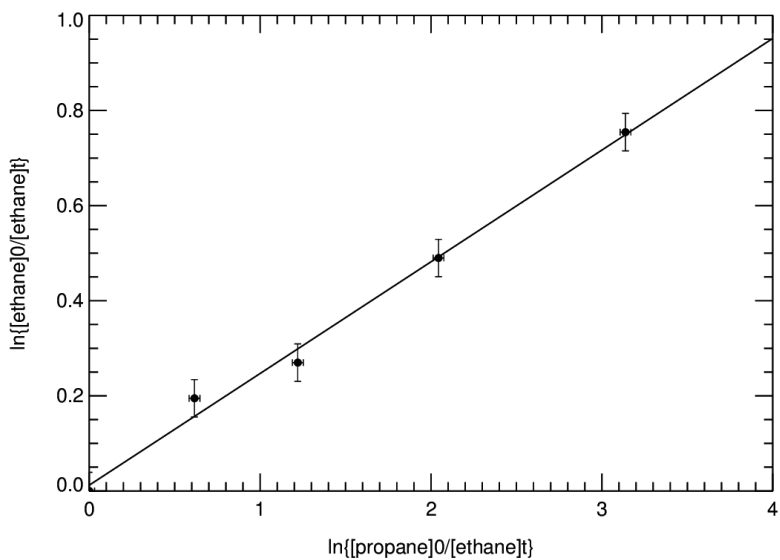
Figure A.8 Relative rate analysis at 303.0 ± 0.1 K (Exp. No.2, Table A.1).
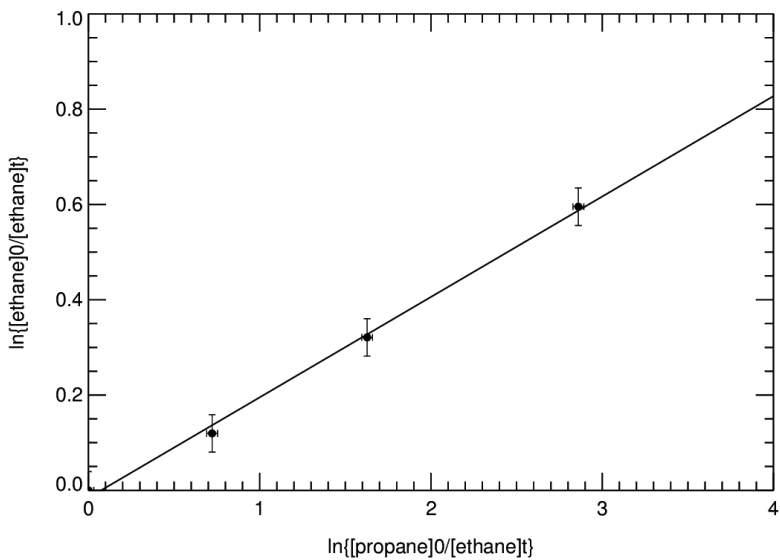
Figure A.9 Relative rate analysis at 303.0 ± 0.1 K (Exp. No.3, Table A.1).
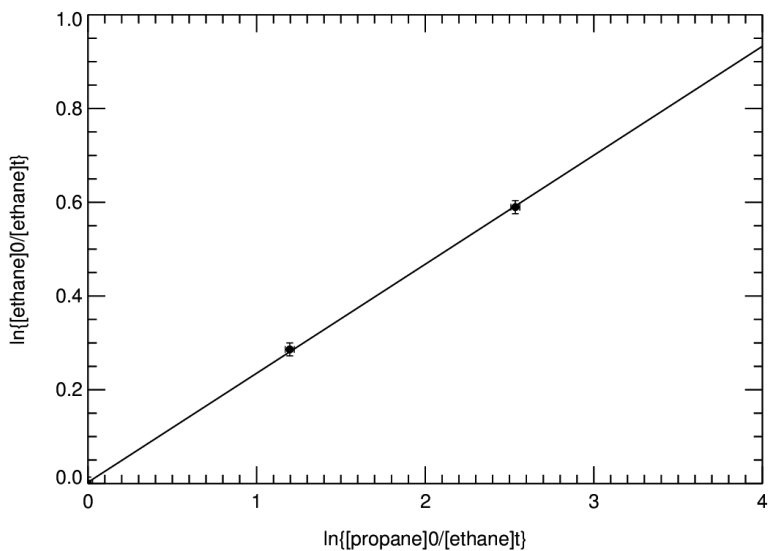
Figure A.10 Relative rate analysis at 288.0 ± 0.2 K (Exp. No.4, Table A.1).
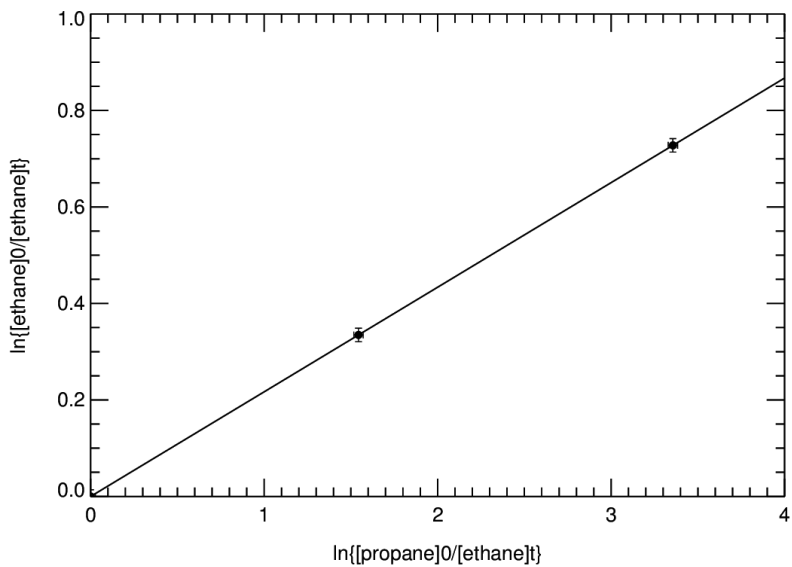
Figure A.11 Relative rate analysis at 288.0 ± 0.2 K (Exp. No.5, Table A.1).
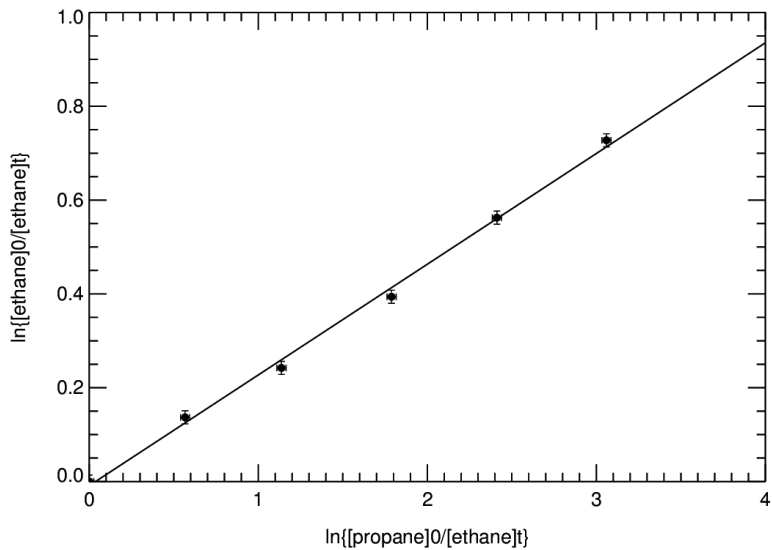
Figure A.12 Relative rate analysis at 288.0 ± 0.2 K (Exp. No.6, Table A.1).
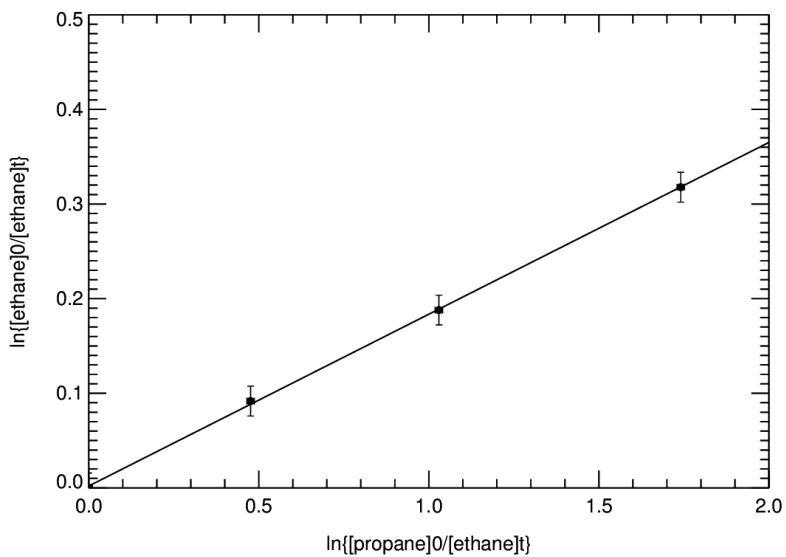
Figure A.13 Relative rate analysis at 272.7 ± 0.3 K (Exp. No.7, Table A.1).
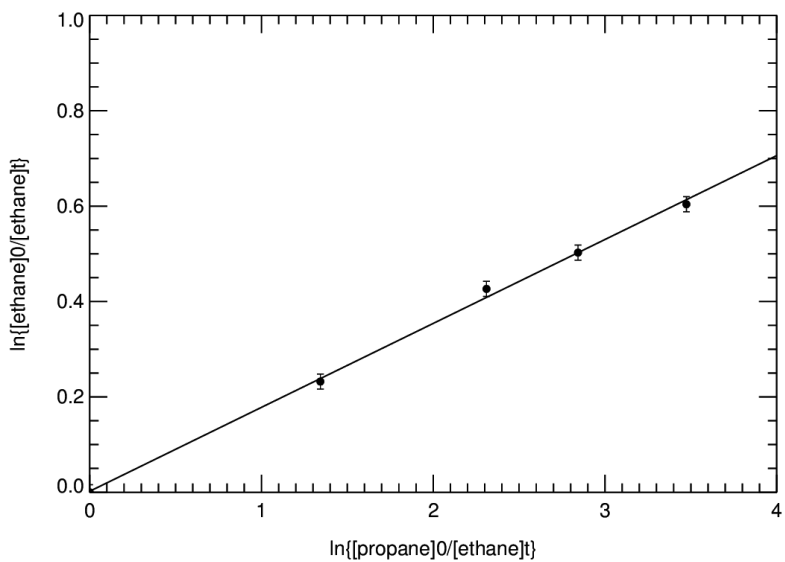
Figure A.14 Relative rate analysis at 272.7 ± 0.3 K (Exp. No.8, Table A.1).
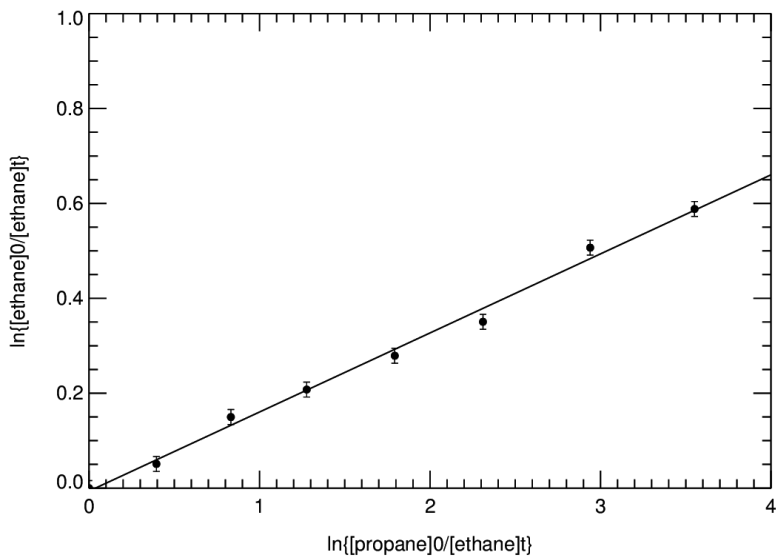
Figure A.15 Relative rate analysis at 272.7 ± 0.3 K (Exp. No.9, Table A.1).
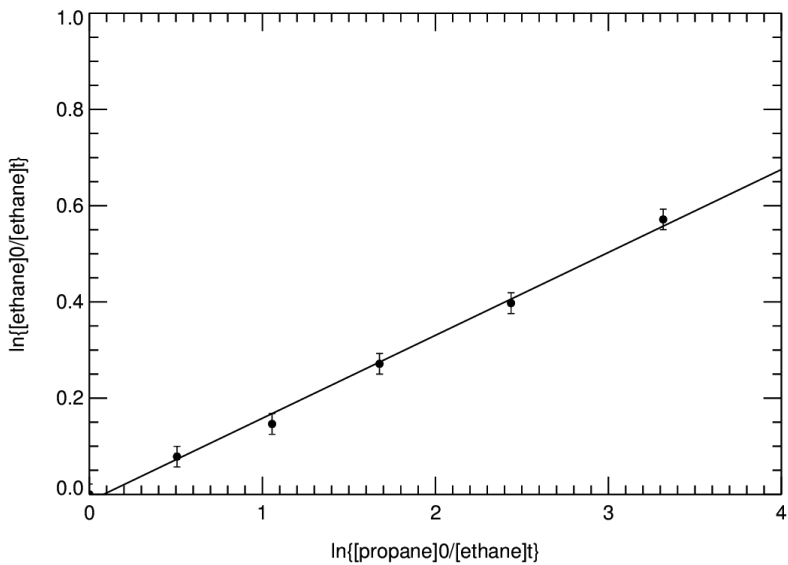
Figure A.16 Relative rate analysis at 262.9 ± 0.3 K (Exp. No.10, Table A.1).
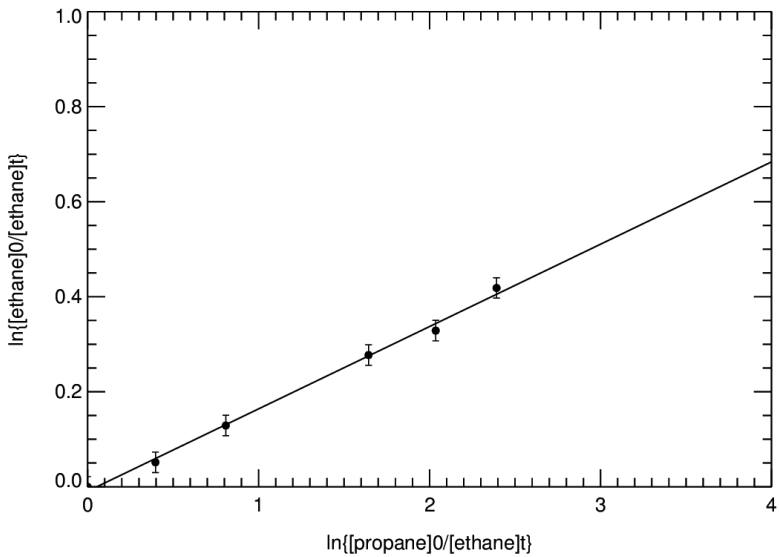
Figure A.17 Relative rate analysis at 262.9 ± 0.3 K (Exp. No.11, Table A.1).
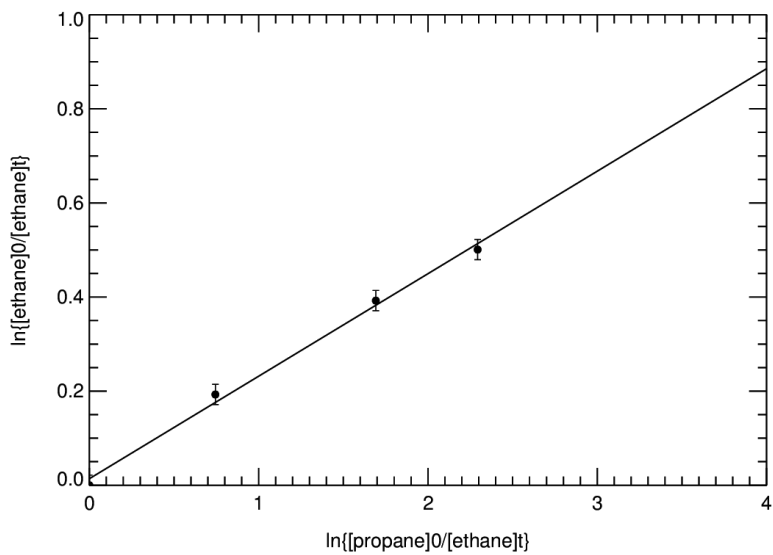
Figure A.18 Relative rate analysis at 262.9 ± 0.3 K (Exp. No.12, Table A.1).
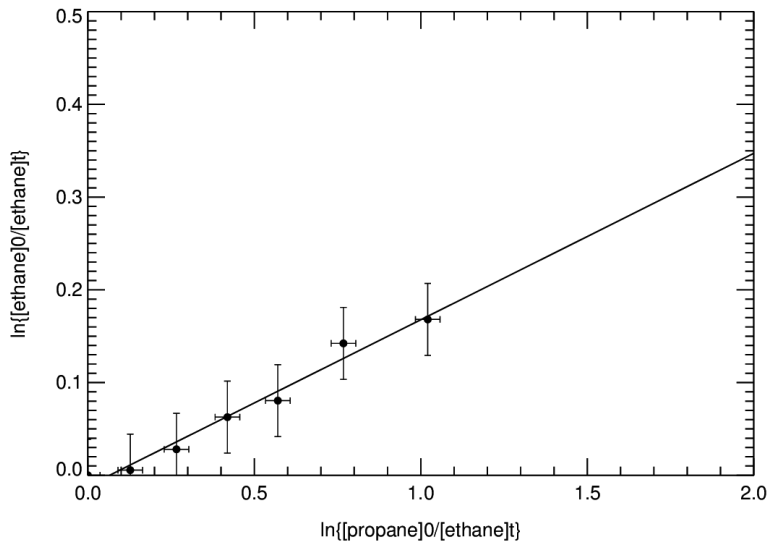
Figure A.19 Relative rate analysis at 253.2 ± 0.3 K (Exp. No.13, Table A.1).
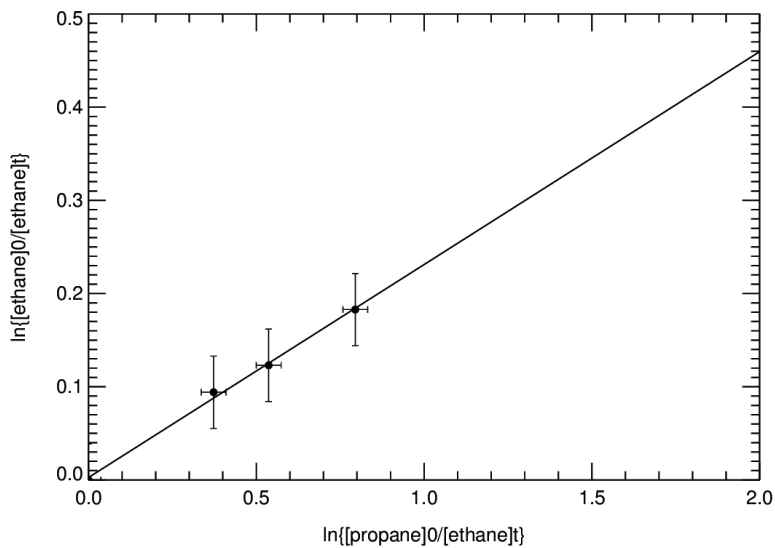
Figure A.20 Relative rate analysis at 253.2 ± 0.3 K (Exp. No.14, Table A.1).
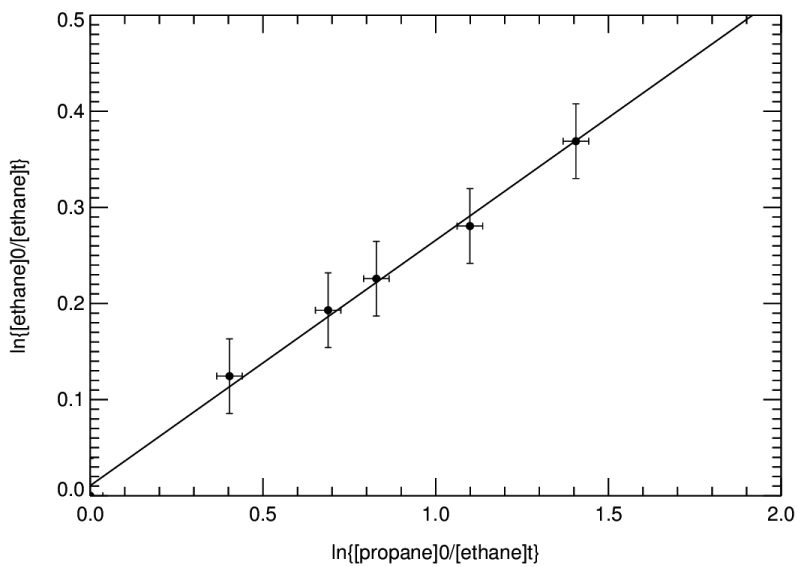
Figure A.21 Relative rate analysis at 253.2 ± 0.3 K (Exp. No.15, Table A.1).
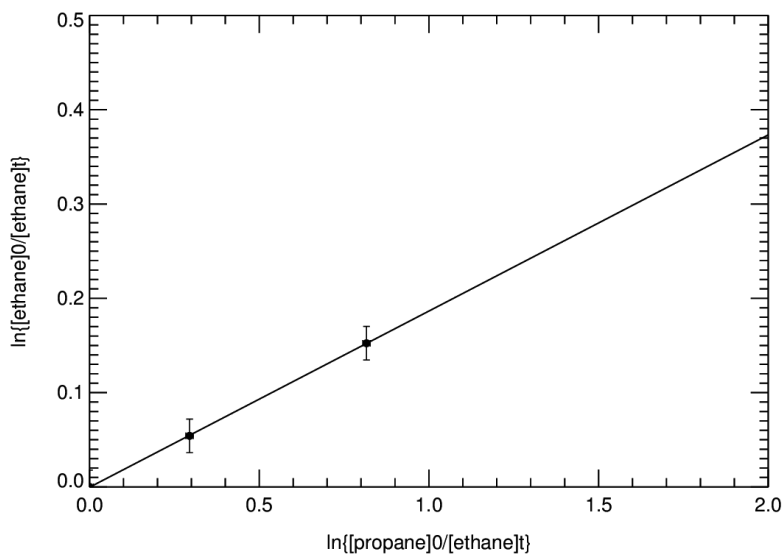
Figure A.22 Relative rate analysis at 242.7 ± 0.3 K (Exp. No.16, Table A.1).
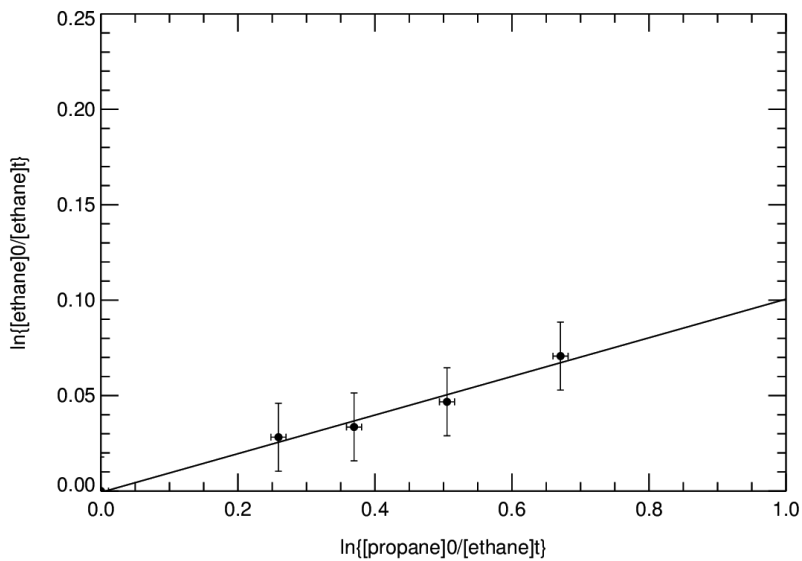
Figure A.23 Relative rate analysis at 242.7 ± 0.3 K (Exp. No.17, Table A.1).
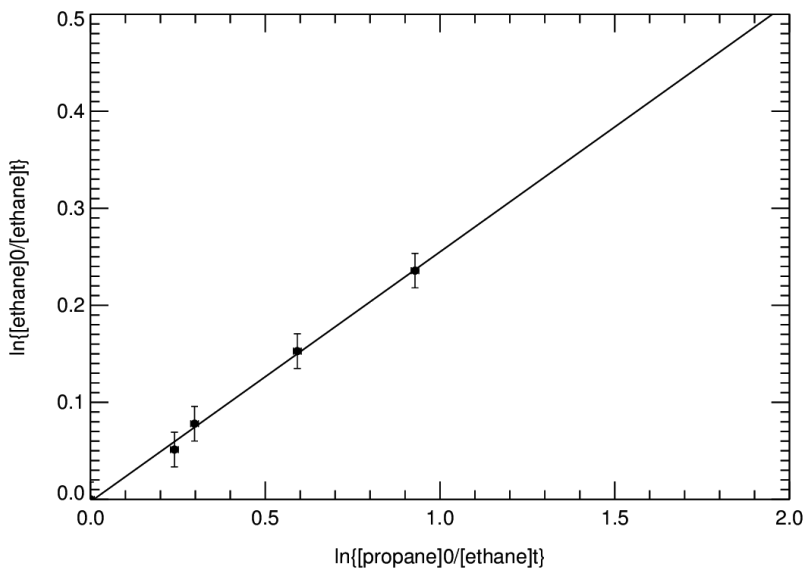
Figure A.24   Relative rate analysis at 242.7 ± 0.3 K (Exp. No.18, Table A.1).
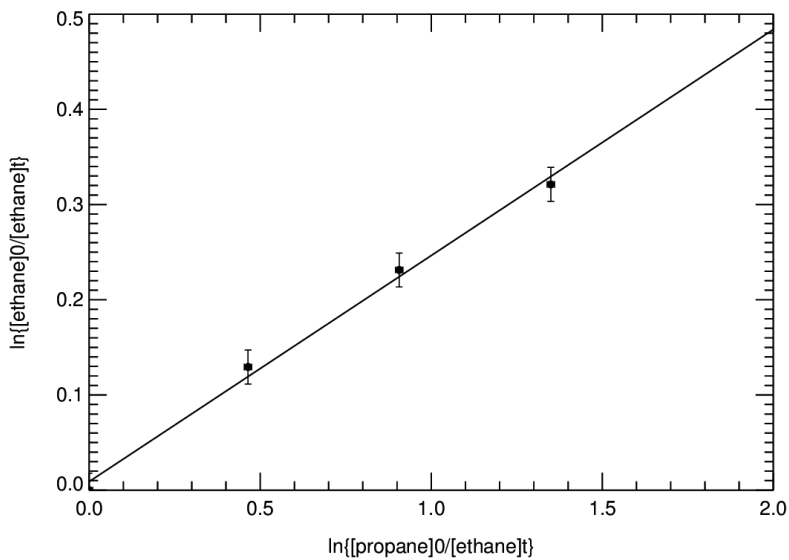
Figure A.25   Relative rate analysis at 242.7 ± 0.3 K (Exp. No.19, Table A.1).

A.5 Results for KIE experiments

A summary of the observed KIE values for the oxidation of ethane and propane by OH are shown in Table A.2. The results are presented for all experiments. Average $^{OH}\varepsilon$ are also given at each investigated temperature. Figures A.26-A.44 illustrate the linear least-squares regression analyses, carried out for the ethane and propane experimental data expressed as $\ln([^{12}C]_t/[^{12}C]_0)$ vs. $\ln((\delta^{13}C_t+1000)/(\delta^{13}C_0+1000))$. Details of deriving KIE from laboratory observations are given in Section 2.3.2.

Table A.2   Summary of the KIE values for all experiments of ethane and propane oxidation by OH. Average $^{OH}\varepsilon$ are presented for each investigated temperature.   Additionally, the slopes of the lines fitted to the experimental data expressed as $\ln([^{12}C]_t/[^{12}C]_0)$ vs. $\ln((\delta^{13}C_t+1000)/(\delta^{13}C_0+1000))$ are shown (see Figures A.26-A.44).

T, K	Exp. No.	Ethane			Propane		
		slope	$^{OH}\varepsilon$, ‰	$^{OH}\varepsilon_{avg}$, ‰	slope	$^{OH}\varepsilon$, ‰	$^{OH}\varepsilon_{avg}$, ‰
303.0 ± 0.1	1	-148.5±9.0	6.78±0.41		-333.1±14.1	3.01±0.13	
	2	-136.4±7.4	7.39±0.40	7.16±0.54	-261.6±9.3	3.84±0.14	3.65±0.36
	3	-138.0±12.6	7.30±0.66		-244.0±9.9	4.12±0.17	
288.0 ± 0.2	4	-122.2±5.6	8.25±0.38		-275.1±13.2	3.65±0.17	
	5	-142.0±3.6	7.09±0.18	7.45±0.48	-323.9±12.8	3.10±0.12	3.60±0.31
	6	-143.6±3.6	7.01±0.17		-247.5±8.2	4.06±0.13	
273.0 ± 0.3	7	-141.6±3.4	7.11±0.17		-276.6±7.2	3.63±0.09	
	8	-140.4±2.6	7.18±0.13	7.36±0.28	-283.1±8.0	3.54±0.10	3.66±0.15
	9	-129.5±3.8	7.78±0.23		-264.5±12.6	3.80±0.18	

Table A.2   Continued.

T, K	Exp. No.	Ethane			Propane		
		slope	$^{OH}\varepsilon$, ‰	$^{OH}\varepsilon_{avg}$, ‰	slope	$^{OH}\varepsilon$, ‰	$^{OH}\varepsilon_{avg}$, ‰
263.0 ± 0.3	10	-126.9±3.5	7.94±0.22		-269.8±6.6	3.72±0.09	
	11	-132.8±12.6	7.59±0.71	7.61±0.51	-244.8±6.4	4.10±0.11	3.61±0.34
	12	-137.8±6.9	7.31±0.36		-333.6±10.6	3.01±0.10	
253.0 ± 0.3	13	-123.2±12.0	8.18±0.79		-220.0±27.7	4.57±0.57	
	14	-108.6±8.0	9.30±0.68	8.89±0.90	-201.9±26.3	4.98±0.64	4.87±0.56
	15	-109.7±11.8	9.20±0.98		-198.0±14.6	5.08±0.37	
243.0 ± 0.3	16	-107.4±28.3	9.40±2.45		-276.4±14.4	3.63±0.19	
	17	-90.4±18.2	10.11±2.23	9.42±2.19	-306.0±30.1	3.28±0.32	4.31±0.70
	18	-81.5±4.7	12.42±0.70		-173.0±7.8	5.81±0.26	
	19	-174.8±7.2	5.75±0.24		-221.7±7.5	4.53±0.15	
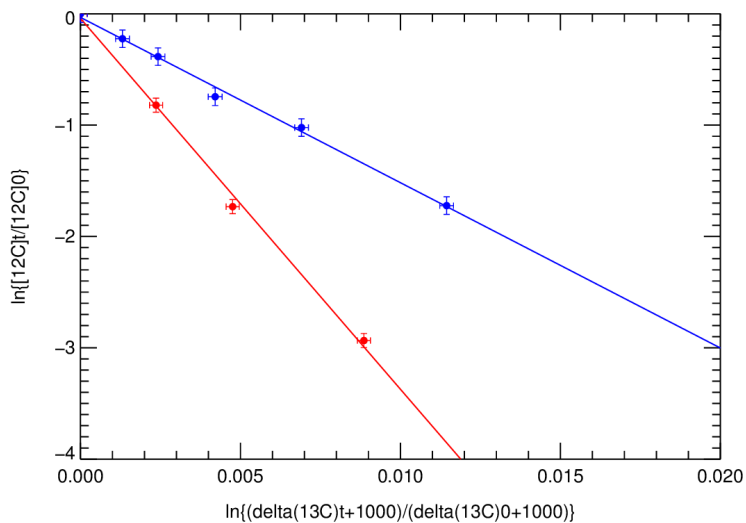
Figure A.26 KIE determination for ethane (blue) and propane (red) at 303.0 ± 0.1 K (Exp. No. 1, Table A.2).
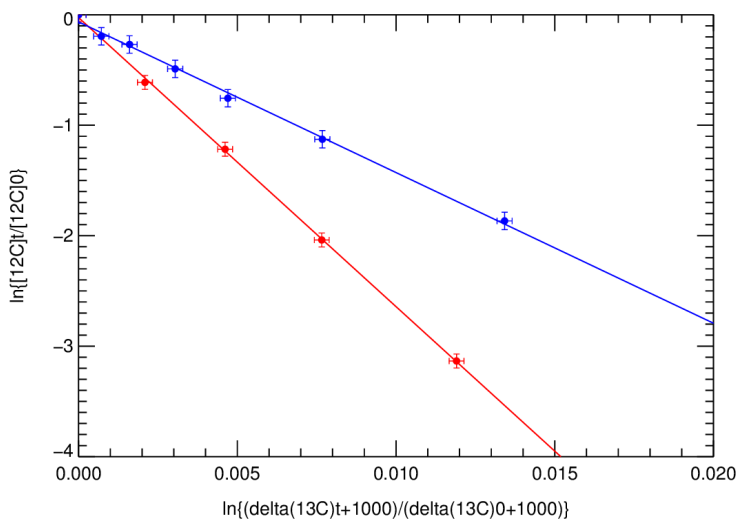
Figure A.27 KIE determination for ethane (blue) and propane (red) at 303.0 ± 0.1 K (Exp. No. 2, Table A.2).
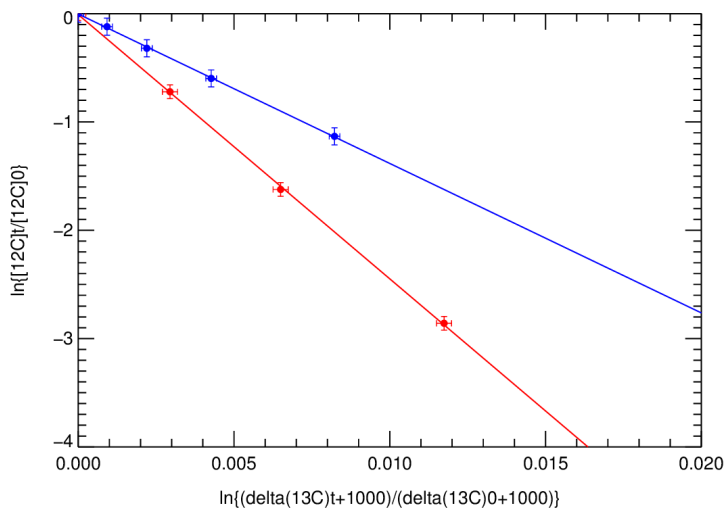
Figure A.28 KIE determination for ethane (blue) and propane (red) at 303.0 ± 0.1 K (Exp. No. 3, Table A.2).
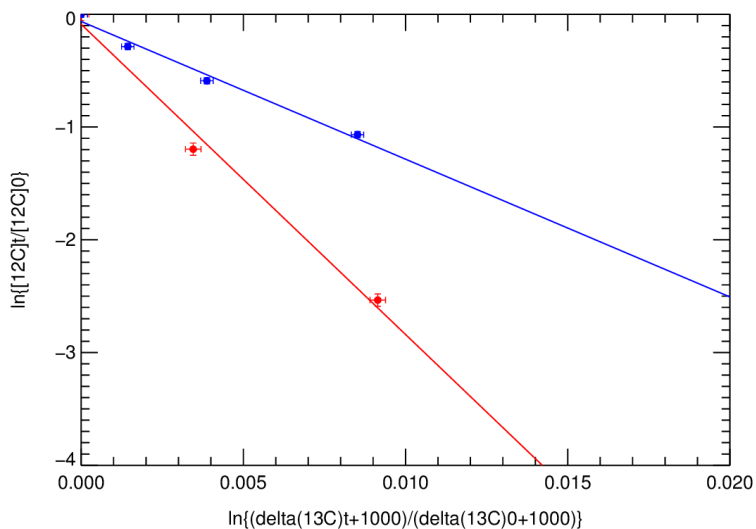
Figure A.29 KIE determination for ethane (blue) and propane (red) at 288.0 ± 0.2 K (Exp. No. 4, Table A.2).
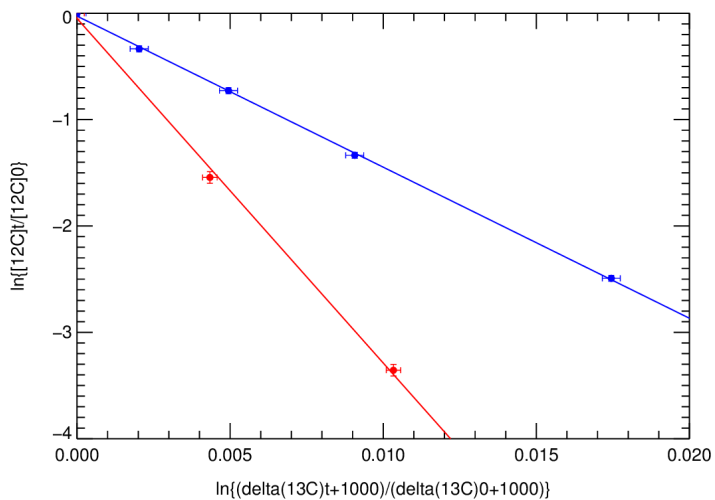
Figure A.30 KIE determination for ethane (blue) and propane (red) at 288.0 ± 0.2 K (Exp. No. 5, Table A.2).
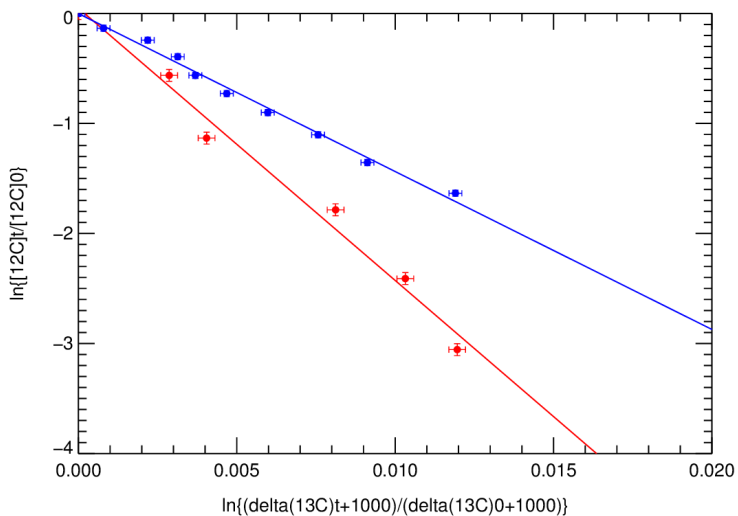
Figure A.31 KIE determination for ethane (blue) and propane (red) at 288.0 ± 0.2 K (Exp. No. 6, Table A.2).
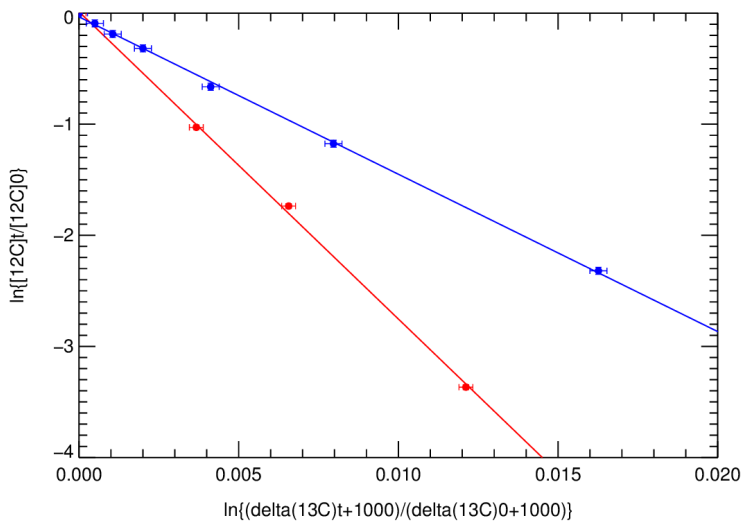
Figure A.32 KIE determination for ethane (blue) and propane (red) at 272.7 ± 0.3 K (Exp. No. 7, Table A.2).
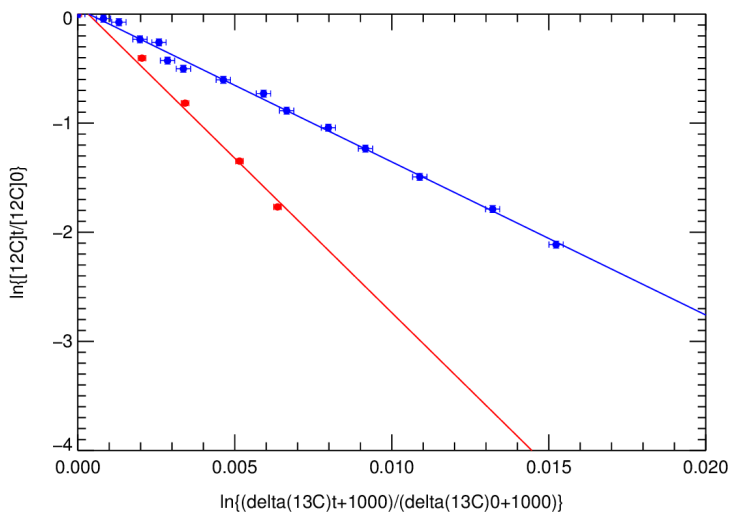
Figure A.33 KIE determination for ethane (blue) and propane (red) at 272.7 ± 0.3 K (Exp. No. 8, Table A.2).
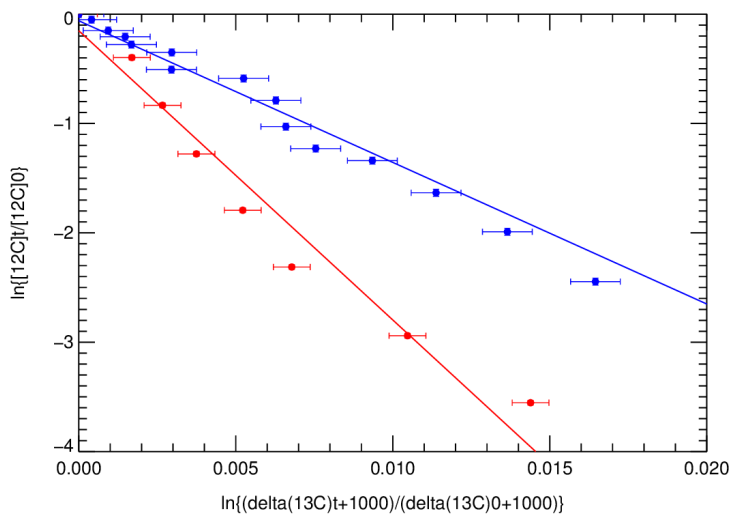
Figure A.34 KIE determination for ethane (blue) and propane (red) at 272.7 ± 0.3 K (Exp. No. 9, Table A.2).
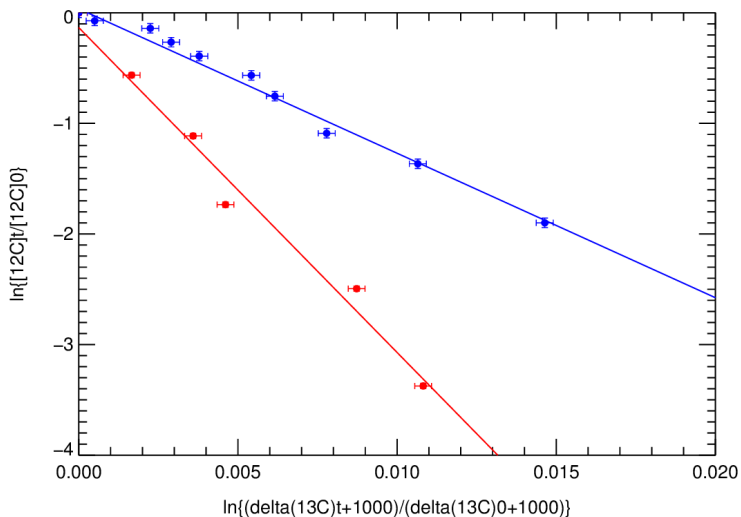
Figure A.35 KIE determination for ethane (blue) and propane (red) at 262.9 ± 0.3 K (Exp. No. 10, Table A.2).
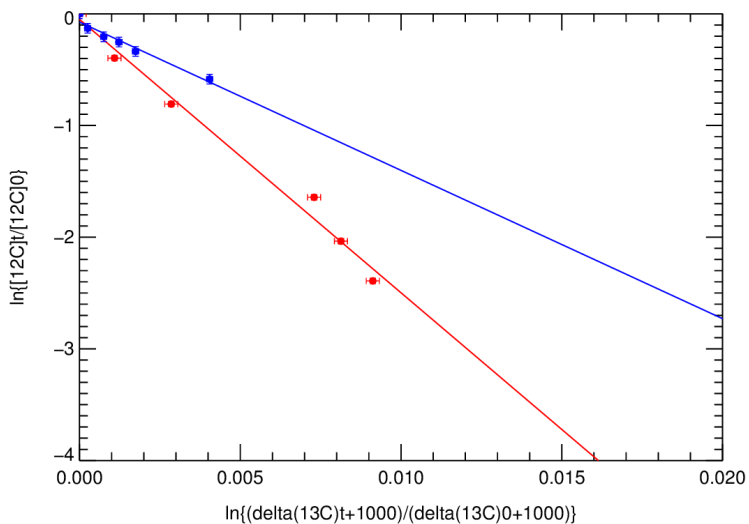
Figure A.36 KIE determination for ethane (blue) and propane (red) at 262.9 ± 0.3 K (Exp. No. 11, Table A.2).
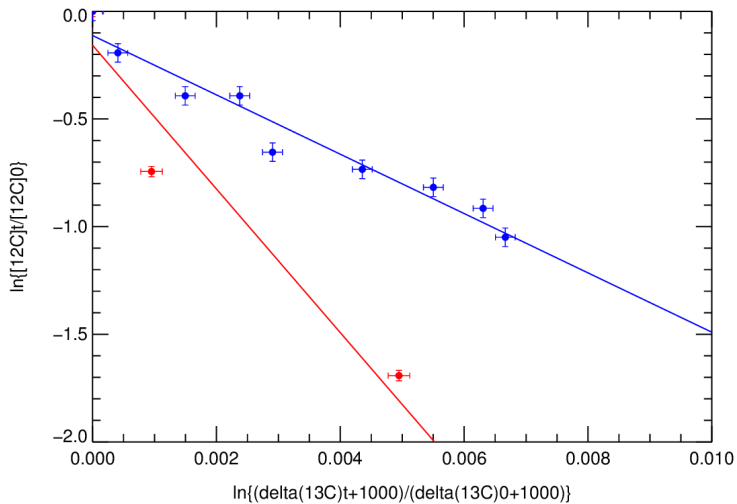
Figure A.37 KIE determination for ethane (blue) and propane (red) at 262.9 ± 0.3 K (Exp. No. 12, Table A.2).
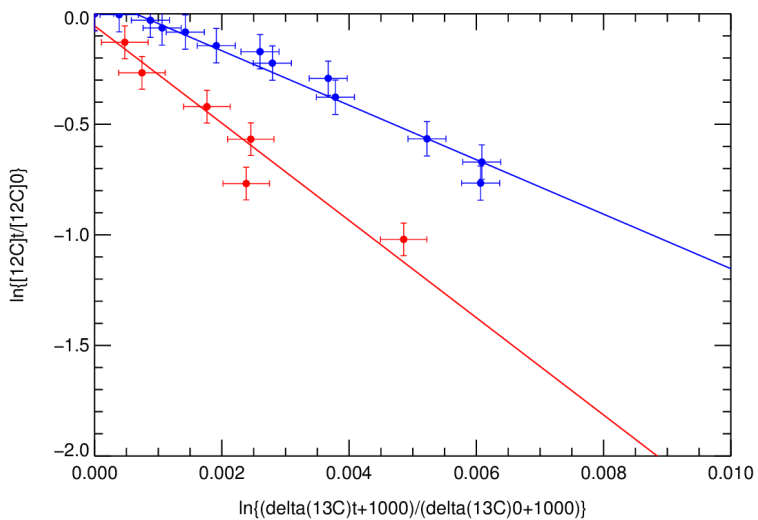
Figure A.38 KIE determination for ethane (blue) and propane (red) at 253.2 ± 0.3 K (Exp. No. 13, Table A.2).
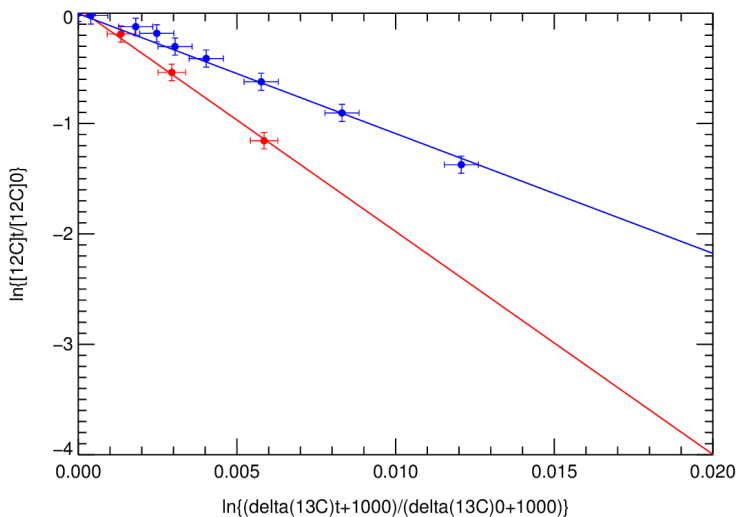
Figure A.39 KIE determination for ethane (blue) and propane (red) at 253.2 ± 0.3 K (Exp. No. 14, Table A.2).
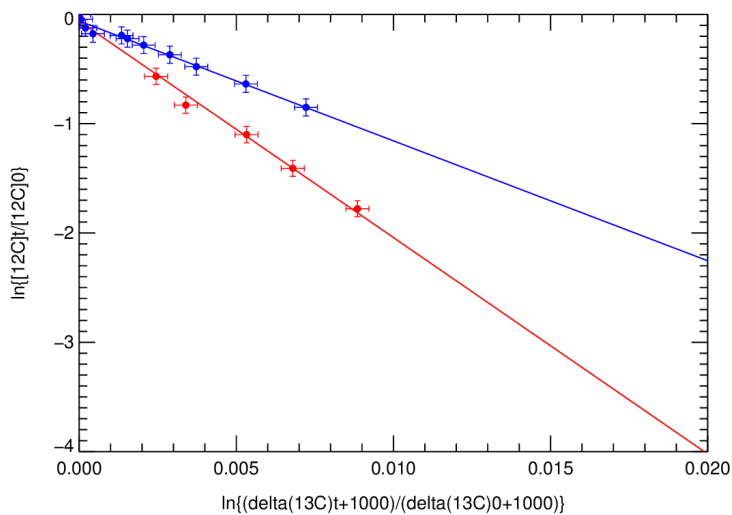
Figure A.40 KIE determination for ethane (blue) and propane (red) at 253.2 ± 0.3 K (Exp. No. 15, Table A.2).
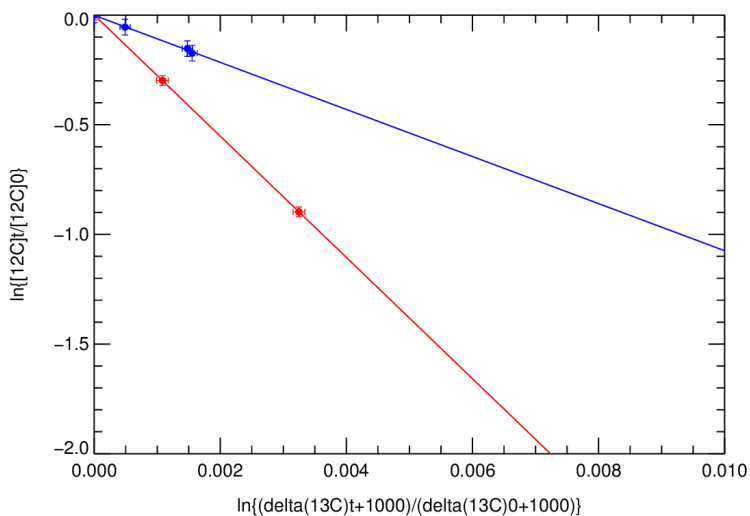
Figure A.41 KIE determination for ethane (blue) and propane (red) at 242.7 ± 0.3 K (Exp. No. 16, Table A.2).
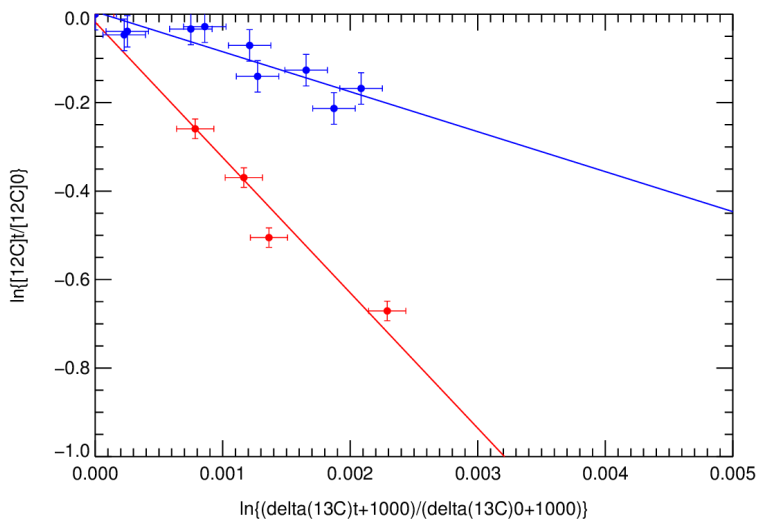
Figure A.42 KIE determination for ethane (blue) and propane (red) at 242.7 ± 0.3 K (Exp. No. 17, Table A.2).
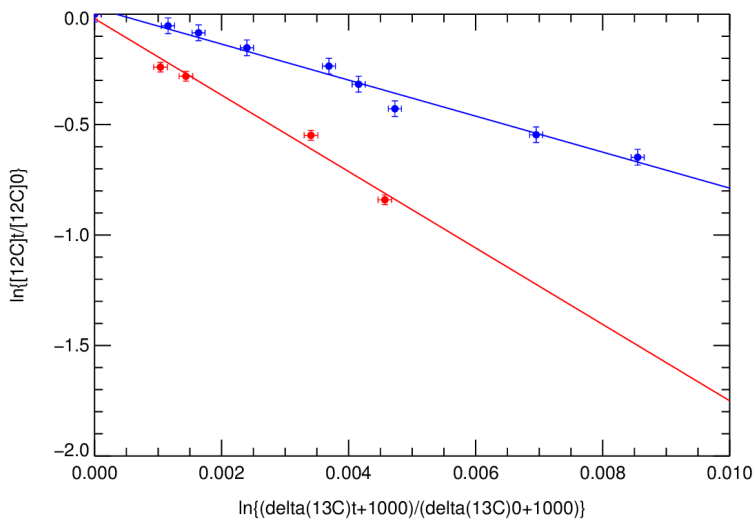
Figure A.43 KIE determination for ethane (blue) and propane (red) at 242.7 ± 0.3 K (Exp. No. 18, Table A.2).
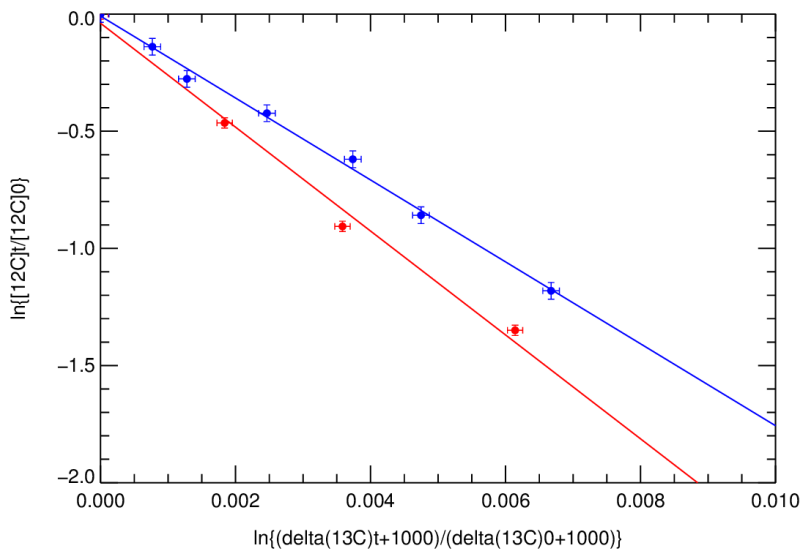
Figure A.44 KIE determination for ethane (blue) and propane (red) at 242.7 ± 0.3 K (Exp. No. 19, Table A.2).

A.6 Results for electronics calculation

Electronics calculations for stationary points involving in the reaction $C_2H_6 + OH \rightarrow$ $C_2H_5 + H_2O$ were performed at MO6-2X/aug-cc-pVTZ level of theory including geometry optimization, potential energies (PE), and anharmonic frequencies analysis. The PE refinement at CCSD(T)/CBS level of theory were further calculated on MO6-2X/ aug-cc-pVTZ optimized geometries, denoted CCSD(T)/CBS//MO6-2X/aug-cc-pVTZ.

A.6.1 Coordinates for optimized structure (Å)

A.6.1.1 Ethane

C1	-0.006372	0.069248	0.758635
H2	0.574976	-0.721359	1.231990
H3	-1.021085	0.013569	1.151494
4H	0.417092	1.023151	1.071428
C5	0.006373	-0.069248	-0.758634
H6	-0.574975	0.721359	-1.231990
H7	1.021086	-0.013569	-1.151493
H8	-0.417091	-1.023151	-1.071427

A.6.1.2 Hydroxyl radical

O1	0.000000	0.000000	0.108853
H2	0.000000	0.000000	-0.863079

A.6.1.3 Reactant complex

C1	1.245232	-0.718185	0.000025
H2	1.819948	-1.003497	-0.879867
H3	0.326581	-1.304686	0.000105
C4	0.954672	0.778354	0.000024
H5	0.390849	1.077340	0.886318
H6	1.873808	1.362624	-0.000043
H7	0.390727	1.077320	-0.886197
H8	1.820081	-1.003470	0.879838
O9	-2.297589	-0.114574	-0.000319
H10	-1.436947	0.340260	0.000217

A.6.1.4 Transition state

C1	-1.452913	-0.468678	0.024998
H2	-1.229147	-1.123196	0.865847
H3	-1.396171	-1.060985	-0.886636
C4	-0.496214	0.701603	-0.024756
H5	-0.644262	1.351595	-0.885251
H6	-0.489185	1.292589	0.889241
H7	0.578955	0.284424	-0.156368
H8	-2.481895	-0.121341	0.135099
O9	1.896352	-0.280379	-0.081312
H10	2.178955	0.192133	0.717355

A.6.1.5 Product complex

C1	-1.219284	-0.674818	-0.000925
H2	-0.765474	-1.122099	0.882956
H3	-0.759528	-1.123857	-0.880842
C4	-1.072367	0.803714	-0.001974
H5	-1.145075	1.360283	-0.924676
H6	-1.150666	1.362199	0.919109
H7	1.191206	0.388352	0.003524
H8	-2.276038	-0.968763	-0.004209
O9	1.994840	-0.144162	0.004797
H10	2.718538	0.485298	0.006639

A.6.1.6 Ethyl radicals

C1	-0.791691	0.000000	-0.023129
H2	-1.345169	0.923088	0.050529
H3	-1.345159	-0.923097	0.050502
C4	0.692227	0.000002	-0.000654
H5	1.101404	-0.883215	-0.491301
H6	1.101399	0.883366	-0.491036
H7	1.084307	-0.000157	1.024322

A.6.1.7 Water

H1	0.762603	-0.469662	0.000000
O2	0.000000	0.112265	0.000000
H3	-0.762604	-0.469661	0.000000

A.6.2 *Potential energies and zero-point energies*

Potential energies (PE) and zero-point energies (ZPE) of stationary points including ethane, hydroxyl radicals, reactant complex (RC), transition state (TS), product complex (PC), ethyl radical, and water were calculated on optimized geometries at MO6-2X/aug-cc-pVTZ level of theory. CCSD(T)/CBS//MO6-2X/aug-cc-pVTZ level of theory was further employed to refine energies for important stationary points. ZPEs for different ^{13}C isotopologues, denoted by C12, C13a and C13b, were calculated to be employed in KIE calculation. (See section 3.3 for details)

Table A.3   Potential energies (PE) in Hartrees calculated at CCSD(T)/CBS// MO6-2X/aug-cc-pVTZ for stationary points: ethane, hydroxyl radicals, reactant complex (RC), transition state (TS), product complex (PC), ethyl radical, and water; and their zero-point energies (ZPE) in Hartrees calculated at MO6-2X/aug-cc-pVTZ for different carbon isotopologues (C12, C13a, and C13b) for ethane, RC, TS, PC and ethyl radical. (See section 3.3 for details)

Species	PE		ZPE		
	MO6-2X	CCSD(T)	C12	C13a	C13b
C_2H_6	-79.8061325	-79.7131422	0.0749701	0.0747773	0.0747773
OH	-75.7338093	-75.6771459	0.0085803	0.0085803	0.0085803
RC	-155.542462	-155.392224	0.0900225	0.0898514	0.0898504
TS	-155.535019	-155.384320	0.0813573	0.0811791	0.0811898
PC	-155.571787	-155.419889	0.0839886	0.0838216	0.0838476
C_2H_5	-79.1362668	-79.0397764	0.0587922	0.0586289	0.0586589
H_2O	-76.4299975	-76.3778565	0.0211466	0.0211466	0.0211466

A.6.3   Harmonic vibrational frequencies (cm^{-1})

A.6.3.1   Ethane

Ethane-C12

305.88	822.46	822.65	1019.90	1221.37	1221.51
1406.02	1424.38	1507.66	1507.91	1509.65	1509.89
3066.06	3067.67	3120.58	3120.71	3143.81	3143.93

Ethane-C13

305.88	821.60	821.80	1004.70	1213.16	1213.30
1399.90	1419.78	1506.95	1507.19	1508.49	1508.73
3063.24	3067.08	3113.67	3113.81	3139.41	3139.54

A.6.3.2   Hydroxyl radical

3766.30

A.6.3.3   Reactant complex

RC-C12

69.12	77.59	124.83	166.54	189.33	348.36
823.62	827.22	1017.00	1220.50	1222.33	1404.07
1427.44	1510.63	1517.63	1518.19	1519.52	3048.25
3070.07	3102.58	3121.12	3143.45	3144.31	3745.75

RC-C13a

69.12	76.47	124.79	166.53	189.22	348.35
822.84	826.50	1001.58	1212.18	1213.95	1401.89
1419.20	1509.27	1516.45	1517.25	1519.43	3048.22
3066.62	3101.38	3115.76	3134.14	3137.50	3745.75

RC-C13b

69.13	77.49	122.88	166.40	189.28	348.32
822.73	826.27	1002.07	1212.55	1214.45	1395.15
1425.50	1510.51	1515.73	1516.42	1519.32	3044.45
3070.06	3092.10	3113.19	3140.59	3143.55	3745.75

A.6.3.4   Transition state

TS-C12

-683.00	54.72	101.40	153.31	343.13	733.55
808.67	875.05	1036.68	1140.56	1225.53	1268.59
1354.01	1408.43	1457.75	1493.26	1501.74	1523.36
3061.41	3094.13	3126.57	3138.77	3163.87	3791.46

TS-C13a

-682.53	54.63	100.48	153.303	43.10	733.41
807.85	873.29	1022.08	1134.71	1217.37	1267.55
1352.83	1398.28	1457.21	1491.83	1499.91	1523.16
3057.61	3093.58	3116.43	3129.57	3161.66	3791.45

TS-C13b

-680.80	54.68	100.86	152.93	342.61	732.31
806.34	874.47	1021.33	1125.87	1217.74	1261.97
1351.81	1408.32	1452.23	1492.93	1501.41	1521.96
3061.41	3088.44	3126.36	3134.39	3156.38	3791.45

A.6.3.5 Product complex

PC-C12

34.42	65.15	76.02	139.98	190.02	230.35
333.89	555.17	810.11	988.88	1075.88	1199.61
1404.66	1471.19	1484.75	1487.06	1618.25	3010.75
3094.57	3136.65	3166.69	3265.43	3801.38	3941.48

PC-C13a

34.39	64.17	76.00	139.92	190.02	230.12
333.89	555.16	809.55	981.70	1060.40	1190.21
1395.95	1469.90	1483.70	1484.29	1618.25	3005.02
3086.43	3125.36	3166.68	3265.37	3801.38	3941.48

PC-C13b

34.39	65.03	75.99	137.64	190.01	230.28
333.71	551.49	809.23	985.09	1059.38	1192.99
1404.42	1466.01	1484.22	1484.35	1618.25	3010.75
3094.57	3136.56	3161.25	3251.91	3801.38	3941.48

A.6.3.6 Ethyl radicals

Ethyl-C12

122.17	448.46	810.03	980.11	1080.72	1195.08
1403.03	1471.27	1487.12	1488.63	3004.04	3085.10
3128.52	3177.70	3276.83			

Ethyl-C13a

122.18	448.45	809.47	973.06	1065.35	1185.80
1393.87	1470.03	1484.45	1487.41	2998.07	3077.27
3117.28	3177.68	3276.77			

Ethyl-C13b

122.18	445.13	809.16	977.30	1063.87	1188.33
1402.86	1465.99	1484.24	1488.28	3004.04	3085.10
3128.46	3172.25	3263.16			

A.6.3.7   Water

| 1618.17 | 3869.58 | 3972.83 |

A.6.4 X-matrix of anharmonic constants (cm^{-1})

A.6.4.1   Ethane

Ethane-C12

	1	2	3	4	5
1	-10.050				
2	-11.136	-9.484			
3	-21.342	-20.776	-4.611		
4	-6.944	-7.067	4.580	-1.241	
5	-6.332	-5.989	4.874	-1.564	-0.823
6	-1.233	-0.759	10.037	-3.955	-3.263
7	-2.086	-1.706	-2.119	-4.947	-3.855
8	-1.958	-1.604	-2.183	-4.468	-4.168
9	1.495	1.496	0.234	-1.718	-1.704
10	-38.900	-10.252	-19.856	-7.133	-6.788

	1	2	3	4	5
11	-10.248	-36.717	-19.308	-7.391	-6.556
12	-20.349	-19.715	-18.361	-10.728	-10.122
13	-5.052	-4.953	11.905	-5.868	-3.390
14	-4.302	-4.519	12.154	-3.417	-4.054
15	-5.654	-5.213	2.389	-3.952	-3.281
16	-3.362	-3.305	-2.348	-8.064	-7.440
17	-4.341	-2.753	-2.679	-8.154	-7.048
18	2.425	2.774	2.598	-2.039	2.484

	6	7	8	9	10
6	-7.317				
7	-7.685	-2.414			
8	-6.825	-0.888	-2.206		
9	-6.177	-5.280	-5.306	-4.525	
10	-3.708	-2.376	-3.279	1.173	-9.663
11	-3.245	-2.936	-1.957	1.174	-10.672
12	6.060	-2.126	-2.161	0.220	-20.824
13	-4.219	-6.494	-5.709	-1.636	-5.980
14	-3.674	-5.091	-5.874	-1.626	-4.997
15	-20.085	-4.940	-4.050	-4.586	-4.376
16	-2.716	-7.958	0.616	-2.069	-3.158
17	-1.279	0.129	-6.069	-2.033	-3.451
18	0.476	-6.358	-6.851	1.198	1.693

	11	12	13	14	15
11	-9.137				
12	-20.231	-4.599			
13	-5.776	-9.666	-2.073		
14	-5.055	-9.063	-4.745	-1.573	
15	-3.919	5.251	-2.614	-1.795	-3.954
16	-2.611	-2.139	-4.028	-2.747	-3.228

	11	12	13	14	15
17	-2.461	-2.489	-3.607	-3.147	-1.794
18	1.967	1.581	-3.266	1.781	-1.911

	16	17	18
16	2.395		
17	10.255	3.310	
18	11.362	10.717	-11.037

Ethane-C13

	1	2	3	4	5
1	-8.309				
2	-3.956	-8.293			
3	9.470	4.598	-8.112		
4	1.761	4.266	-14.160	-5.155	
5	0.251	0.473	-5.746	-4.657	-4.388
6	-28.902	-12.156	-4.800	-3.517	1.227
7	-28.083	-11.799	-4.232	-3.170	1.229
8	-12.601	-29.334	-0.974	-6.387	1.619
9	-12.208	-28.481	-0.614	-5.851	1.622
10	15.910	2.402	-5.316	-1.296	-1.272
11	16.384	2.492	-4.444	-1.010	-1.261
12	0.906	13.830	-2.331	-5.101	-1.348
13	0.983	14.263	-1.966	-4.169	-1.335
14	-2.125	-2.160	-6.991	-4.789	-4.697
15	-2.185	-2.203	-6.112	-3.944	-4.660
16	-2.390	-2.544	-2.811	-3.542	-2.191
17	-2.724	-2.868	-1.384	-2.104	-2.160
18	1.495	2.091	0.369	-2.368	1.633

	6	7	8	9	10
6	-11.565				
7	-12.911	-10.944			
8	-31.262	-8.121	-11.762		
9	-8.133	-29.487	-13.218	-11.095	
10	-8.557	-8.503	-3.235	-3.232	-3.620
11	-7.496	-7.447	-2.825	-2.859	-5.662
12	-4.433	-4.538	-8.589	-8.729	-5.434
13	-4.174	-4.040	-7.760	-7.454	-1.030
14	-2.372	-2.882	-2.101	-1.821	-5.980
15	-3.255	-1.963	-2.096	-1.623	-4.944
16	-3.375	-2.879	-3.544	-3.475	-5.027
17	-3.721	-2.680	-4.505	-2.923	-4.753
18	1.312	1.609	2.032	2.433	-2.646

	11	12	13	14	15
11	-2.773				
12	-1.045	-2.683			
13	-5.060	-4.009	-1.892		
14	-4.399	-5.135	-3.818	-2.249	
15	-5.280	-4.369	-4.339	-0.239	-1.996
16	-3.929	-7.062	-6.270	-7.750	0.755
17	-4.108	-7.010	-6.066	0.345	-5.939
18	2.222	-1.977	2.614	-4.685	-5.220

	16	17	18
16	2.175		
17	9.377	3.088	
18	9.810	9.181	-11.431

A.6.4.2 Transition state

TS-C12

	1	2	3	4	5
1	124.278				
2	-1.706	-93.236			
3	-7.340	0.155	-10.080		
4	-5.118	-0.050	-27.179	-11.645	
5	0.389	-0.201	-11.071	-27.775	-12.081
6	-4.025	0.080	-38.653	-15.716	-3.380
7	1.864	-0.171	-5.786	-17.384	-44.206
8	324.521	-9.892	-13.626	-7.483	0.948
9	2.813	-0.288	-5.883	-13.901	-5.291
10	4.791	-0.198	-3.033	-6.838	-17.636
11	73.231	-3.131	-9.896	-3.516	0.000
12	4.825	-0.094	-2.366	-5.222	-7.306
13	7.983	-0.874	-8.183	-2.314	0.889
14	149.068	-2.843	-1.707	-2.060	-0.866
15	-0.243	-0.560	-3.465	-2.148	-3.297
16	-110.913	-3.189	-5.272	-4.165	-2.175
17	-16.530	-0.512	0.554	0.754	1.081
18	-92.455	-5.782	-3.407	-3.047	-2.849
19	-59.761	-0.950	-3.782	-5.251	-4.028
20	-41.933	-8.370	2.010	1.850	-0.505
21	-74.594	-0.202	-1.529	-0.731	-0.580
22	-22.955	-1.014	-0.884	-2.945	-8.900
23	-80.941	-3.681	-0.693	-1.831	-1.315
24	-278.407	-52.018	-11.883	-15.824	-7.344

	6	7	8	9	10
6	-11.893				
7	-1.363	-11.817			
8	-3.729	3.295	37.388		
9	-0.355	6.912	-1.615	-4.129	
10	-1.010	4.660	1.322	-4.345	-2.585
11	1.764	0.670	-9.576	-1.159	-0.673
12	-0.711	8.806	1.750	-6.380	-6.629
13	-6.683	0.717	112.033	0.096	-0.427
14	4.010	-0.560	260.054	3.056	4.106
15	-3.975	-1.463	-8.856	-5.470	-4.753
16	-2.621	-2.175	91.087	-2.178	-2.757
17	0.102	0.484	-6.609	-1.587	-1.265
18	-3.876	-2.179	-58.101	-4.659	-4.008
19	-2.779	-2.447	-9.164	-5.084	-6.447
20	0.644	-1.374	-22.670	-0.855	-0.054
21	-1.660	-0.068	-22.114	-1.545	-2.484
22	-0.047	-8.984	-24.305	-4.786	-18.693
23	-0.095	-0.428	0.101	-4.085	-2.249
24	-6.453	-0.442	-1.795	-11.885	0.224

	11	12	13	14	15
11	-13.964				
12	-3.061	-8.607			
13	38.581	-0.431	-17.749		
14	70.274	1.238	53.830	-89.403	
15	-12.110	-3.553	0.637	-4.560	-2.014
16	33.809	-2.199	12.271	186.544	-4.854
17	-0.942	-4.013	1.274	0.154	-4.480
18	-14.660	1.052	17.807	34.013	-5.023

	11	12	13	14	15
19	5.292	-2.642	-1.455	58.132	-1.262
20	-23.902	-2.108	-31.574	-25.813	0.193
21	5.177	0.390	-3.000	1.247	-0.302
22	-19.751	-5.121	27.107	7.372	-10.376
23	6.941	3.913	27.729	-35.168	-4.717
24	75.518	13.671	168.186	-79.033	-12.784

	16	17	18	19	20
16	5.493				
17	-9.401	-4.758			
18	-18.581	-5.488	-7.037		
19	-21.116	-6.394	-17.654	-3.914	
20	15.862	12.668	37.506	22.874	-26.470
21	-15.540	-1.327	-3.938	2.047	20.841
22	-0.697	0.660	-12.825	-4.540	-1.823
23	-17.482	-24.101	-36.847	-26.248	35.577
24	-127.233	-92.166	-229.088	-137.949	423.281

	21	22	23	24
21	-11.058			
22	-19.083	-22.352		
23	-9.965	-9.155	-64.375	
24	-36.501	28.917	-1667.231	-3629.405

TS-C13a

	1	2	3	4	5
1	125.116				
2	-1.725	-93.236			
3	-8.053	0.200	-12.466		
4	-4.484	-0.114	-16.570	-14.429	
5	0.005	-0.188	-8.530	-32.591	-10.656
6	-3.925	0.067	-43.524	-10.641	-6.841
7	2.049	-0.181	-2.608	-18.613	-41.405
8	325.524	-9.939	-15.357	-5.800	0.856
9	2.184	-0.260	-3.586	-15.988	-4.835
10	4.702	-0.189	-1.868	-7.875	-16.620
11	73.296	-3.136	-11.347	-2.260	-0.094
12	4.286	-0.099	-1.496	-6.232	-7.126
13	6.721	-0.861	-9.733	-0.915	0.576
14	150.723	-2.913	-1.720	-2.069	-0.643
15	-0.894	-0.582	-3.442	-2.387	-3.429
16	-112.591	-3.165	-5.504	-3.922	-2.352
17	-16.843	-0.547	0.591	0.809	1.100
18	-89.995	-5.668	-3.499	-2.765	-2.839
19	-59.983	-0.957	-3.584	-5.487	-4.124
20	-41.532	-8.362	2.032	1.780	-0.337
22	-22.895	-1.034	-0.364	-3.659	-8.369
23	-82.098	-3.913	-0.796	-2.186	-1.451
24	-277.143	-51.496	-12.011	-16.556	-8.308

	6	7	8	9	10
6	-10.977				
7	-2.972	-12.576			
8	-3.861	3.393	37.573		
9	-0.560	5.942	-1.361	-4.330	
10	-1.664	4.350	1.148	-4.259	-2.497
11	1.545	0.430	-10.507	-0.876	-0.705
12	-0.879	6.028	2.356	-4.672	-6.693
13	-6.365	0.786	111.590	0.379	-0.151
14	3.707	-0.487	272.352	2.542	3.561
15	-4.034	-1.521	-9.035	-5.361	-4.770
16	-2.622	-2.316	82.198	-2.640	-2.951
17	0.168	0.747	-7.013	-1.597	-1.341
18	-3.750	-2.290	-57.255	-4.607	-3.997
19	-2.837	-2.440	-9.236	-5.390	-6.565
20	0.594	-1.489	-22.847	-0.967	0.024
21	-1.597	-0.059	-22.172	-1.342	-2.436
22	-0.449	-9.243	-24.139	-4.148	-18.233
23	-0.282	-0.296	0.524	-2.093	-2.164
24	-7.085	-0.198	0.497	-10.693	0.577

	11	12	13	14	15
11	-14.135				
12	-0.328	-7.967			
13	38.248	-0.426	-18.023		
14	72.785	2.044	56.761	-90.098	
15	-12.110	-3.212	0.767	-4.687	-1.999
16	31.478	-2.151	11.403	191.124	-4.499
17	-0.842	-3.987	1.419	-1.667	-4.526
18	-14.705	1.280	16.896	34.085	-5.231

	11	12	13	14	15
19	5.409	-2.566	-1.498	59.203	-1.320
20	-24.034	-1.554	-31.548	-27.458	0.969
21	4.804	0.578	-2.907	1.455	-0.017
22	-19.932	-5.137	26.333	7.813	-9.591
23	7.729	2.848	29.269	-35.798	-4.950
24	80.724	10.416	170.028	-68.606	-15.300

	16	17	18	19	20
16	1.501				
17	-9.993	-4.848			
18	-18.778	-5.365	-5.968		
19	-21.888	-6.378	-16.265	-3.900	
20	18.777	13.740	35.348	23.096	-26.459
21	-14.607	-1.077	-3.551	1.176	20.586
22	-1.098	0.054	-12.110	-4.576	-1.629
23	-19.782	-25.016	-35.346	-26.830	38.476
24	-139.630	-94.759	-212.106	-137.646	423.280

	21	22	23	24
21	-11.008			
22	-18.896	-22.345		
23	-10.012	-8.401	-70.189	
24	-33.376	33.319	-1726.745	-3585.843

TS-C13b

	1	2	3	4	5
1	126.560				
2	-1.739	-93.236			
3	-6.134	0.044	-8.648		
4	-6.408	0.036	-34.625	-8.903	
5	0.414	-0.204	-19.418	-19.272	-12.362
6	-4.266	0.079	-26.658	-27.544	-2.385
7	1.885	-0.179	-11.518	-11.713	-44.699
8	330.354	-9.826	-10.670	-10.494	0.867
9	2.982	-0.285	-10.005	-9.830	-5.423
10	4.888	-0.199	-5.115	-4.749	-17.877
11	75.294	-3.008	-7.288	-6.079	-0.067
12	4.887	-0.097	-3.864	-3.824	-7.415
13	13.098	-0.967	-5.584	-5.327	1.024
14	148.148	-2.750	-1.737	-1.744	-1.042
15	3.309	-0.550	-3.481	-2.127	-3.333
16	-112.900	-3.315	-4.726	-4.747	-2.280
17	-16.926	-0.471	0.676	0.982	1.131
18	-93.061	-5.784	-3.102	-3.369	-2.828
19	-67.232	-1.080	-4.330	-4.808	-3.915
20	-42.653	-8.396	1.812	1.842	-0.507
21	-75.971	-0.178	-1.505	-0.820	-0.556
22	-22.716	-1.022	-2.245	-1.810	-9.101
23	-81.262	-3.837	-1.489	-1.471	-1.361
24	-277.540	-51.951	-13.467	-14.184	-7.266

	6	7	8	9	10
6	-12.087				
7	-0.896	-11.819			
8	-4.264	2.893	36.207		
9	-0.380	6.732	-1.375	-4.218	
10	-0.857	4.558	1.216	-4.413	-2.610
11	0.502	0.610	-12.510	-0.998	-0.710
12	-0.702	8.734	1.719	-6.460	-6.555
13	-7.223	0.781	124.982	2.576	-0.294
14	3.514	-0.623	231.713	2.487	3.734
15	-3.884	-1.501	-9.579	-5.525	-4.785
16	-2.645	-2.255	95.661	-1.919	-2.586
17	0.342	0.463	-6.465	-1.565	-1.300
18	-3.948	-2.126	-58.231	-4.658	-4.010
19	-2.935	-2.316	-10.803	-5.110	-6.294
20	0.621	-1.354	-22.122	-0.914	-0.273
21	-1.721	-0.063	-20.900	-1.519	-2.451
22	-0.043	-9.024	-23.419	-2.579	-18.942
23	-0.265	-0.314	-1.373	-4.085	-2.129
24	-6.810	-0.308	-6.510	-11.455	0.658
	11	12	13	14	15
11	-14.044				
12	-2.709	-8.572			
13	41.916	0.190	-17.283		
14	66.412	1.008	54.702	-92.569	
15	-14.119	-3.661	1.708	-1.486	-2.198
16	35.646	-2.191	19.076	172.375	-3.606
17	-0.740	-4.142	0.122	1.832	-4.050
18	-13.681	0.989	18.684	33.371	-4.641

	11	12	13	14	15
19	6.856	-2.424	-1.643	61.887	0.265
20	-59.379	-2.055	-30.828	-17.988	-3.325
21	6.754	0.385	-4.335	0.666	0.985
22	-12.732	-5.190	26.048	0.719	-11.793
23	8.680	3.748	27.438	-41.353	-1.284
24	89.162	14.003	154.169	-109.639	8.606
	16	17	18	19	20
16	14.132				
17	-8.003	-4.484			
18	-14.456	-6.130	-6.969		
19	-15.630	-6.812	-19.190	-5.343	
20	11.538	10.687	35.639	24.442	-25.004
21	-13.379	-0.959	-4.070	0.132	20.654
22	0.243	-0.457	-12.749	-4.288	-1.377
23	-15.565	-18.638	-36.673	-28.449	35.723
24	-109.291	-77.576	-220.344	-150.553	414.316
	21	22	23	24	
21	-11.316				
22	-18.764	-22.545			
23	-9.775	-8.233	-66.925		
24	-35.369	34.124	-1693.520	-3606.411	

Schriften des Forschungszentrums Jülich
Reihe Energie & Umwelt / Energy & Environment

Weitere *Schriften des Verlags im Forschungszentrum Jülich* unter
http://wwwzb1.fz-juelich.de/verlagextern1/index.asp

JÜLICH
FORSCHUNGSZENTRUM